CO-ASSEMBLY OF NANOSTRUCTURED HYBRID MATERIALS FOR ENERGY APPLICATIONS

A Dissertation

Presented to the Faculty of the Graduate School

of Cornell University

In Partial Fulfillment of the Requirements for the Degree of

Doctor of Philosophy

by

Kwan Wee Tan

August 2014

CO-ASSEMBLY OF NANOSTRUCTURED HYBRID MATERIALS FOR ENERGY APPLICATIONS

Kwan Wee Tan, Ph.D.

Cornell University 2014

Self-assembly is employed in nature to build multi-dimensional hierarchical materials and represents a viable synthetic approach to construct next-generation functional materials for a large number of applications. This dissertation describes the design, synthesis and characterization of multifunctional nanostructured hybrid materials on multiple length scales by co-assembly of organic and organic/inorganic components. These materials are promising for a number of applications, and in particular for energy conversion devices.

In the first part, organic-inorganic co-assembly is coupled with conventional heating (10^2-10^5 s) to generate hybrid materials for solid-state hybrid solar cells. A polyisoprene-*block*-polystyrene-*block*-polyethylene oxide (PI-*b*-PS-*b*-PEO) triblock terpolymer was employed to structure-direct alumina sol to form mesoporous block copolymer (BCP) directed alumina superstructures. *In situ* grazing incidence wide-angle X-ray scattering and scanning electron microscopy were utilized to probe the structural evolution of methylammonium lead trihalide perovskite on mesoporous BCP-directed alumina superstructures during thermal annealing. A crystalline precursor structure not previously described was discovered to be highly crucial in enhancing perovskite film morphology and coverage, leading to better performing hybrid perovskite solar cells. Time/temperature control in thermal annealing enabled tuning the

macroscopic perovskite film morphology and the crystal texture simultaneously.

Extending the concept of time/temperature control in structure formation, the second part of the dissertation focuses on directed self-assembly using transient heating (10^{-8}-10^{-3} s) to generate porous crystalline semiconductor and organic nanostructures. In a first example, a 308 nm pulsed XeCl excimer laser was used to induce transient melting of amorphous silicon in colloidal self-assembly-directed silica templates, which subsequently solidified into crystalline silicon nanostructures with hexagonal non-close-packed symmetry. Subsequently, by harnessing the thermal stability enhancement of organic polymers under transient heating, direct laser writing of porous organic structures is discussed by combining block copolymer-resol co-assembly with a 10.6 μm continuous wave CO_2 laser-induced transient heating. Organic-organic hybrid thin films of PI-*b*-PS-*b*-PEO mixed with resorcinol-formaldehyde resol oligomers were heated by the CO_2 laser on sub-millisecond time scales, inducing PI-*b*-PS-*b*-PEO decomposition and resol thermopolymerization, to form hierarchical porous resin polymer structures with 3D connectivity, high surface areas and exceptional chemical, mechanical and thermal properties. The porous resin structures are highly suitable for a number of potential applications, *e.g.*, microfluidic reactors, BCP organic templating to generate crystalline silicon network nanostructures, and energy conversion and storage.

BIOGRAPHICAL SKETCH

Kwan Wee Tan is from the island state of Singapore. During his pre-tertiary education days, he met many inspiring teachers who motivated him to make efforts to pay attention in their classes. Outside the classroom, he was very active in the National Cadet Corps, a uniformed student organization supported by the Ministries of Defence and Education. However, his heavy involvement caused severe distress to his parents and teachers for negligence in his school work. He was ranked last in class for his mid-semester examinations and became a highly agitated topic of discussion between his parents and teachers. After completing his A-Levels at Nanyang Junior College in 1999, Kwan Wee served his country as a specialist instructor with the Singapore Combat Engineers for two years and four months. He harbored the intention to pursue a military career during National Service before finally decided to take a gamble with other career opportunities as a civilian.

Kwan Wee matriculated at Nanyang Technological University to pursue his Bachelor degree in Materials Engineering in 2002. He gained his first experience living abroad as a student intern at Nokia GmbH in Bochum, Germany in July 2004. Even today, he missed the great fun and company with his international friends and, of course, the free flow of coffee. He gained his first research experience working under the supervision of Prof. Chee C. Wong for his final year project on colloidal self-assembly. Seemingly making up to his academic curriculum, Kwan Wee was named Valedictorian and earned his Bachelor of Engineering degree with First Class Honours in June 2006. Inspired by Prof. Wong's life and research philosophies, Kwan Wee continued to work in his group, first as a research associate and then a M.Eng./M.S. candidate, where he conducted research in science and play with many great friends seated in the graduate

student office. He was awarded the Singapore-MIT Alliance graduate fellowship to earn his dual Master degrees from Massachusetts Institute of Technology in September 2008 and National University of Singapore in April 2009.

In August 2009, Kwan Wee enrolled in Cornell University and joined Prof. Ulrich Wiesner's research group. His doctoral research was on organic, inorganic and hybrid nanostructure formation by coupling soft matter self-assembly with transient laser annealing, co-advised by Prof. Michael O. Thompson. In October 2011, he visited Prof. Henry Snaith's group at University of Oxford and constructed his first solid-state dye-sensitized solar cell devices. He obtained his Master of Science and Doctor of Philosophy degrees in Materials Science and Engineering in January 2013 and August 2014, respectively. His graduate study at Cornell University was supported by the Singapore National Research Foundation Ph.D. Scholarship.

Dedicated to my family, mentors and friends

for their unwavering encouragement, inspiration and support.

ACKNOWLEDGMENTS

I like to express my appreciation to many people that I have the honor to meet, learn and have fun with during my five year journey at Cornell. First and foremost, I am sincerely grateful to Prof. Uli Wiesner and Prof. Mike Thompson who have instilled invigorating creativity and enthusiasm in my research. Under their dedicated teachings, I have grown into a confident independent researcher who seeks excellence and pride in my work. Special thanks to my committee members Prof. Frank DiSalvo and Prof. Lara Estroff for their alternative insights and guidance in my doctoral research. I also thank Prof. Tobias Hanrath and Prof. Henry Snaith for their kind invitations to work in their laboratories.

This dissertation would not have been possible without the generous support from many excellent friends in the Wiesner and Thompson research groups and collaborators. I like to especially acknowledge Hitesh Arora, Robert Bell, Michelle Chavis, Christina Cowman-Eggert, Rachel Dorin, Yibei Gu, Tobias Hoheisel, Kahyun Hur, Alan Jacobs, Byungki Jung, Cathy Zihui Li, David Lynch, David Moore, Spencer Robbins, Hiroaki Sai, Michael Saliba, Juho Song, Aey Suteewong, Yao Sun, Joerg Werner, Takeshi Yuasa and Qi Zhang for their friendships and nonsenses. I have been fortunate for the chance to guide my former undergraduate student Stacey Saba and a big thank you for supporting my work. Congratulations on passing her qualifying examinations and best wishes to her doctoral research in the Hillmyer group at University of Minnesota. I also thank my friends back in Singapore for still remembering my existence and organizing our get-together events during my home trips.

Research at Cornell has been a great experience with our open collaborative culture and world-class facilities on campus. I like to thank all the facility managers and

staff members who have assisted me greatly: Prof. Kit Umbach, Dolores Dewbury, Phil Carubia, Beth Rhoades, Mick Thomas and Maura Weathers. I also like to thank the administrative staff in the Department of Materials Science and Engineering for ensuring the smooth operation of the offices and laboratories.

I am thankful to the Singapore Energy Innovation Programme Office for financial support with a graduate fellowship and administrative support from Li Shan Tham, Cecilia Wong, Shirley Ong and Mee Kim Wong.

My deepest heartfelt gratitude to my parents for their sacrifices and my siblings for their patience to give me the opportunity to pursue my dreams.

TABLE OF CONTENTS

LIST OF FIGURES

LIST OF TABLES

CHAPTER 1

INTRODUCTION

Nature is a great source of inspiration for many intriguing examples of hierarchical functional materials, ranging from protein molecules, microscopic *Aulacoseira* (diatom) and *Euplectella* sp. biosilicas, to larger bones and wood hybrid fibrous composites[1–5], see Figure 1.1. Their multi-functional properties is a collective consequence of both the structure and individual components. In retrospect, these natural structural materials have evolved continuously over many millenniums to develop their multi-dimensional complexities and functionalities; however, current synthetic approaches developed to construct structures with multi-length scale features and morphologies integrating novel functional properties are still limited. Hence, new design and synthesis strategies are required to realize hierarchical functional materials for emerging technologies[6].

Hierarchical structures, in particular three-dimensional (3D) nanomaterials, are often challenging to fabricate using top-down techniques. For example, conventional photolithography is quickly approaching the theoretical resolution limits and requires multiple processing steps to fabricate 3D features[7,8]. Bottom-up self-assembly of building blocks[2,9–25] provides a direct pathway to construct a plethora of tailored superstructures and morphologies with different length scales for many applications, including catalysis[26,27], electronics[28], energy storage[29,30], hybrid solar cells[30–32], membrane separation[20], and photonics and metamaterials[33–38].

Block copolymers (BCP) provide a unique platform to fabricate ordered mesoscale morphologies (2-50 nm) with 2D and 3D periodicity in the bulk[16–19,30]. A

linear BCP is a macromolecule consisting of a sequence of two or more chemically distinct polymeric chains (blocks) linked by covalent bonds. In the melt phase, the immiscible blocks repel one another and microphase segregate to form a variety of ordered structures. However, most all-organic ordered BCP morphologies have poor mechanical and thermal stability and functional properties.

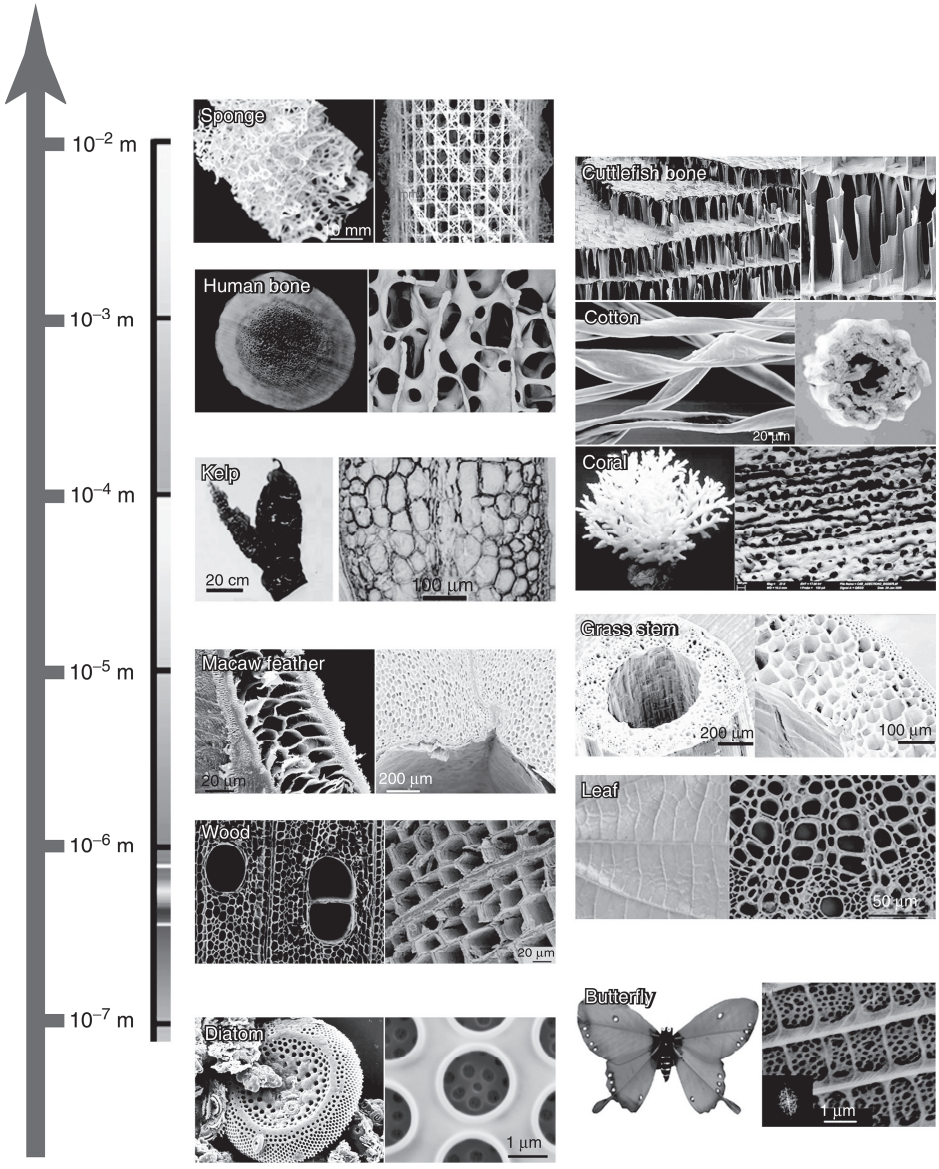

Figure 1.1. A general overview of natural hierarchical structures ranked in descending order of their critical dimensions. Reproduced with permission[5]. Copyright 2011, Wiley-VCH.

Organic-inorganic/organic hybrid materials represent a novel class of materials enabling improved physical and functional properties. BCPs are utilized to direct the structure of organic/inorganic additives into a myriad of mesoscopic morphologies with new and enhanced properties[21–25,39–44]. Wiesner and co-workers first employed polyisoprene-*block*-polyethylene oxide (PI-*b*-PEO) as a structure-directing agent (SDA) for organically modified aluminosilicate sol nanoparticles to form a myriad of BCP-directed aluminosilicate hybrid materials[23,45–47]. The mesostructured materials remained stable up to 600 °C when PI-*b*-PEO SDA was removed during calcination leaving behind the mesoporous inorganic phase[45,46].

New properties and functionalities are incorporated into BCP-directed hybrid and mesoporous structured materials by tuning the macromolecular chemistry, morphology and additive materials selection. Electrically conductive mesoporous polycrystalline structures with lamellar and hexagonal morphologies were formed employing PI-*b*-PEO and polyisoprene-*block*-polydimethylaminoethyl methacrylate (PI-*b*-PDMAEMA) diblock copolymers to structure-direct transitional metal oxide sols and ligand-stabilized platinum nanoparticles, respectively, after heat treatment[39,40]. The addition of a third block to the BCP increases the degree of freedom and expands the composition window of 3D periodic continuous network morphologies that are expected to provide high mechanical stability and connectivity[18]. To this end, polyisoprene-*block*-polystyrene-*block*-polyethylene oxide (PI-*b*-PS-*b*-PEO) and polyisoprene-*block*-polystyrene-*block*-poly(*N,N*-dimethylamino)ethyl methacrylate (PI-*b*-PS-*b*-PDMAEMA) have been utilized as SDAs for inorganic and organic additives to form highly ordered 3D mesoporous aluminosilicate, niobia, titania, carbon and binary gold-platinum structures with continuous gyroid morphology[48–50,44]. Remarkably, gyroidal mesoporous carbons exhibited long range order even after pyrolysis at 1600 °C

attributed to enhanced mechanical integrity inherited from the 3D network structure[44]. Mesoporous gyroidal anatase titania was deployed in dye-sensitized solar cells as a highly porous electron-collecting electrode providing continuous connectivity for charge transport and continuous pore network for backfilling with the hole transport material[31,32]

In Chapter 2, the first application of a mesoporous PI-*b*-PS-*b*-PEO terpolymer-directed alumina as superstructure support for hybrid perovskite solar cells is reported. Synchrotron radiation based grazing incidence wide- and small-angle X-ray scattering (GIWAXS/GISAXS) and scanning electron microscopy (SEM) were employed to generate the structure-property correlations for methylammonium lead trihalide perovskite on BCP-directed alumina superstructure. Real-time GIWAXS measurements of hybrid perovskite thermally annealed on a hotplate provide insight into control of crystal growth and film morphology leading to improved mesoporous BCP-directed alumina perovskite solar cell performance. Changes in hybrid perovskite structure formation on BCP-directed alumina superstructure and other solar cell device architectures induced by a rapid increase of annealing temperature are discussed in Chapter 3.

To access more complex functional nanostructures, BCP-directed mesoporous aluminosilicate and niobia template formation was coupled with transient laser annealing to generate single-crystal epitaxial silicon (Si) and nickel silicide (NiSi) nanostructures[51]. A 40 ns full-width-half-maximum pulsed XeCl excimer laser irradiation melted both the amorphous Si and NiSi as well as part of the Si substrate. The molten Si and NiSi backfilled the mesoporous BCP-directed inorganic templates, which subsequently solidified with the single-crystal orientation directed epitaxially by the Si substrate in less than 100 ns, see Figure 1.2. It should be noted that high pattern

transfer fidelity was enabled by thermal stability enhancement of BCP-directed amorphous aluminosilicate and niobia template retaining structure integrity up to 1414 °C (Si m.p.) under transient heating. Thompson and co-workers have also reported similar enhancement effects for organic systems heated by CO_2 laser spike annealing on sub-millisecond time frames remaining stable up to 800 °C[52].

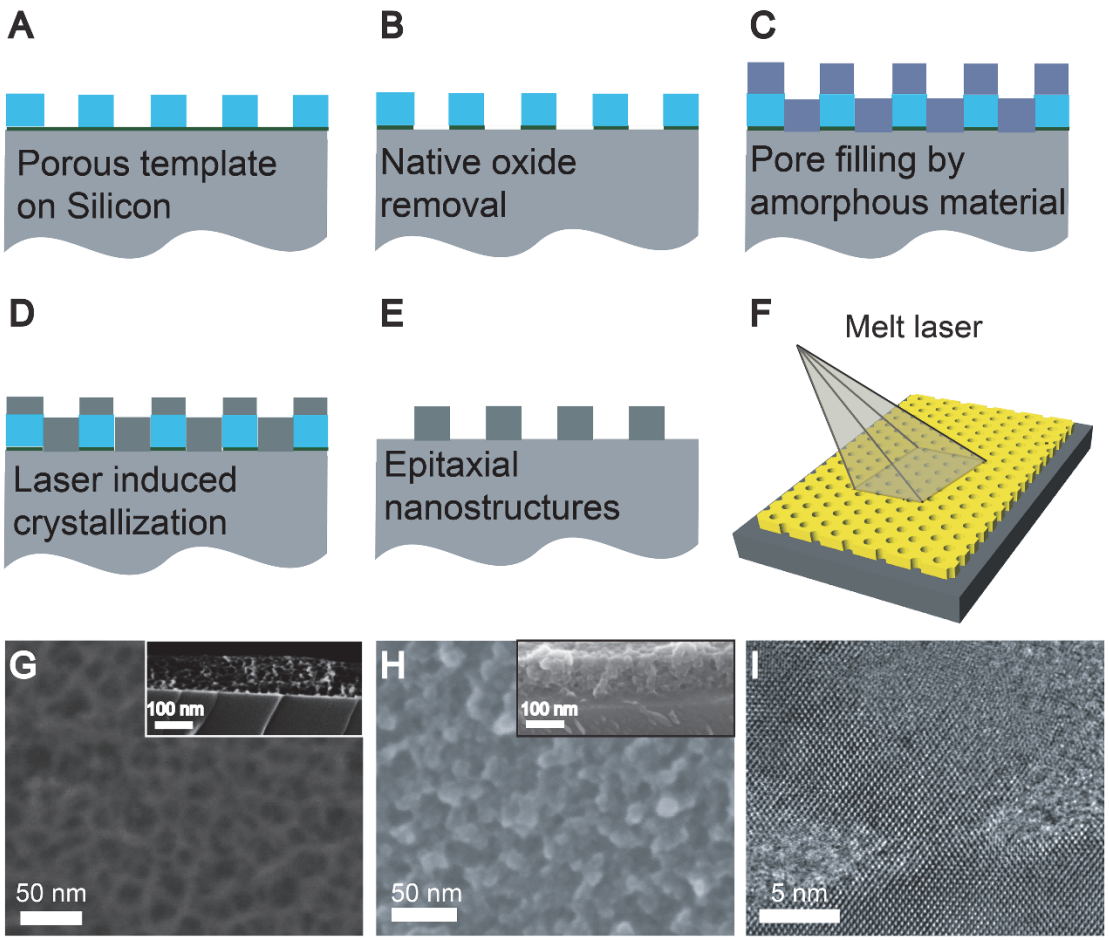

Figure 1.2. (a-e) Schematic illustration of single-crystal epitaxial nanostructure fabrication and (f) laser irradiation of template covered silicon substrate. Plan view and cross-sectional (insets) scanning electron microscopy images of (g) PI-*b*-PS-*b*-PEO directed niobia template and (h) inverse single-crystal epitaxial Si nanostructure after niobia template removal. (i) Cross-sectional high resolution transmission electron microscopy image shows the congruence of lattice fringes in the single-crystal silicon nanostructure in (g) and Si substrate. From ref. 51. Reprinted with permission from AAAS.

Chapter 4 describes the pulsed laser induced melt-solidification of amorphous Si into larger 2D/3D crystalline Si nanostructures with non-close-packed symmetry using alternative colloidal self-assembly-directed silica templates. In Chapter 5, CO_2 laser spike annealing was applied on block copolymer-directed resol hybrid systems for direct laser writing of mesoporous 3D resin polymer network structures. Under transient heating on sub-millisecond time frames, temperature stability of resin polymer was enhanced beyond conventional limits retaining the mesostructure while BCP was thermally decomposed to generate porosity in air. The porous structure formation is rapid (<5 min) and grating patterns are defined directly by the CO_2 laser beam. Pyrolysis heat treatment condensed the phenolic resin into an electrically conductive mesoporous amorphous carbon phase. The enhanced thermal stability obtained via transient heating enabled the resin structure to be employed as a template to form mesoporous crystalline Si nanostructures in Chapter 6. Finally, a summary of the dissertation and suggestions for future work are provided in Chapter 7.

REFERENCES

1. Fratzl, P. in *Learning from Nature How to Design New Implantable Biomaterialsis: From Biomineralization Fundamentals to Biomimetic Materials and Processing Routes* (eds. Reis, R. L. & Weiner, S.) 15–34 (Springer Netherlands, 2005).

2. Boncheva, M. & Whitesides, G. M. Making Things by Self-Assembly. *MRS Bull.* **30,** 736–742 (2005).

3. Aizenberg, J. *et al*. Skeleton of Euplectella sp.: Structural Hierarchy from the Nanoscale to the Macroscale. *Science* **309,** 275–278 (2005).

4. Bao, Z. *et al*. Chemical reduction of three-dimensional silica micro-assemblies into microporous silicon replicas. *Nature* **446,** 172–175 (2007).

5. Su, B.-L., Sanchez, C. & Yang, X.-Y. in *Hierarchically Structured Porous Materials* (eds. Su, B.-L., Sanchez, C. & Yang, X.-Y.) 1–27 (Wiley-VCH Verlag GmbH & Co. KGaA, 2011).

6. Hemminger, J., Crabtree, G. & Sarrao, J. *From Quanta to the Continuum: Opportunities for Mesoscale Science*. (U.S. Department of Energy Basic Energy Sciences Advisory Committee Report, 2012). at <http://science.energy.gov/~/media/bes/pdf/reports/files/OFMS_rpt.pdf>

7. Ito, T. & Okazaki, S. Pushing the limits of lithography. *Nature* **406,** 1027–1031 (2000).

8. Nie, Z. & Kumacheva, E. Patterning surfaces with functional polymers. *Nat. Mater.* **7,** 277–290 (2008).

9. Whitesides, G. M. & Grzybowski, B. Self-Assembly at All Scales. *Science* **295,** 2418–2421 (2002).

10. Mann, S. Self-assembly and transformation of hybrid nano-objects and nanostructures under equilibrium and non-equilibrium conditions. *Nat. Mater.* **8,** 781–792 (2009).

11. Xia, Y., Gates, B., Yin, Y. & Lu, Y. Monodispersed Colloidal Spheres: Old Materials with New Applications. *Adv. Mater.* **12,** 693–713 (2000).

12. Leunissen, M. E. et al. Ionic colloidal crystals of oppositely charged particles. *Nature* **437,** 235–240 (2005).

13. Kalsin, A. M. *et al*. Electrostatic Self-Assembly of Binary Nanoparticle Crystals with a Diamond-Like Lattice. *Science* **312,** 420–424 (2006).

14. Shevchenko, E. V., Talapin, D. V., Kotov, N. A., O'Brien, S. & Murray, C. B. Structural diversity in binary nanoparticle superlattices. *Nature* **439,** 55–59 (2006).

15. Talapin, D. V. *et al*. Quasicrystalline order in self-assembled binary nanoparticle superlattices. *Nature* **461,** 964–967 (2009).

16. Bates, F. S. Polymer-Polymer Phase Behavior. *Science* **251,** 898–905 (1991).

17. Bates, F. S. & Fredrickson, G. H. Block Copolymers—Designer Soft Materials. *Phys. Today* **52,** 32–38 (1999).

18. Bates, F. S. Network Phases in Block Copolymer Melts. *MRS. Bull.* **30,** 525–532 (2005).

19. Ross, C. A., Berggren, K. K., Cheng, J. Y., Jung, Y. S. & Chang, J.-B. Three-

Dimensional Nanofabrication by Block Copolymer Self-Assembly. *Adv. Mater.* **26,** 4386–4396 (2014).

20. Peinemann, K.-V., Abetz, V. & Simon, P. F. W. Asymmetric superstructure formed in a block copolymer via phase separation. *Nat. Mater.* **6,** 992–996 (2007).

21. Yanagisawa, T., Shimizu, T., Kuroda, K. & Kato, C. The Preparation of Alkyltriinethylaininonium–Kaneinite Complexes and Their Conversion to Microporous Materials. *Bull. Chem. Soc. Jpn.* **63,** 988–992 (1990).

22. Kresge, C. T., Leonowicz, M. E., Roth, W. J., Vartuli, J. C. & Beck, J. S. Ordered mesoporous molecular sieves synthesized by a liquid-crystal template mechanism. *Nature* **359,** 710–712 (1992).

23. Templin, M. *et al*. Organically Modified Aluminosilicate Mesostructures from Block Copolymer Phases. *Science* **278,** 1795–1798 (1997).

24. Yang, P., Zhao, D., Margolese, D. I., Chmelka, B. F. & Stucky, G. D. Generalized syntheses of large-pore mesoporous metal oxides with semicrystalline frameworks. *Nature* **396,** 152–155 (1998).

25. Zhao, D. *et al*. Triblock Copolymer Syntheses of Mesoporous Silica with Periodic 50 to 300 Angstrom Pores. *Science* **279,** 548–552 (1998).

26. Chai, G. S., Shin, I. S. & Yu, J.-S. Synthesis of Ordered, Uniform, Macroporous Carbons with Mesoporous Walls Templated by Aggregates of Polystyrene Spheres and Silica Particles for Use as Catalyst Supports in Direct Methanol Fuel Cells. *Adv. Mater.* **16,** 2057–2061 (2004).

27. Kamperman, M. *et al*. Integrating Structure Control over Multiple Length Scales in Porous High Temperature Ceramics with Functional Platinum Nanoparticles. *Nano Lett.* **9,** 2756–2762 (2009).

28. Urban, J. J., Talapin, D. V., Shevchenko, E. V., Kagan, C. R. & Murray, C. B. Synergism in binary nanocrystal superlattices leads to enhanced p-type conductivity in self-assembled PbTe/Ag_2Te thin films. *Nat. Mater.* **6,** 115–121 (2007).

29. Ji, X., Lee, K. T. & Nazar, L. F. A highly ordered nanostructured carbon–sulphur cathode for lithium–sulphur batteries. *Nat. Mater.* **8,** 500–506 (2009).

30. Orilall, M. C. & Wiesner, U. Block copolymer based composition and morphology control in nanostructured hybrid materials for energy conversion and storage: solar cells, batteries, and fuel cells. *Chem. Soc. Rev.* **40,** 520–535 (2011).

31. Crossland, E. J. W. *et al*. A Bicontinuous Double Gyroid Hybrid Solar Cell. *Nano Lett.* **9,** 2807–2812 (2009).

32. Docampo, P. *et al*. Triblock-Terpolymer-Directed Self-Assembly of Mesoporous TiO_2: High-Performance Photoanodes for Solid-State Dye-Sensitized Solar Cells. *Adv. Energy Mater.* **2,** 676–682 (2012).

33. Blanco, A. *et al*. Large-scale synthesis of a silicon photonic crystal with a complete three-dimensional bandgap near 1.5 micrometres. *Nature* **405,** 437–440 (2000).

34. Vlasov, Y. A., Bo, X.-Z., Sturm, J. C. & Norris, D. J. On-chip natural assembly of silicon photonic bandgap crystals. *Nature* **414,** 289–293 (2001).

35. Fink, Y., Urbas, A. M., Bawendi, M. G., Joannopoulos, J. D. & Thomas, E. L. Block Copolymers as Photonic Bandgap Materials. *J. Lightwave Technol.* **17,** 1963 (1999).

36. Urbas, A. m., Maldovan, M., DeRege, P. & Thomas, E. l. Bicontinuous Cubic Block

Copolymer Photonic Crystals. *Adv. Mater.* **14,** 1850–1853 (2002).

37. Hur, K. *et al*. Three-Dimensionally Isotropic Negative Refractive Index Materials from Block Copolymer Self-Assembled Chiral Gyroid Networks. *Angew. Chem. Int. Ed.* **50,** 11985–11989 (2011).

38. Vignolini, S. *et al*. A 3D Optical Metamaterial Made by Self-Assembly. *Adv. Mater.* **24,** OP23–OP27 (2012).

39. Lee, J. *et al*. Direct access to thermally stable and highly crystalline mesoporous transition-metal oxides with uniform pores. *Nat. Mater.* **7,** 222–228 (2008).

40. Warren, S. C. *et al*. Ordered Mesoporous Materials from Metal Nanoparticle–Block Copolymer Self-Assembly. *Science* **320,** 1748–1752 (2008).

41. Liang, C., Hong, K., Guiochon, G. A., Mays, J. W. & Dai, S. Synthesis of a Large-Scale Highly Ordered Porous Carbon Film by Self-Assembly of Block Copolymers. *Angew. Chem. Int. Ed.* **43,** 5785–5789 (2004).

42. Meng, Y. *et al*. Ordered Mesoporous Polymers and Homologous Carbon Frameworks: Amphiphilic Surfactant Templating and Direct Transformation. *Angew. Chem. Int. Ed.* **44,** 7053–7059 (2005).

43. Werner, J. G., Hoheisel, T. N. & Wiesner, U. Synthesis and Characterization of Gyroidal Mesoporous Carbons and Carbon Monoliths with Tunable Ultralarge Pore Size. *ACS Nano* **8,** 731–743 (2014).

44. Sai, H. *et al*. Hierarchical Porous Polymer Scaffolds from Block Copolymers. *Science* **341,** 530–534 (2013).

45. Simon, P. F. W., Ulrich, R., Spiess, H. W. & Wiesner, U. Block Copolymer−Ceramic Hybrid Materials from Organically Modified Ceramic Precursors. *Chem. Mater.* **13,** 3464–3486 (2001).

46. Du, P. *et al*. Additive-Driven Phase-Selective Chemistry in Block Copolymer Thin Films: The Convergence of Top–Down and Bottom–Up Approaches. *Adv. Mater.* **16,** 953–957 (2004).

47. Garcia, B. C. *et al*. Morphology Diagram of a Diblock Copolymer−Aluminosilicate Nanoparticle System. *Chem. Mater.* **21,** 5397–5405 (2009).

48. Stefik, M. *et al*. Ordered Three- and Five-ply Nanocomposites from ABC Block Terpolymer Microphase Separation with Niobia and Aluminosilicate Sols. *Chem. Mater.* **21,** 5466–5473 (2009).

49. Stefik, M. *et al*. Networked and chiral nanocomposites from ABC triblock terpolymer coassembly with transition metal oxide nanoparticles. *J. Mater. Chem.* **22,** 1078–1087 (2011).

50. Li, Z. *et al*. Linking experiment and theory for three-dimensional networked binary metal nanoparticle–triblock terpolymer superstructures. *Nat. Commun.* **5,** (2014).

51. Arora, H. *et al*. Block Copolymer Self-Assembly–Directed Single-Crystal Homo- and Heteroepitaxial Nanostructures. *Science* **330,** 214–219 (2010).

52. Jung, B. *et al*. Kinetic Rates of Thermal Transformations and Diffusion in Polymer Systems Measured during Sub-millisecond Laser-Induced Heating. *ACS Nano* **6,** 5830–5836 (2012).

CHAPTER 2

THERMALLY INDUCED STRUCTURAL EVOLUTION AND PERFORMANCE OF MESOPOROUS BLOCK COPOLYMER-DIRECTED ALUMINA PEROVSKITE SOLAR CELLS

Abstract

Structure control in solution-processed hybrid perovskites is crucial to design and fabricate highly efficient solar cells. Here, we utilize *in situ* grazing incidence wide-angle X-ray scattering and scanning electron microscopy to investigate the structural evolution and film morphologies of methylammonium lead tri-iodide/chloride ($CH_3NH_3PbI_{3-x}Cl_x$) in mesoporous block copolymer derived alumina superstructures during thermal annealing. We show the $CH_3NH_3PbI_{3-x}Cl_x$ material evolution to be characterized by three distinct structures: a crystalline precursor structure not described previously, a 3D perovskite structure, and a mixture of compounds resulting from degradation. Finally, we demonstrate how understanding the processing parameters provides the foundation needed for optimal perovskite film morphology and coverage, leading to enhanced block copolymer-directed perovskite solar cell performance.

Reproduced with permission from Tan, K. W.[*], Moore, D. M.[*], Saliba, M.[*], Sai, H., Estroff, L. A., Hanrath, T., Snaith, H. J. & Wiesner, U. Thermally induced structural evolution and performance of mesoporous block copolymer-directed alumina perovskite solar cells. *ACS Nano* **8**, 4730–4739 (2014).

([*]These authors contributed equally to this work.)

Introduction

Harnessing sunlight to generate photovoltaic electricity based on thin film solar cell technologies is desirable to deliver green, sustainable energy at reduced materials and fabrication cost.[1,2] Thin film hybrid solar cells using solution-processable materials[2] such as semiconductor nanocrystals,[3,4] organic polymers,[5,6] or dye-sensitized solar cells[7–9] have achieved 7-12% power conversion efficiencies (PCEs). Recently, a new class of highly efficient solid-state hybrid perovskite solar cells has been reported pushing PCEs above 15%.[10–34]

Organic-inorganic hybrid materials enable the combination of both organic and inorganic qualities into a single molecular composite. These hybrid materials have been studied extensively for their electrical, mechanical, and optical functional properties and have been applied, for example, in field-effect transistors, optoelectronic devices and hybrid solar cells.[35–38] Another area of intense scientific research and commercial interest is utilizing the methylammonium lead trihalide ($CH_3NH_3PbX_3$; X = I, Br, Cl) semiconducting perovskite in thin film photovoltaics.[10–34] The $CH_3NH_3PbX_3$ perovskite semiconductor material is highly attractive due to the ease of solution processing and excellent absorption properties in the near-infrared spectrum to generate charge carriers.[10,12,13,18] Moreover, ambipolar charge transport properties and long carrier lifetimes enable the direct transport of both photogenerated electron and hole charge carriers to the respective collecting electrodes.[14,15,18,19,28,29,34]

The photovoltaic device architecture provides an alternative approach to enhance device performance.[39–41] In particular, block copolymer (BCP) self-assembly-directed materials have improved charge transport and light management of mesoscopic solar cells *via* control of morphology,[37,38,41–46] porosity and pore size,[46–50] material crystallinity,[51,52] electronic[37,52] and optical[47,53] properties. For example, well-ordered

bicontinuous BCP gyroid morphologies enable easy backfilling of the hole transport materials and complete mesopore interconnectivity in solid-state dye-sensitized solar cells.[37,38] Moreover, porous BCP nanostructures provide control over single-crystal epitaxial nanostructures,[51] and may enable tuning the feature size and morphology of well-defined $CH_3NH_3PbX_3$ nanocrystallites within the BCP mesoporous heterojunction electrode to achieve excellent photovoltaic device performance.[19,24,32–34] Combining BCP structure control with the organic-inorganic hybrid perovskite, observation of structural evolution at multiple length scales is expected to be key to establishing structure-property correlations. To the best of our knowledge, such evolution of thermally annealed hybrid perovskites obtained *via* a single-step spin coating process has not been reported.

In this work we employed *in situ* time-resolved grazing incidence wide-angle x-ray scattering (GIWAXS) to probe the structure of methylammonium lead tri-iodide/chloride ($CH_3NH_3PbI_{3-x}Cl_x$) perovskites in mesoporous block copolymer-directed alumina (MBCP-Al_2O_3) during thermal annealing. Optimized structure and film morphology of the organic-inorganic hybrid perovskites resulted in enhanced meso-superstructured solar cell performance.

Results and Discussion

GIWAXS of $CH_3NH_3PbI_{3-x}Cl_x$ Perovskites. One of the key advantages of the $CH_3NH_3PbX_3$ hybrid perovskite photovoltaic devices is the ease of solution-processing. The organic (CH_3NH_3I) and inorganic precursors ($PbCl_2$) are dissolved in a common solvent (*N,N*-dimethylformamide), deposited on a substrate by spin coating, and annealed at relatively low temperatures of 90-100 °C for 5-120 min to induce perovskite

crystallization.[12–23,25–27] However, crystallographic data obtained from one-dimensional (1D) powder X-ray diffraction provides only limited structural information, in particular for the highly oriented perovskite thin films.[12,13,18,19,22–26] To this end, we employed GIWAXS with 2D detection capability to probe the crystallographic orientations of planar $CH_3NH_3PbI_{3-x}Cl_x$ perovskite thin films.

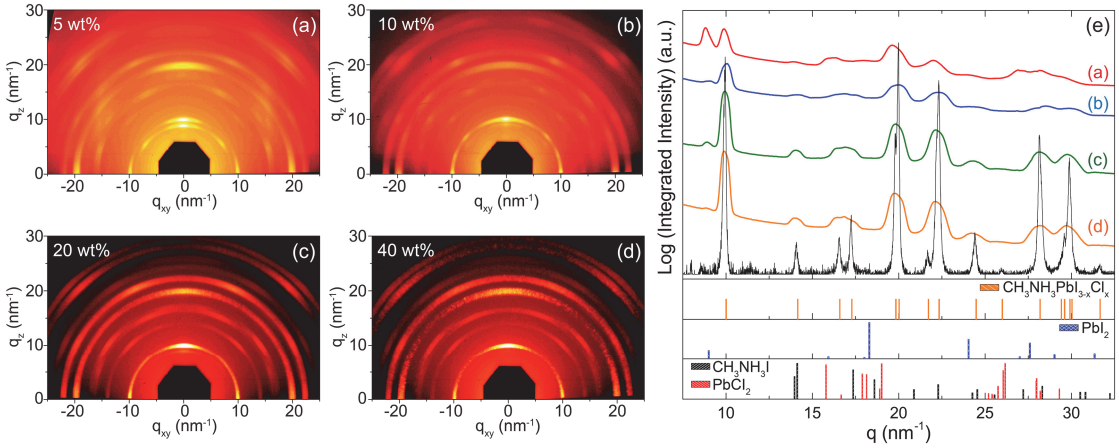

Figure 2.1. 2D GIWAXS profiles of $CH_3NH_3PbI_{3-x}Cl_x$ perovskite films on flat substrates prepared from (a) 5 wt%, (b) 10 wt%, (c) 20 wt%, (d) 40 wt% precursor solutions, and annealed at 100 °C for 45 min. (e) Azimuthally integrated intensity plots of the GIWAXS patterns. The bottom black curve is the XRD spectrum of the $CH_3NH_3PbI_{3-x}Cl_x$ perovskite measured in powdered form.

Characterization of Mesoporous Block Copolymer-Directed Alumina Thin Films. In a solvent mixture of non-polar toluene and polar *n*-butanol, the structure directing polyisoprene-*block*-polystyrene-*block*-polyethylene oxide (PI-*b*-PS-*b*-PEO) triblock terpolymer forms micelles with the hydrophobic PI and PS in the core, and a hydrophilic PEO corona.[46–49] The added Al_2O_3 sol is selectively attracted to the PEO corona by hydrogen bonds.[42] Upon solvent evaporation, the organic-inorganic micelles

self-assemble into a randomly packed arrangement. Mesoporous block copolymer-directed alumina (MBCP-Al_2O_3) thin films with interconnected porosity are generated when the organic components are removed by calcination as evidenced by the scanning electron microscopy (SEM) and atomic force microscopy (AFM) images in Figures 2.2 and S2.1, respectively. The MBCP-Al_2O_3 pores are interconnected in both in-plane and out-of-plane directions. From SEM and AFM, the pore diameter is ~36 nm and the film thickness is 70-80 nm after calcination. In 2D grazing incidence small-angle X-ray scattering (GISAXS) patterns, we observe two intense diffraction peaks at q_{xy} = ±0.157 nm^{-1} (Figure 2.2c) consistent with a disordered mesoporous material with a macroscopically homogenous in-plane d-spacing of $2\pi/q_{xy} \approx 40$ nm.[49] The oscillations at the diffraction peaks are attributed to the form factor of the film thickness.[57] In contrast, the porosity of Al_2O_3 nanoparticulate films is macroscopically inhomogeneous as shown in Figure S2.2.[18–20]

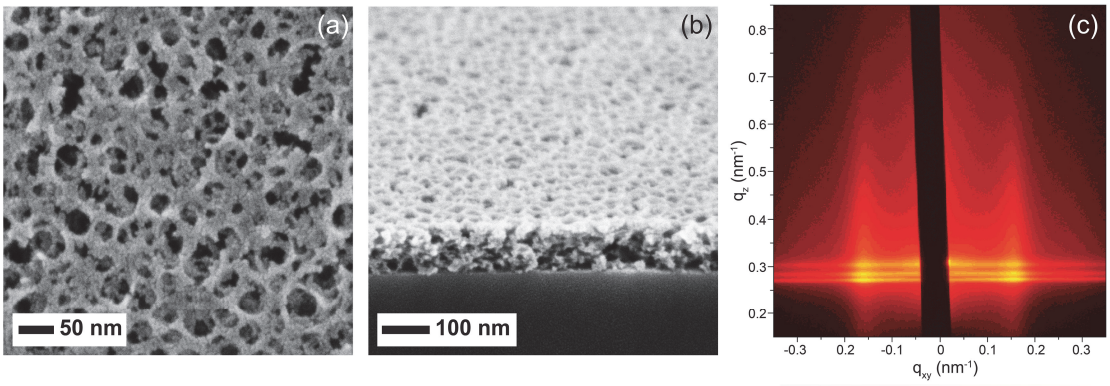

Figure 2.2. (a) Plan view and (b) cross-sectional SEM micrographs, and (c) 2D GISAXS profile at incidence angle of 0.16 °of MBCP-Al_2O_3 film after calcination.

***In Situ* X-ray Characterization of MBCP-Al_2O_3 Perovskite Structural Evolution.** The mesoporous support in solution-processed nanostructured

$CH_3NH_3PbX_3$ perovskite solar cells fulfills multiple roles. For example, mesoporous TiO_2 acts as the distributed heterojunction with large surface areas for the generation of charges by the $CH_3NH_3PbI_3$ perovskite absorber, and collects and transports the electrons to the collecting electrode.[10–17,24,32–34] Moreover, mesoporous superstructures improve the coating of perovskite material to enhance coverage and light harvesting efficiency,[19] and act as a physical barrier to prevent the formation of "shunt paths" by direct contact of the hole transport material and electron selective layer.[18–22] We applied *in situ* GIWAXS to study the structural evolution of solution-processed $CH_3NH_3PbI_{3-x}Cl_x$ perovskite on MBCP-Al_2O_3 thin films during annealing in real time.

As mentioned earlier, we observed similar GIWAXS patterns for the 20 wt% and 40 wt% perovskite thin films (Figure 2.1c,d). Here we chose to deposit a 20 wt% perovskite precursor solution on the MBCP-Al_2O_3 thin film for isothermal-time-dependent (ITD) annealing in air and nitrogen, respectively. The precursor solution filled the interconnected mesopores and formed a "wet capping layer" on the superstructure scaffold with incomplete solvent removal. After deposition the sample was immediately loaded on a sample-stage held at 100 °C. It should be noted that in this way the ITD MBCP-Al_2O_3 perovskite samples underwent an immediate jump from ambient temperature to 100 °C. GIWAXS measurements were collected in real time over a dwell of 50 min. In the employed beam configuration, GIWAXS measured the perovskite material within the MBCP-Al_2O_3 scaffold and capping layer as the incidence angle of the incoming X-ray beam was above the critical angle of the silicon substrate. *In situ* 2D GIWAXS profiles and azimuthally integrated intensity plots of the ITD MBCP-Al_2O_3 perovskite structural evolution in nitrogen and air, respectively, are shown in Figure 2.3.

For the study of the ITD MBCP-Al_2O_3 perovskite behavior in nitrogen, the wet

sample was loaded into a custom-made environmental chamber on the heated stage at 100 °C under flowing nitrogen.[58] Under these conditions, the wet sample exhibits multiple orders of scattering rings in the GIWAXS profile (Figure 2.3a), indicating the formation of crystalline material. Interestingly, from the integrated intensity plots in Figure 2.3c, at short times (3 min time point) we observe a distinct set of scattering peaks at lower q values (<9 nm^{-1}) that are neither characteristic for CH_3NH_3I, $PbCl_2$, PbI_2, nor for the $CH_3NH_3PbI_{3-x}Cl_x$ perovskite structure. After 10 minutes the expected peaks for the mixed halide perovskite are observed (compare Figure 2.3c with Figure 2.1e). This observation suggests the formation of a distinct crystalline structure, which in the following discussion we will refer to as the "crystalline precursor structure". We assigned the peak at $q \approx 11$ nm^{-1} as the signature scattering peak for this crystalline precursor structure. Further investigation is currently underway to identify the structure of this crystalline precursor material. Somewhere between 3 and 10 min of annealing in nitrogen under the set conditions, the film underwent a transition to form the mixed halide perovskite structure, at which point the intensity of the peak at $q \approx 11$ nm^{-1} for the crystalline precursor in Figure 2.3c vanishes. The film started to degrade into PbI_2 after about 20-30 min of annealing, as indicated by the appearance of a scattering peak at $q = 9$ nm^{-1}. The degradation may be attributed to the presence of moisture in the chamber,[13,22,23,54,56] but at this point X-ray beam induced damage cannot be excluded either. For comparison, Figure 2.3b shows the GIWAXS profile of the MBCP-Al_2O_3 perovskite film after 50 min annealing in nitrogen at 100 °C.

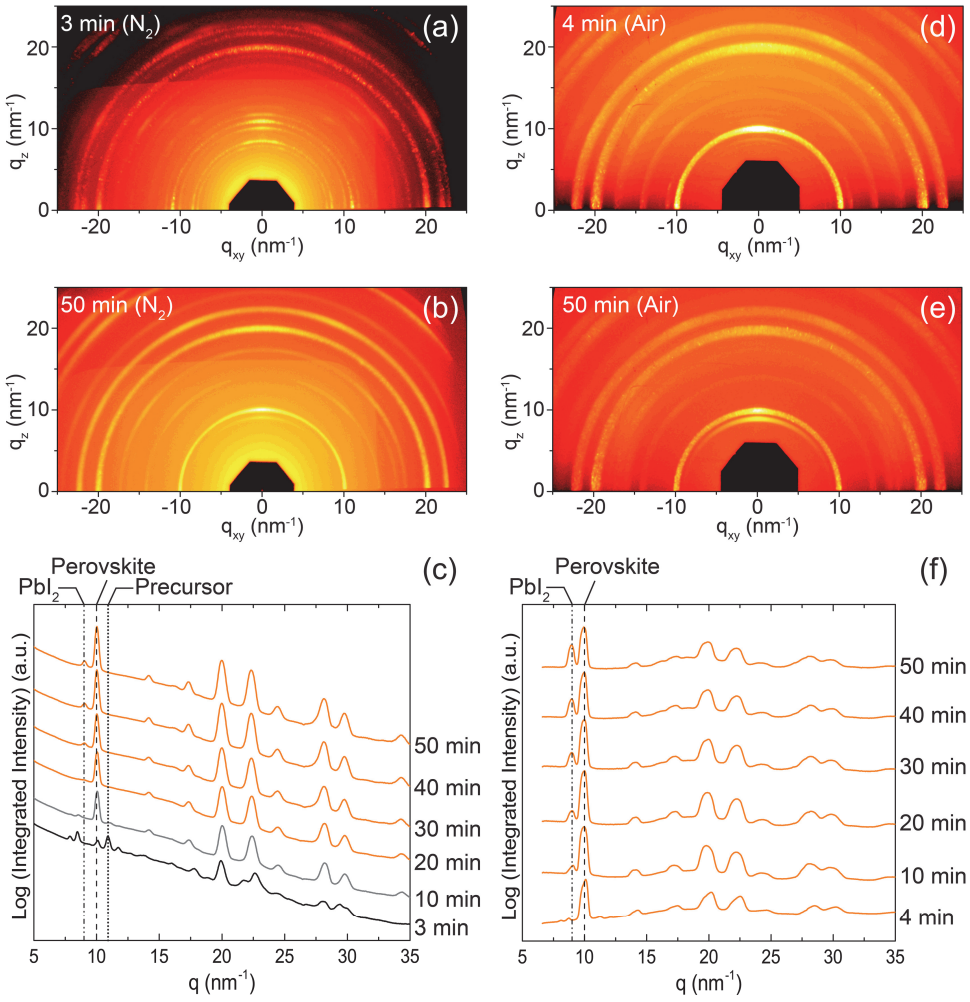

Figure 2.3. 2D GIWAXS profiles for ITD annealing of MBCP-Al_2O_3 perovskite films at 100 °C in (a, b) nitrogen and (d, e) air for different time points as indicated, together with (c, f) respective azimuthally integrated intensity plots. The dotted line at $q \approx 11$ nm^{-1}, dashed line at $q = 10$ nm^{-1}, and dash-dotted line at $q = 9$ nm^{-1} denote the signature scattering peaks for the crystalline precursor, perovskite, and PbI_2 structures, respectively.

From the beginning of ITD annealing at 100 °C in air, we observe multiple orders of scattering rings in the GIWAXS profile (Figure 2.3d), consistent with the rapid formation of a polycrystalline perovskite phase in the presence of MBCP-Al_2O_3. Figure

2.3f shows the azimuthally integrated intensity plot of the ITD experiments in air with the perovskite signature peak at q = 10 nm^{-1}. Within 10 min at 100 °C, the perovskite started to degrade to PbI_2 as signified by the new peak formed at q = 9 nm^{-1}. The degradation is likely to initiate from the perovskite film surface[56] and may be attributed to moisture in the air[13,22,23,54] and X-ray beam induced damage. Over the dwell of 50 min at 100 °C, the scattering peaks remained in the same positions as shown in Figure 2.3e,f, suggesting minimal reorientation changes to the perovskite structure. Under air the perovskite structure already showed first indications of degradation *via* the peak at q = 9 nm^{-1} by the 10 min time point. We suspect that the absence of the crystalline precursor structure may be due to a more rapid transition in air as compared to nitrogen. We observe similar behavior, *i.e.* the absence of the crystalline precursor for $CH_3NH_3PbI_{3-x}Cl_x$ on a MBCP-TiO_2 superstructure annealed in air, albeit with more severe degradation into PbI_2 (Figure S2.3).

To delineate how individual parameters contribute to the structural evolution of $CH_3NH_3PbI_{3-x}Cl_x$ on MBCP-Al_2O_3, we conducted time-temperature-dependent (TTD) GIWAXS measurements with a slow temperature ramp applied to the wet MBCP-Al_2O_3 perovskite sample in nitrogen. To that end, 20 wt% precursor solution was deposited on the MBCP-Al_2O_3 thin film and loaded into the environmental chamber held at 30 °C under flowing nitrogen. The temperature of the heating stage was raised by 10 °C at every 10 min time interval. It took approximately 2-3 min for the heated stage to reach the set temperature. Figure 2.4 displays four representative 2D GIWAXS profiles (a-d) while the integrated intensity plots (e) reveal the TTD structural evolution of the MBCP-Al_2O_3 perovskite sample from 30-100 °C over the dwell of 120 min.

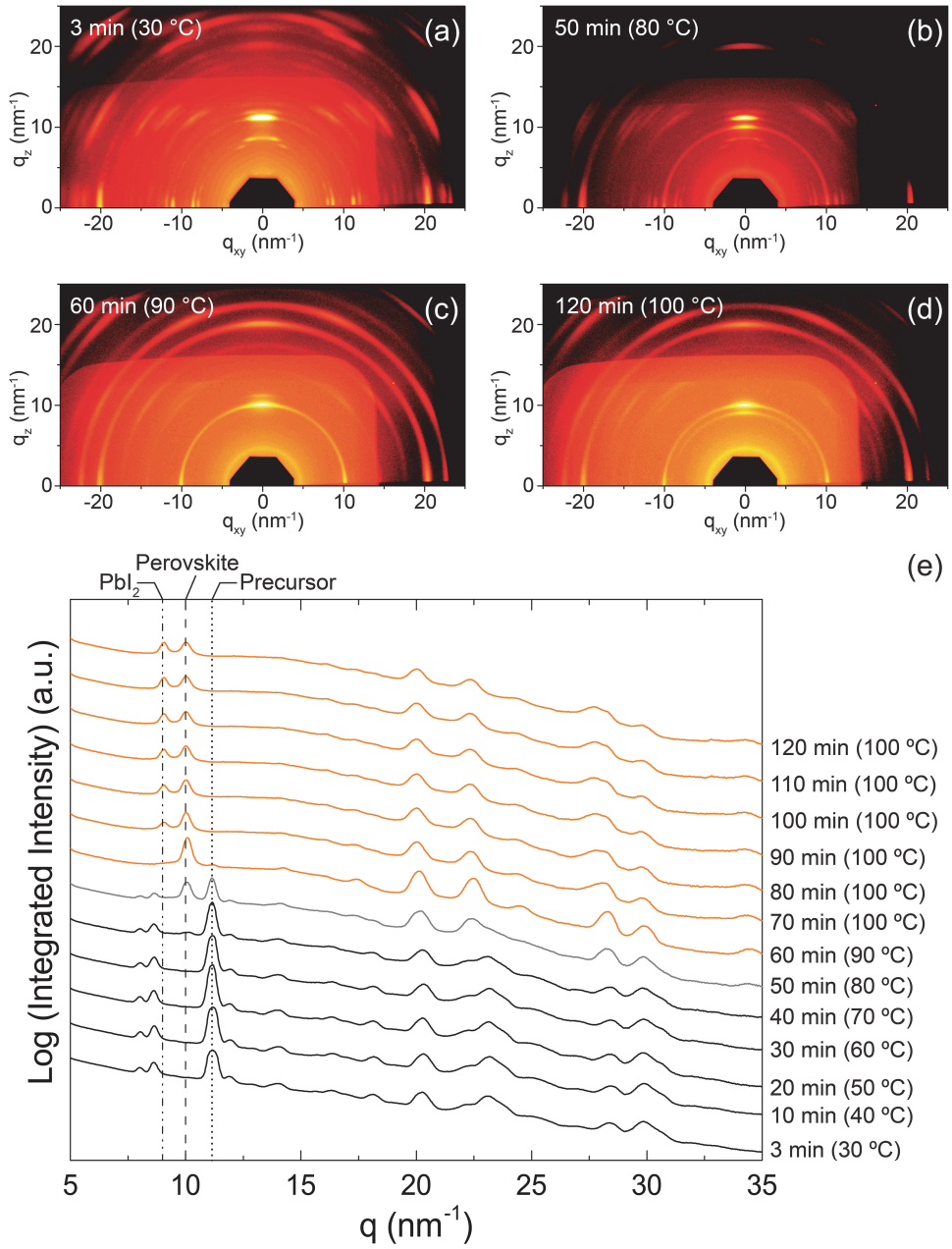

Figure 2.4. 2D GIWAXS profiles for TTD annealing of MBCP-Al_2O_3 perovskite films in nitrogen after (a) 3 min, (b) 50 min, (c) 60 min and (d) 120 min, together with (e) azimuthally integrated intensity plots. The dotted line at $q \approx 11$ nm^{-1}, dashed line at $q = 10$ nm^{-1}, and dash-dotted line at $q = 9$ nm^{-1} denote the signature scattering peaks for the crystalline precursor, perovskite, and PbI_2 structures, respectively. The difference in background brightness of the GIWAXS patterns is a shadow artifact of the experimental setup.

At the beginning of the experiment, the crystalline precursor was detected in the GIWAXS profile *via* the peak at $q \approx 11$ nm^{-1}, see also GIWAXS pattern in Figure 2.4a showing results for the 3 min (30 °C) time point. At the 50 min time point (80 °C) a scattering ring appeared at $q = 10$ nm^{-1} (Figure 2.4b), indicating the transition from the crystalline precursor to polycrystalline perovskite. This structural transition was completed at the 60 min time point (90 °C, Figure 2.4c), similar to the 10 min time point for the ITD annealed MBCP-Al_2O_3 perovskite at 100 °C in nitrogen (compare with Figure 2.3c). Perovskite film degradation was observed at the 70 min time point after the temperature was raised to the final value of 100 °C, and progressed till the final time point at 120 min (Figure 2.4d). Similar to the ITD annealing in nitrogen, three distinct structures were identified during the TTD processing of $CH_3NH_3PbI_{3-x}Cl_x$ in MBCP-Al_2O_3 superstructures: (1) crystalline precursor, (2) perovskite, and (3) PbI_2 as a perovskite degradation product.

From the present and previous work, we conclude that transitions between these different structures are driven by a combination of annealing temperature, environmental atmosphere and film thickness.[22,26,27] A yet-to-be identified crystalline precursor structure was observed upon spin coating the $CH_3NH_3PbI_{3-x}Cl_x$ precursor solution on MBCP-Al_2O_3, and displayed noteworthy thermal stability during the TTD ramp annealing. We postulate that the crystalline precursor undergoes a solid-solid phase transformation to the 3D perovskite structure at 80 °C. This transition occurs relatively rapid (<10 min) and is largely completed at 90 °C. To the best of our knowledge, this is the first experimental observation of a transformation from a crystalline precursor to the perovskite crystal structure for methylammonium lead trihalide perovskite materials, suggesting a phase transformation pathway consistent with Ostwald's "Rule of Stages" in which a metastable precursor is first formed,

followed by transformation into the more stable product.[59,60]

We further note that macroscopic coverage of the substrate with perovskite layers is largely affected by the heat treatment profile. In plan view SEM images (Figure S2.4a,b) we observe large (>2 μm) perovskite crystallite islands and pores in the capping layer on MBCP-Al_2O_3 under ITD annealing conditions. In contrast, the discrete perovskite islands and pores are on the sub-micron length scale for the TTD annealed MBCP-Al_2O_3 perovskite film shown in Figure S2.4,e. Since the only difference in the heat treatment profile is at the initial stage before perovskite formation, this result suggests that the crystalline precursor coverage and the subsequent phase transformation contributes significantly to the final film coverage, which in turn greatly affects device performance (*vide infra*).

MBCP-Al_2O_3 Perovskite Solar Cell Performance. Figure 2.5 shows SEM images of MBCP-Al_2O_3 perovskite films prepared from 40 wt% precursor solutions and annealed either instantaneously at 100 °C (ITD), or with a slow temperature ramp to 100 °C (TTD) in nitrogen. While the crystallite domain sizes are very similar for the ITD and TTD annealed films (Figure 2.5c,d), the capping film coverage is drastically different. Figure 2.5a shows that large pores (>1 μm) were formed in the capping layer of the MBCP-Al_2O_3 perovskite films annealed instantly at 100 °C (ITD). In contrast, when the MBCP-Al_2O_3 perovskite film was annealed with a slow temperature ramp of 5 °C / 5 min in nitrogen to 100 °C and held for 45 min at the final temperature (TTD), significantly better perovskite film coverage was achieved. The 40 wt% perovskite film morphology is highly similar to the 20 wt% perovskite films (Figure S2.4). We hypothesize that the crystalline precursor which is present for a longer dwell period during TTD annealing, promotes film formation with fewer macroscopic defects than in ITD annealed films.

We fabricated MBCP-Al_2O_3 perovskite solar cells annealed under ITD and TTD conditions (see Table S2.1). Comparing the best performing MBCP-Al_2O_3 perovskite solar cells in Figure 2.5e, the values of short-circuit current density (J_{SC}), open-circuit voltage (V_{OC}) and fill factor (FF) of the TTD-N_2 device increased by at least 15% relative to the ITD-air device. At the same time, the power conversion efficiency increased from 5.2% to 8.3%. We attribute the device performance improvement to the enhanced perovskite film morphology and coverage, enabling more uniform charge generation and collection, and reduced leakage with less available shunt paths.[19,22,26,27]

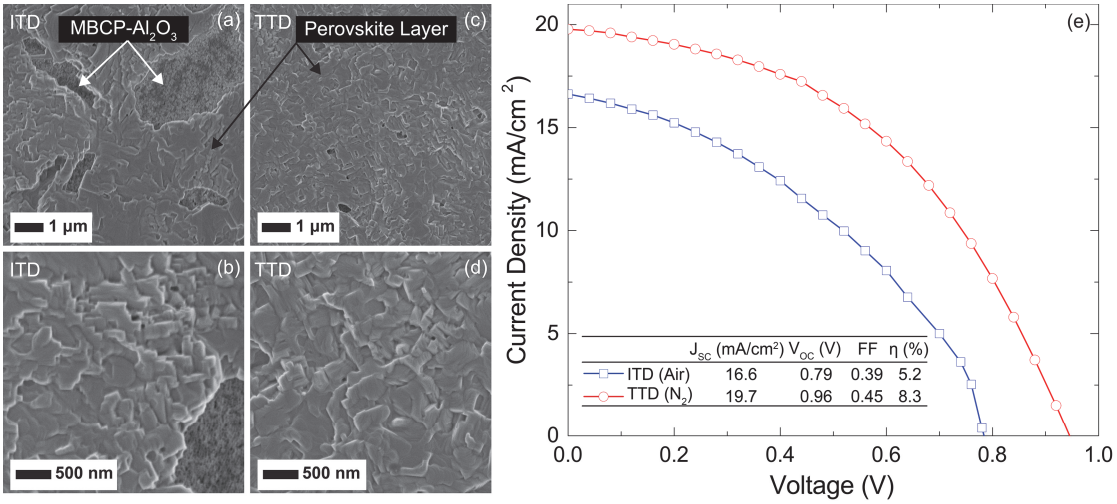

Figure 2.5. Plan view SEM micrographs of perovskite crystallization on MBCP-Al_2O_3 annealed under (a, b) ITD, and (c, d) TTD conditions in nitrogen. (e) Current density/voltage curves of best performing MBCP-Al_2O_3 perovskite solar cells measured under stimulated AM1.5 sunlight of 100 mW/cm^2 irradiation for different annealing conditions (ITD versus TTD).

Conclusion

In conclusion, we employed *in situ* 2D GIWAXS in combination with SEM to

follow the structural evolution of $CH_3NH_3PbI_{3-x}Cl_x$ perovskite on mesoporous block copolymer Al_2O_3 thin films under thermal annealing. Solution-processed perovskite films underwent transitions between three distinct crystalline structures during thermal annealing: a crystalline precursor, a perovskite and a degradation product in the form of PbI_2. Finally, we demonstrated by annealing the MBCP-Al_2O_3 perovskite films with a well-controlled temperature ramp in a dry environment that the perovskite capping film coverage and the power conversion efficiency of block copolymer-directed alumina perovskite solar cells can be greatly improved. To the best of our knowledge, the crystalline precursor has not previously been described and its exact structure is currently unknown. We showed that the evolution between these structures markedly depends on the annealing conditions. A clear understanding of $CH_3NH_3PbX_3$ wet solution processing conditions in combination with bicontinuous BCP gyroidal titania electrodes[37,38] with an interconnecting pore network may allow complete perovskite infiltration, and enhance the photogenerated electron collection and transport for optimal solar cell performance.[24,32–34]

Methods

Materials. All materials were used as received. Anhydrous grades of toluene, *n*-butanol, tetrahydrofuran, chloroform, *N,N*-dimethylformamide and terpineol, 97% aluminum tri-*sec*-butoxide, >97% titanium isopropoxide, 20 wt% aluminum oxide nanoparticles in isopropanol (<50 nm, product number 702129), 57 wt% hydriodic acid in water, 33 wt% methylamine solution in ethanol, and lead chloride were obtained from Sigma-Aldrich. 70% nitric acid and 37% hydrochloric acid were obtained from Mallinckrodt Baker and EMD Millipore, respectively. 10 cP and 46 cP ethyl cellulose were obtained from TCI America.

Mesoporous Block Copolymer-Directed Alumina (MBCP-Al_2O_3) and Titania (MBCP-TiO_2) Films. MBCP-Al_2O_3 thin films were prepared using 50 mg of poly(isoprene)-*block*-poly(styrene)-*block*-poly(ethylene oxide) (ISO, M_n = 38.3 kg/mol, with a polydispersity index of 1.07 containing 68.4 wt% PI and 18.0 wt% PS) dissolved in 500 mg of toluene and *n*-butanol solvent mixture (1:1, w/w). In a separate vial, 104 mg of 97% aluminum tri-*sec*-butoxide, 478 mg of *n*-butanol and 478 mg of toluene were added sequentially. The white cloudy suspension was left undisturbed for 15 min, followed by vigorous stirring for 30 min to allow homogenization. 55 μL of 70% nitric acid was added and the mixture was stirred overnight (>12 h). The transparent alumina sol was added into the ISO solution and stirred for 45 min. The ISO-Al_2O_3 solution was processed by spin coating on silicon at 2000 rpm (45 s) in a nitrogen drybox. The MBCP-Al_2O_3 hybrid thin films were baked at 50 °C (2 h), 100°C (2 h), and 130 °C (2 h) sequentially in the drybox, and calcined in a tube furnace at 450 °C (3 h) with a ramp rate of 1 °C/min.

MBCP-TiO_2 thin films were prepared using a modified method as described elsewhere.[38] Briefly, 50 mg of ISO was dissolved in 1.35 g of tetrahydrofuran and chloroform solvent mixture (4:5, w/w). In a separate vial, 53.9 μL of >97% titanium isopropoxide, 16.8 μL of 37% HCl acid, and 216 μL of tetrahydrofuran were mixed and stirred vigorously. The yellow-colored titania sol was added into the ISO solution and stirred for 45 min. The ISO-TiO_2 solution was processed by spin coating on silicon at 2000 rpm (45 s) in the drybox. The MBCP-TiO_2 hybrid thin films were baked at 50 °C (2 h), 100°C (2 h), and calcined in a tube furnace at 450 °C (3 h) with a ramp rate of 1 °C/min.

Mesoporous Alumina Nanoparticle (NP) Films. Mesoporous Al_2O_3 nanoparticle (NP) thin films were prepared as described elsewhere.[18–20] The binder-free

mesoporous Al_2O_3 NP film was prepared by spin coating 6.67 wt% Al_2O_3 NPs in isopropanol on silicon at 2500 rpm (60 s), and baked at 150 °C (1 h). The 2 wt% Al_2O_3 NP-binder paste was prepared by mixing 1 g of Al_2O_3 NPs, 3.33 g terpineol, 1 g 10 cP ethyl cellulose and 1 g 46 cP ethyl cellulose in 43.67 g isopropanol. The mixture was stirred vigorously at 70 °C for 30 min. The mesoporous Al_2O_3 NP film with binder was prepared by spin coating the Al_2O_3 NP-binder mixture on silicon at 2500 rpm (60 s), and calcined in a tube furnace at 500 °C (3 h) with a ramp rate of 1 °C/min.

Mesoporous Alumina Thin Film Characterization. Scanning electron microscopy (SEM) images were acquired on Au-Pd coated mesoporous alumina thin films using LEO 1550 and TESCAN MIRA3-LM field emission SEMs equipped with in-lens detectors. Atomic force microscopy (AFM) images were obtained on a Veeco Multimode II SPM with a Nanoscope III controller in tapping mode at ambient conditions. GISAXS was measured at the G1 beamline of the Cornell High Energy Synchrotron Source (CHESS). The G1 beamline setup consists of a multilayer monochromator of wavelength $\lambda = 0.1225$ nm with a CCD area detector with a 71.73 μm pixel size and a total of 1024 × 1024 pixels. The sample-to-detector distance was 2.745 m. The incident angle of the beam was varied between 0.1 ° and 0.3 ° with typical exposure times <2 s. GISAXS patterns were analyzed with an in-house software[61] and the FIT2D program.[62]

Wide-Angle X-ray Scattering Measurements of Methylammonium Lead Tri-Iodide/Chloride Hybrid Perovskite. Methylammonium iodide (CH_3NH_3I) was prepared using 57 wt% hydriodic acid (HI) in water and 33 wt% methylamine solution (CH_3NH_2) in ethanol as reported elsewhere.[18] 5-40 wt% of methylammonium iodide (CH_3NH_3I) and lead chloride ($PbCl_2$) (3:1 by molarity) dissolved in *N,N*-dimethylformamide was dispensed on the MBCP-Al_2O_3 and flat glass coverslip

substrates by spin coating at 3000 rpm (45 s) in air. For *ex situ* measurements, the hybrid perovskite samples were annealed by a slow temperature ramp of 10 °C / 10 min and held at 100 °C for 45 min in a nitrogen atmosphere. The annealed perovskite films were carefully scratched from the substrate and powdered for X-ray diffraction (XRD) analysis. The XRD characterization was performed on a Rigaku Ultima IV multipurpose X-ray diffraction system using Cu-Kα radiation (40 kV, 44 mA, wavelength $\lambda = 1.5418$ Å) and unit cell refinement analysis with the MDI Jade 9 software.

For *in situ* GIWAXS measurements, after spin coating the sample was immediately loaded on a temperature-controlled stage at the D1 beamline of CHESS. The D1 beamline setup consists of a multilayer monochromator of wavelength $\lambda = 0.1161$ nm. GIWAXS patterns were collected on Fuji image plates placed in a holder at a distance of 177 mm from the sample. The incident beam angle was above the silicon critical angle (~0.25 °) with exposure times <5 s. The direct beam was blocked with lead tape. The exposed plates were scanned for digital processing with a GE Healthcare Typhoon FLA-7000 image plate reader. Digital images were analyzed using the FIT2D program.[62] The resolution of the letter-sized image plate is 2000 x 2500 pixels with a 100 μm pixel size. The measurements in nitrogen were conducted in a custom-made environmental chamber mounted on the temperature-controlled stage.[58]

Isothermal-Time-Dependent (ITD) Perovskite Crystallization. A 20 wt% precursor solution was dispensed on the MBCP-Al_2O_3 substrate by spin coating and immediately loaded on the temperature-stage held at 100 °C at the D1 beamline. GIWAXS measurements were taken at different time intervals over a dwell of 50 min. The measurements were conducted in ambient air and nitrogen.

Time-Temperature-Dependent (TTD) Perovskite Crystallization. A 20 wt% precursor solution was dispensed on the MBCP-Al_2O_3 substrate by spin coating and

loaded on the temperature-stage held at 30 °C at the D1 beamline. The stage was slowly heated at a ramp rate of 10 °C / 10 min to the final temperature of 100 °C. The MBCP-Al_2O_3 perovskite sample was held at 100 °C for 60 min. The GIWAXS measurements were taken at different time intervals in nitrogen.

MBCP-Al_2O_3 Hybrid Perovskite Solar Cell Assembly. MBCP-Al_2O_3 perovskite solar cells (>20 cells for each annealing history) were fabricated as reported elsewhere.[18] Briefly, HCl-etched FTO glass substrates were coated with a dense TiO_2 compact layer prepared by spin coating a mildly HCl-acidified solution of titanium isopropoxide in ethanol, and sintered at 500 °C for 45 min. The MBCP-Al_2O_3 hybrid films were prepared by spin coating on the TiO_2/FTO substrates at 2000 rpm (45 s). The substrates were baked at 50 °C (2 h), 100°C (2 h), and 130 °C (2 h) sequentially in the drybox and calcined at 450 °C (3 h) with a ramp rate of 1 °C/min.

A 40 wt% perovskite precursor solution was dispensed on the MBCP-Al_2O_3 scaffold by spin coating at 2000 rpm (45 s). For the ITD-air processed MBCP-Al_2O_3 perovskite solar cells, the devices were fabricated in ambient air and heated in a oven at 100 °C for 45 min. For the TTD-nitrogen processed MBCP-Al_2O_3 perovskite solar cells, the devices were fabricated in a nitrogen glovebox. After drying at ambient temperature for at least 20 min, the samples were slowly heated on a hotplate from ambient temperature to 100 °C at a ramp rate of 5 °C / 5 min, and held at 100 °C for 45 min. The electron blocking layer was formed by spin coating 80 mM 2,2',7,7'-tetrakis-(*N,N*-di-*p*-methoxyphenylamine)-9,9'-spirobifluorene (spiro-OMeTAD) in chlorobenzene solution with 68.3 mM *tert*-butylpyridine and 22.6 mM lithium bis(trifluoromethanesulfonyl)imide additives (170 mg/mL in acetonitrile) and aged overnight in a dessicator (in air). Silver contact electrodes of 150 nm were thermally evaporated to complete the devices.

MBCP-Al_2O_3 Hybrid Perovskite Solar Cell Characterization. More than 20 solar cells were measured for each annealing condition (ITD versus TTD) with a Keithley 2400 under AM 1.5G 100 mW/cm^2 simulated sunlight (Abet Technologies Sun 2000) calibrated against an NREL certified KG5 filtered silicon reference diode. The cells were masked with a square aperture defining an active area of typically 0.07 cm^2 and measured in a light-tight sample holder.

Acknowledgement

This work was financially supported by the National Science Foundation (NSF) through the Materials World Network grant between the US (DMR-1008125) and the UK (Engineering and Physical Sciences Research Council, EPSRC). K.W.T. gratefully acknowledges the Singapore Energy Innovation Programme Office for a National Research Foundation graduate fellowship. This work made use of the research facilities of the Cornell Center for Materials Research (CCMR) with support from the NSF Materials Research Science and Engineering Centers (MRSEC) program (DMR-1120296), Cornell High Energy Synchrotron Source (CHESS) which is supported by the NSF and the NIH/National Institute of General Medical Sciences under NSF award DMR-0936384, and the KAUST-Cornell Center for Energy and Sustainability supported by Award No. KUS-C1-018-02, made by King Abdullah University of Science and Technology (KAUST). The authors gratefully acknowledge D. M. Smilgies, M. Koker, R. Li, J. Kim, S. W. Robbins, T. Scott and J. Song of Cornell University for kind experimental assistance.

REFERENCES

(1) Cho, A. Energy's Tricky Tradeoffs. *Science* **2010**, *329*, 786–787.

(2) Graetzel, M.; Janssen, R. A. J.; Mitzi, D. B.; Sargent, E. H. Materials Interface Engineering for Solution-Processed Photovoltaics. *Nature* **2012**, *488*, 304–312.

(3) Ip, A. H.; Thon, S. M.; Hoogland, S.; Voznyy, O.; Zhitomirsky, D.; Debnath, R.; Levina, L.; Rollny, L. R.; Carey, G. H.; Fischer, A.; *et al.* Hybrid Passivated Colloidal Quantum Dot Solids. *Nat. Nanotechn.* **2012**, *7*, 577–582.

(4) Ning, Z.; Zhitomirsky, D.; Adinolfi, V.; Sutherland, B.; Xu, J.; Voznyy, O.; Maraghechi, P.; Lan, X.; Hoogland, S.; Ren, Y.; *et al.* Graded Doping for Enhanced Colloidal Quantum Dot Photovoltaics. *Adv. Mater.* **2013**, *25*, 1719–1723.

(5) Service, R. F. Outlook Brightens for Plastic Solar Cells. *Science* **2011**, *332*, 293–293.

(6) You, J.; Dou, L.; Yoshimura, K.; Kato, T.; Ohya, K.; Moriarty, T.; Emery, K.; Chen, C.-C.; Gao, J.; Li, G.; *et al.* A Polymer Tandem Solar Cell with 10.6% Power Conversion Efficiency. *Nat. Commun.* **2013**, *4*, 1446.

(7) Yella, A.; Lee, H.-W.; Tsao, H. N.; Yi, C.; Chandiran, A. K.; Nazeeruddin, M. K.; Diau, E. W.-G.; Yeh, C.-Y.; Zakeeruddin, S. M.; Grätzel, M. Porphyrin-Sensitized Solar Cells with Cobalt (II/III)–Based Redox Electrolyte Exceed 12 Percent Efficiency. *Science* **2011**, *334*, 629–634.

(8) Han, L.; Islam, A.; Chen, H.; Malapaka, C.; Chiranjeevi, B.; Zhang, S.; Yang, X.; Yanagida, M. High-Efficiency Dye-Sensitized Solar Cell with a Novel Co-Adsorbent. *Energy Environ. Sci.* **2012**, *5*, 6057–6060.

(9) Chung, I.; Lee, B.; He, J.; Chang, R. P. H.; Kanatzidis, M. G. All-Solid-State Dye-Sensitized Solar Cells with High Efficiency. *Nature* **2012**, *485*, 486–489.

(10) Kojima, A.; Teshima, K.; Shirai, Y.; Miyasaka, T. Organometal Halide Perovskites as Visible-Light Sensitizers for Photovoltaic Cells. *J. Am. Chem. Soc.* **2009**, *131*, 6050–6051.

(11) Im, J.-H.; Lee, C.-R.; Lee, J.-W.; Park, S.-W.; Park, N.-G. 6.5% Efficient Perovskite Quantum-Dot-Sensitized Solar Cell. *Nanoscale* **2011**, *3*, 4088–4093.

(12) Kim, H.-S.; Lee, C.-R.; Im, J.-H.; Lee, K.-B.; Moehl, T.; Marchioro, A.; Moon, S.-J.; Humphry-Baker, R.; Yum, J.-H.; Moser, J. E.; *et al.* Lead Iodide Perovskite Sensitized All-Solid-State Submicron Thin Film Mesoscopic Solar Cell with Efficiency Exceeding 9%. *Sci. Rep.* **2012**, *2*, 591.

(13) Noh, J. H.; Im, S. H.; Heo, J. H.; Mandal, T. N.; Seok, S. I. Chemical Management for Colorful, Efficient, and Stable Inorganic–Organic Hybrid Nanostructured Solar Cells. *Nano Lett.* **2013**, *13*, 1764–1769.

(14) Etgar, L.; Gao, P.; Xue, Z.; Peng, Q.; Chandiran, A. K.; Liu, B.; Nazeeruddin, M. K.; Grätzel, M. Mesoscopic $CH_3NH_3PbI_3/TiO_2$ Heterojunction Solar Cells. *J. Am. Chem. Soc.* **2012**, *134*, 17396–17399.

(15) Heo, J. H.; Im, S. H.; Noh, J. H.; Mandal, T. N.; Lim, C.-S.; Chang, J. A.; Lee, Y. H.; Kim, H.; Sarkar, A.; Nazeeruddin, M. K.; *et al.* Efficient Inorganic-Organic Hybrid Heterojunction Solar Cells Containing Perovskite Compound and Polymeric Hole Conductors. *Nat. Photonics* **2013**, *7*, 486–491.

(16) Crossland, E. J. W.; Noel, N.; Sivaram, V.; Leijtens, T.; Alexander-Webber, J. A.;

Snaith, H. J. Mesoporous TiO_2 Single Crystals Delivering Enhanced Mobility and Optoelectronic Device Performance. *Nature* **2013**, *495*, 215–219.

(17) Kim, H.-S.; Mora-Sero, I.; Gonzalez-Pedro, V.; Fabregat-Santiago, F.; Juarez-Perez, E. J.; Park, N.-G.; Bisquert, J. Mechanism of Carrier Accumulation in Perovskite Thin-Absorber Solar Cells. *Nat. Commun.* **2013**, *4*, 2242.

(18) Lee, M. M.; Teuscher, J.; Miyasaka, T.; Murakami, T. N.; Snaith, H. J. Efficient Hybrid Solar Cells Based on Meso-Superstructured Organometal Halide Perovskites. *Science* **2012**, *338*, 643–647.

(19) Ball, J. M.; Lee, M. M.; Hey, A.; Snaith, H. J. Low-Temperature Processed Meso-Superstructured to Thin-Film Perovskite Solar Cells. *Energy Environ. Sci.* **2013**, *6*, 1739–1743.

(20) Edri, E.; Kirmayer, S.; Cahen, D.; Hodes, G. High Open-Circuit Voltage Solar Cells Based on Organic–Inorganic Lead Bromide Perovskite. *J. Phys. Chem. Lett.* **2013**, 897–902.

(21) Zhang, W.; Saliba, M.; Stranks, S. D.; Sun, Y.; Shi, X.; Wiesner, U.; Snaith, H. J. Enhancement of Perovskite-Based Solar Cells Employing Core–Shell Metal Nanoparticles. *Nano Lett.* **2013**, *13*, 4505–4510.

(22) Eperon, G. E.; Burlakov, V. M.; Docampo, P.; Goriely, A.; Snaith, H. J. Morphological Control for High Performance, Solution-Processed Planar Heterojunction Perovskite Solar Cells. *Adv. Funct. Mater.* **2014**, *24*, 151–157.

(23) Colella, S.; Mosconi, E.; Fedeli, P.; Listorti, A.; Gazza, F.; Orlandi, F.; Ferro, P.; Besagni, T.; Rizzo, A.; Calestani, G.; *et al.* $MAPbI_{3-x}Cl_x$ Mixed Halide Perovskite for Hybrid Solar Cells: The Role of Chloride as Dopant on the Transport and Structural Properties. *Chem. Mater.* **2013**, *25*, 4613–4618.

(24) Burschka, J.; Pellet, N.; Moon, S.-J.; Humphry-Baker, R.; Gao, P.; Nazeeruddin, M. K.; Grätzel, M. Sequential Deposition as a Route to High-Performance Perovskite-Sensitized Solar Cells. *Nature* **2013**, *499*, 316–319.

(25) Liu, M.; Johnston, M. B.; Snaith, H. J. Efficient Planar Heterojunction Perovskite Solar Cells by Vapour Deposition. *Nature* **2013**, *501*, 395–398.

(26) Conings, B.; Baeten, L.; De Dobbelaere, C.; D'Haen, J.; Manca, J.; Boyen, H.-G. Perovskite-Based Hybrid Solar Cells Exceeding 10% Efficiency with High Reproducibility Using a Thin Film Sandwich Approach. *Adv. Mater.* **2014**, *26*, 2041–2046.

(27) Jeng, J.-Y.; Chiang, Y.-F.; Lee, M.-H.; Peng, S.-R.; Guo, T.-F.; Chen, P.; Wen, T.-C. $CH_3NH_3PbI_3$ Perovskite/Fullerene Planar-Heterojunction Hybrid Solar Cells. *Adv. Mater.* **2013**, *25*, 3727–3732.

(28) Stranks, S. D.; Eperon, G. E.; Grancini, G.; Menelaou, C.; Alcocer, M. J. P.; Leijtens, T.; Herz, L. M.; Petrozza, A.; Snaith, H. J. Electron-Hole Diffusion Lengths Exceeding 1 Micrometer in an Organometal Trihalide Perovskite Absorber. *Science* **2013**, *342*, 341–344.

(29) Xing, G.; Mathews, N.; Sun, S.; Lim, S. S.; Lam, Y. M.; Grätzel, M.; Mhaisalkar, S.; Sum, T. C. Long-Range Balanced Electron- and Hole-Transport Lengths in Organic-Inorganic $CH_3NH_3PbI_3$. *Science* **2013**, *342*, 344–347.

(30) Liu, D.; Kelly, T. L. Perovskite Solar Cells with a Planar Heterojunction Structure Prepared Using Room-Temperature Solution Processing Techniques. *Nat. Photonics* **2014**, *8*, 133–138.

(31) You, J.; Hong, Z.; Yang, Y. (Michael); Chen, Q.; Cai, M.; Song, T.-B.; Chen, C.-C.; Lu, S.; Liu, Y.; Zhou, H.; *et al.* Low-Temperature Solution-Processed Perovskite Solar Cells

with High Efficiency and Flexibility. *ACS Nano* **2014**, *8*, 1674–1680.

(32) Edri, E.; Kirmayer, S.; Henning, A.; Mukhopadhyay, S.; Gartsman, K.; Rosenwaks, Y.; Hodes, G.; Cahen, D. Why Lead Methylammonium Tri-Iodide Perovskite-Based Solar Cells Require a Mesoporous Electron Transporting Scaffold (but Not Necessarily a Hole Conductor). *Nano Lett.* **2014**, *14*, 1000–1004.

(33) Gonzalez-Pedro, V.; Juarez-Perez, E. J.; Arsyad, W.-S.; Barea, E. M.; Fabregat-Santiago, F.; Mora-Sero, I.; Bisquert, J. General Working Principles of $CH_3NH_3PbX_3$ Perovskite Solar Cells. *Nano Lett.* **2014**, *14*, 888–893.

(34) Marchioro, A.; Teuscher, J.; Friedrich, D.; Kunst, M.; van de Krol, R.; Moehl, T.; Grätzel, M.; Moser, J.-E. Unravelling the Mechanism of Photoinduced Charge Transfer Processes in Lead Iodide Perovskite Solar Cells. *Nat. Photonics* **2014**, 8, 250-255.

(35) Kagan, C. R.; Mitzi, D. B.; Dimitrakopoulos, C. D. Organic-Inorganic Hybrid Materials as Semiconducting Channels in Thin-Film Field-Effect Transistors. *Science* **1999**, *286*, 945–947.

(36) Mitzi, D. B.; Chondroudis, K.; Kagan, C. R. Organic-Inorganic Electronics. *IBM J. Res. Dev.* **2001**, *45*, 29–45.

(37) Crossland, E. J. W.; Kamperman, M.; Nedelcu, M.; Ducati, C.; Wiesner, U.; Smilgies, D.-M.; Toombes, G. E. S.; Hillmyer, M. A.; Ludwigs, S.; Steiner, U.; *et al.* A Bicontinuous Double Gyroid Hybrid Solar Cell. *Nano Lett.* **2009**, *9*, 2807–2812.

(38) Docampo, P.; Stefik, M.; Guldin, S.; Gunning, R.; Yufa, N. A.; Cai, N.; Wang, P.; Steiner, U.; Wiesner, U.; Snaith, H. J. Triblock-Terpolymer-Directed Self-Assembly of Mesoporous TiO_2: High-Performance Photoanodes for Solid-State Dye-Sensitized Solar Cells. *Adv. Energy Mater.* **2012**, *2*, 676–682.

(39) Polman, A.; Atwater, H. A. Photonic Design Principles for Ultrahigh-Efficiency Photovoltaics. *Nat. Mater.* **2012**, *11*, 174–177.

(40) Lunt, R. R.; Osedach, T. P.; Brown, P. R.; Rowehl, J. A.; Bulović, V. Practical Roadmap and Limits to Nanostructured Photovoltaics. *Adv. Mater.* **2011**, *23*, 5712–5727.

(41) Orilall, M. C.; Wiesner, U. Block Copolymer Based Composition and Morphology Control in Nanostructured Hybrid Materials for Energy Conversion and Storage: Solar Cells, Batteries, and Fuel Cells. *Chem. Soc. Rev.* **2011**, *40*, 520–535.

(42) Templin, M.; Franck, A.; Chesne, A. D.; Leist, H.; Zhang, Y.; Ulrich, R.; Schädler, V.; Wiesner, U. Organically Modified Aluminosilicate Mesostructures from Block Copolymer Phases. *Science* **1997**, *278*, 1795–1798.

(43) Guo, C.; Lin, Y.-H.; Witman, M. D.; Smith, K. A.; Wang, C.; Hexemer, A.; Strzalka, J.; Gomez, E. D.; Verduzco, R. Conjugated Block Copolymer Photovoltaics with near 3% Efficiency through Microphase Separation. *Nano Lett.* **2013**, *13*, 2957–2963.

(44) Kuemmel, M.; Grosso, D.; Boissière, C.; Smarsly, B.; Brezesinski, T.; Albouy, P. A.; Amenitsch, H.; Sanchez, C. Thermally Stable Nanocrystalline γ-Alumina Layers with Highly Ordered 3D Mesoporosity. *Angew. Chem. Int. Ed.* **2005**, *44*, 4589–4592.

(45) Oveisi, H.; Jiang, X.; Imura, M.; Nemoto, Y.; Sakamoto, Y.; Yamauchi, Y. A Mesoporous γ-Alumina Film with Vertical Mesoporosity: The Unusual Conversion from a $Im\bar{3}m$ Mesostructure to Vertically Oriented γ-Alumina Nanowires. *Angew. Chem. Int. Ed.* **2011**, *50*, 7410–7413.

(46) Jiang, X.; Suzuki, N.; Bastakoti, B. P.; Wu, K. C.-W.; Yamauchi, Y. Synthesis of Continuous Mesoporous Alumina Films with Large-Sized Cage-Type Mesopores by Using

Diblock Copolymers. *Chem. Asian J.* **2012**, *7*, 1713–1718.

(47) Guldin, S.; Kolle, M.; Stefik, M.; Langford, R.; Eder, D.; Wiesner, U.; Steiner, U. Tunable Mesoporous Bragg Reflectors Based on Block-Copolymer Self-Assembly. *Adv. Mater.* **2011**, *23*, 3664–3668.

(48) Rauda, I. E.; Buonsanti, R.; Saldarriaga-Lopez, L. C.; Benjauthrit, K.; Schelhas, L. T.; Stefik, M.; Augustyn, V.; Ko, J.; Dunn, B.; Wiesner, U.; *et al.* General Method for the Synthesis of Hierarchical Nanocrystal-Based Mesoporous Materials. *ACS Nano* **2012**, *6*, 6386–6399.

(49) Buonsanti, R.; Pick, T. E.; Krins, N.; Richardson, T. J.; Helms, B. A.; Milliron, D. J. Assembly of Ligand-Stripped Nanocrystals into Precisely Controlled Mesoporous Architectures. *Nano Lett.* **2012**, *12*, 3872–3877.

(50) Nedelcu, M.; Lee, J.; Crossland, E. J. W.; Warren, S. C.; Orilall, M. C.; Guldin, S.; Hüttner, S.; Ducati, C.; Eder, D.; Wiesner, U.; *et al.* Block Copolymer Directed Synthesis of Mesoporous TiO_2 for Dye-Sensitized Solar Cells. *Soft Matter* **2009**, *5*, 134–139.

(51) Arora, H.; Du, P.; Tan, K. W.; Hyun, J. K.; Grazul, J.; Xin, H. L.; Muller, D. A.; Thompson, M. O.; Wiesner, U. Block Copolymer Self-Assembly–Directed Single-Crystal Homo- and Heteroepitaxial Nanostructures. *Science* **2010**, *330*, 214–219.

(52) Guldin, S.; Hüttner, S.; Tiwana, P.; Orilall, M. C.; Ülgüt, B.; Stefik, M.; Docampo, P.; Kolle, M.; Divitini, G.; Ducati, C.; *et al.* Improved Conductivity in Dye-Sensitised Solar Cells through Block-Copolymer Confined TiO_2 Crystallisation. *Energy Environ. Sci.* **2010**, *4*, 225–233.

(53) Hur, K.; Francescato, Y.; Giannini, V.; Maier, S. A.; Hennig, R. G.; Wiesner, U. Three-Dimensionally Isotropic Negative Refractive Index Materials from Block Copolymer Self-Assembled Chiral Gyroid Networks. *Angew. Chem. Int. Ed.* **2011**, *50*, 11985–11989.

(54) Baikie, T.; Fang, Y.; Kadro, J. M.; Schreyer, M.; Wei, F.; Mhaisalkar, S. G.; Graetzel, M.; White, T. J. Synthesis and Crystal Chemistry of the Hybrid Perovskite $(CH_3NH_3)PbI_3$ for Solid-State Sensitised Solar Cell Applications. *J. Mater. Chem. A* **2013**, *1*, 5628–5641.

(55) Poglitsch, A.; Weber, D. Dynamic Disorder in Methylammoniumtrihalogenoplumbates (II) Observed by Millimeter-wave Spectroscopy. *J. Chem. Phys.* **1987**, *87*, 6373–6378.

(56) Stoumpos, C. C.; Malliakas, C. D.; Kanatzidis, M. G. Semiconducting Tin and Lead Iodide Perovskites with Organic Cations: Phase Transitions, High Mobilities, and Near-Infrared Photoluminescent Properties. *Inorg. Chem.* **2013**, *52*, 9019–9038.

(57) Busch, P.; Rauscher, M.; Smilgies, D.-M.; Posselt, D.; Papadakis, C. M. Grazing-Incidence Small-Angle X-Ray Scattering from Thin Polymer Films with Lamellar Structures – the Scattering Cross Section in the Distorted-Wave Born Approximation. *J. Appl. Crystallogr.* **2006**, *39*, 433–442.

(58) Bian, K.; Choi, J. J.; Kaushik, A.; Clancy, P.; Smilgies, D.-M.; Hanrath, T. Shape-Anisotropy Driven Symmetry Transformations in Nanocrystal Superlattice Polymorphs. *ACS Nano* **2011**, *5*, 2815–2823.

(59) D. Yoreo, J.; Vekilov, P. G. Principles of Crystal Nucleation and Growth. In *Biomineralization*; Dove, P. M.; De Yoreo, J.; Weiner, S.; Mineralogical Society of America: Washington, DC, 2003; Vol. 54, pp 57-93.

(60) Vekilov, P. G. Nucleation. *Cryst. Growth Des.* **2010**, *10*, 5007–5019.

(61) Smilgies, D.-M.; Blasini, D. R. Indexation Scheme for Oriented Molecular Thin Films

Studied with Grazing-Incidence Reciprocal-Space Mapping. *J. Appl. Crystallogr.* **2007**, *40*, 716–718.

(62) Hammersley, A. P.; Svensson, S. O.; Hanfland, M.; Fitch, A. N.; Hausermann, D. Two-Dimensional Detector Software: From Real Detector to Idealised Image or Two-Theta Scan. *High Pressure Res.* **1996**, *14*, 235–248.

APPENDIX A

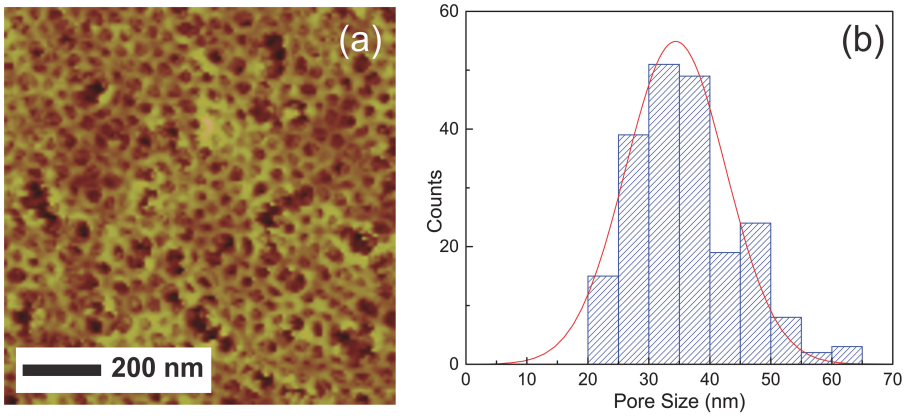

Figure S2.1. (a) AFM surface profile of the MBCP-Al_2O_3 film. (b) Histogram of the MBCP-Al_2O_3 pore size distribution. A Gaussian fitting curve is added to guide the eye.

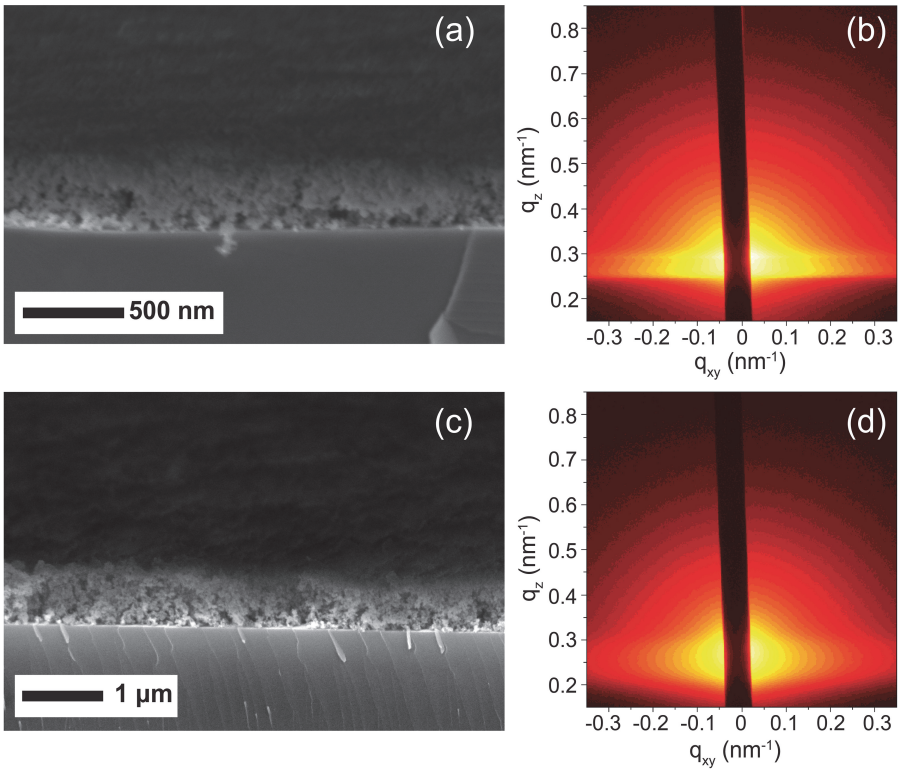

Figure S2.2. Cross-sectional SEM micrographs and GISAXS profiles of (a, b) binder-free Al_2O_3 and (c, d) Al_2O_3 with binder nanoparticulate (NP) films measured at incidence angle of 0.18 °. The in-plane porosity in the Al_2O_3 NP films is macroscopically inhomogeneous.

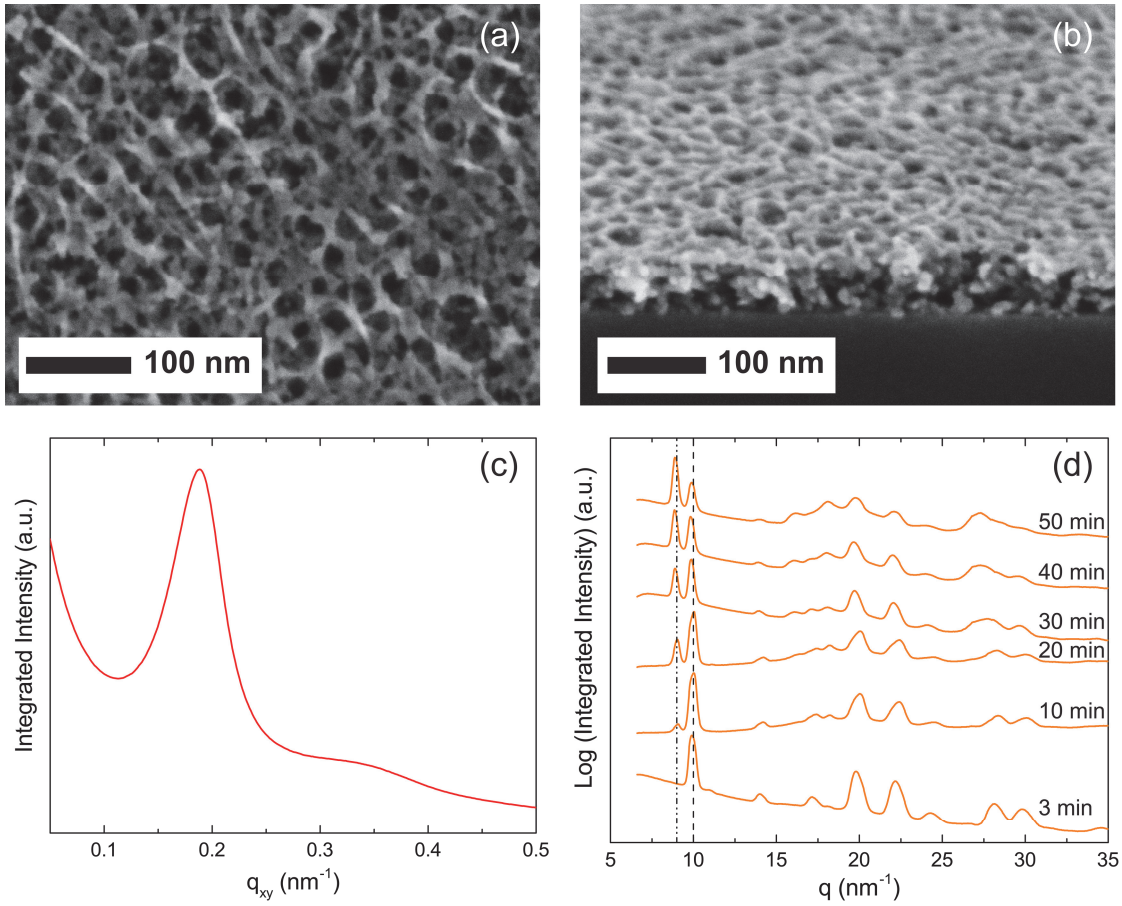

Figure S2.3. (a) Plan view and (b) cross-sectional SEM micrographs of MBCP-TiO_2 film. (c) Integrated intensity plot of GISAXS profile of MBCP-TiO_2 measured at an incidence angle of 0.16 °. The first scattering peak at q_{xy} = 0.189 nm^{-1} provides a macroscopically homogeneous in-plane d-spacing of $2\pi/q_{xy} \approx 33$ nm. (d) *In situ* GIWAXS azimuthally integrated intensity plots of $CH_3NH_3PbI_{3-x}Cl_x$ perovskite on MBCP-TiO_2 as observed under ITD annealing at 100 °C in air.

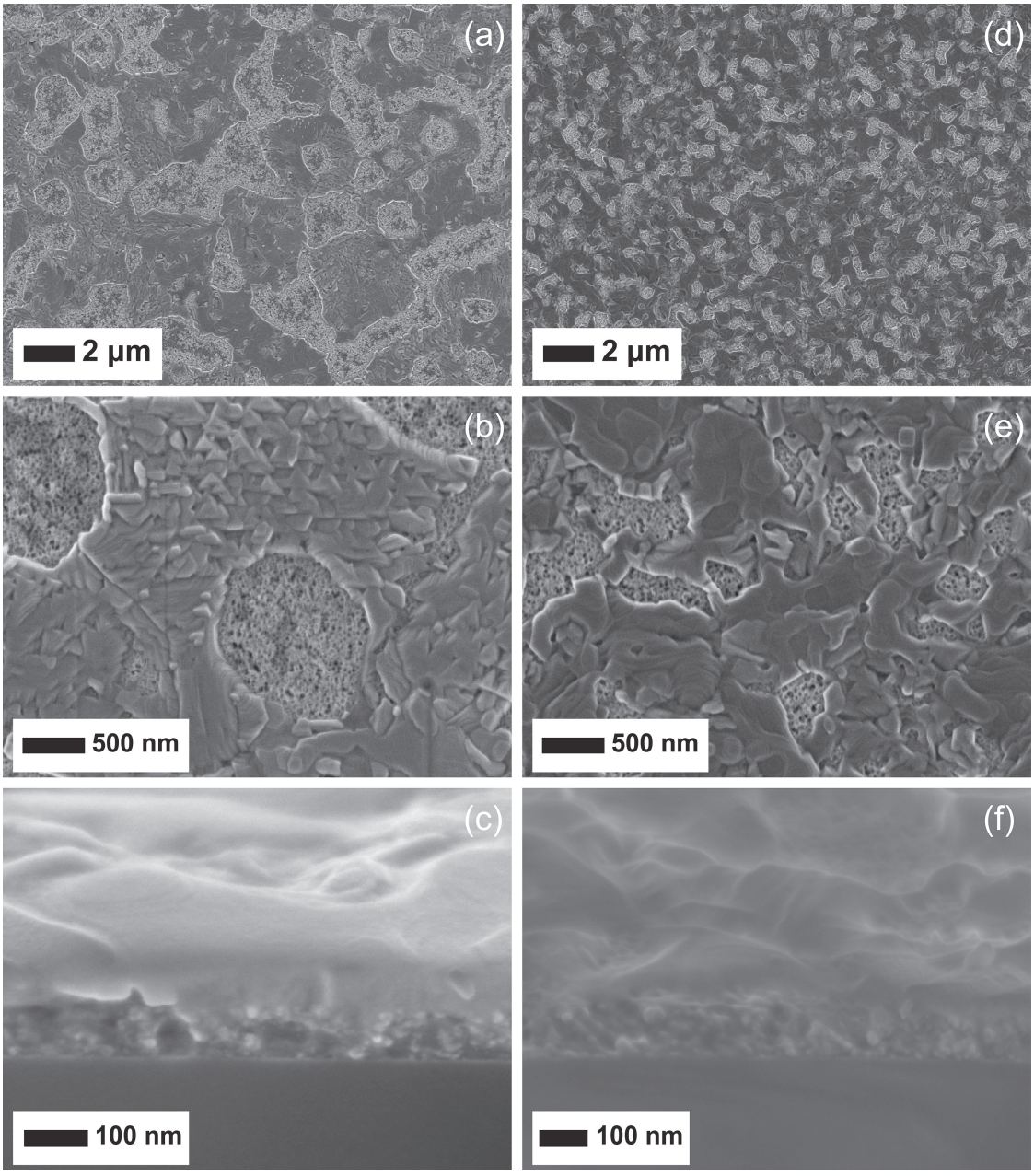

Figure S2.4. Plan view and cross-sectional SEM micrographs of 20 wt% perovskite on MBCP-Al_2O_3 prepared by (a-c) ITD (100 °C for 45 min), and (d-f) TTD (5 °C / 5 min ramp rate, 100 °C for 45 min) annealing in nitrogen. Large perovskite crystallite islands and pore regions were observed for the ITD annealed MBCP-Al_2O_3 perovskite films compared to the TTD annealed samples.

Table S2.1. MBCP-Al_2O_3 perovskite solar cell performance parameters averaged over a batch of at least 20 devices measured under 100 mW/cm^2 stimulated AM1.5 sunlight irradiation.

	Short-circuit density current (mA/cm^2)	Open-circuit voltage (V)	Fill factor	Power conversion efficiency (%)
ITD-annealed in air	13.7 ± 1.7	0.73 ± 0.08	0.36 ± 0.06	3.6 ± 1.0
TTD-annealed in N_2	15.7 ± 2.9	0.94 ± 0.02	0.44 ± 0.05	6.3 ± 1.2

CHAPTER 3

THE INFLUENCE OF THERMAL PROCESSING PROTOCOL UPON THE CRYSTALLIZATION AND PHOTOVOLTAIC PERFORMANCE OF ORGANIC-INORGANIC LEAD TRIHALIDE PEROVSKITES

Abstract

In this work, we investigate the thermally-induced morphological and crystalline development of methylammonium lead mixed halide perovskite ($CH_3NH_3PbI_{3-x}Cl_x$) thin films and photovoltaic device performance with meso-superstructured and planar heterojunction architectures. We observe that a short rapid thermal annealing at 130 °C leads to the growth of large micron-sized textured perovskite domains and improved the short circuit currents and power conversion efficiencies up to 13.5% for the planar heterojunction perovskite solar cells. This work highlights the criticality of controlling the thin film crystallization mechanism of hybrid perovskite materials for high-performing photovoltaic applications.

Reproduced with permission from Saliba, M.[*], Tan, K. W.[*], Sai, H., Moore, D. M., Scott, T., Zhang, W., Estroff, L. A., Wiesner, U. & Snaith, H. J. Influence of thermal processing protocol upon the crystallization and photovoltaic performance of organic–inorganic lead trihalide perovskites. *J. Phys. Chem. C* (2014). doi:10.1021/jp500717w. Copyright 2014 American Chemical Society.
([*]These authors contributed equally to this work.)

Introduction

Organic-inorganic hybrid perovskites, previously investigated for field-effect transistors and light emitting applications,[1,2] have emerged in recent years at the forefront of solution-processable and abundant thin-film photovoltaic technologies yielding power conversion efficiencies (PCEs) over 15%.[3–9] The methylammonium trihalide[10] ($CH_3NH_3PbX_3$, X = Cl, Br, I) perovskite-based solar cells[11–35] have undergone a number of changes in the selection of materials and designs of device configuration; for example the first embodiment, the electrolyte based sensitizer configuration using a mesoporous TiO_2 photoanode (essentially a dye-sensitized solar cell[36] where the dye is replaced by the hybrid perovskite),[11,12] the solid-state sensitized approach,[14,15] the meso-superstructured device configuration consisting of a mesoporous alumina insulator scaffold,[15] or the scaffold-less planar heterojunction configuration.[16]

Recent investigations into the perovskite film morphology formation have provided insights towards identifying key parameters to attain consistently high-performing solar cells. Park and co-workers spin coated 10-40 wt% of $CH_3NH_3PbI_3$ dissolved in γ-butyrolactone on a 5.5 μm thick mesoporous titania photoanode, forming 2-3 nm perovskite nanocrystals after annealing at 40-160 °C.[12] Graetzel and colleagues utilized a two-step sequential process by first depositing PbI_2 on a 350 nm thick mesoporous TiO_2 layer, and subsequent dip-coating into a solution of CH_3NH_3I precursor in isopropanol to grow ~22 nm $CH_3NH_3PbI_3$ nanocrystallites.[20,37] The nanoporous nature and large surface area of the titania film enabled ultrafast growth of perovskite crystals within the pores and high performing devices of over 15% PCE.[20] Even the removal of the mesoporous scaffold did not deter high performances of planar heterojunction perovskite-based solar cells and recent investigations of vapor

deposition[16] and solution processing[28] have demonstrated over 15% PCE. Despite the distinction in the state of the precursors (liquid versus vapor), the resulting hybrid perovskite films to date fulfill similar criteria: high film uniformity and coverage, and large perovskite crystallites (100-1000 nm) to harness the excellent carrier properties.[16,23–29,33,38]

In this work, we prepared methylammonium lead mixed halide ($CH_3NH_3PbI_{3-x}Cl_x$) perovskites with different crystal domain sizes *via* a direct single-step spin coating process, followed by growth under different thermal annealing conditions. We subsequently correlated the resulting film morphologies with performances in alumina-based meso-superstructured and planar heterojunction solar cell architectures.

Experimental Section

Materials. All materials were used as received. Anhydrous grades of toluene, *n*-butanol, *N,N*-dimethylformamide, 97% aluminum tri-*sec*-butoxide, 20 wt% aluminum oxide nanoparticles in isopropanol (<50 nm, product number 702129), 57 wt% hydriodic acid in water, 33 wt% methylamine solution in ethanol, and lead chloride were obtained from Sigma-Aldrich. 70% nitric acid was obtained from Mallinckrodt Baker.

Mesoporous Block Copolymer-Directed Alumina Thin Films. Mesoporous block copolymer-directed alumina (BCP-Al_2O_3) thin films were prepared using 50 mg of poly(isoprene)-*block*-poly(styrene)-*block*-poly(ethylene oxide) (ISO, M_n = 38.3 kg/mol, with a polydispersity index of 1.07 containing 68.4 wt% PI and 18.0 wt% PS) dissolved in 500 mg of toluene and *n*-butanol solvent mixture (1:1, w/w). In a separate vial, 104 mg of 97% aluminum tri-*sec*-butoxide, 478 mg of *n*-butanol and

478 mg of toluene were added sequentially. The white cloudy suspension was left undisturbed for 15 min, followed by vigorous stirring for 30 min to allow homogenization. 55 μL of 70% nitric acid was added and the mixture was stirred overnight (>12 h). The transparent alumina sol was added into the ISO solution and stirred for 45 min. The ISO-Al_2O_3 solution was prepared by spin coating on silicon at 2000 rpm (45 s) in a nitrogen drybox. The MBCP-Al_2O_3 hybrid thin films were baked at 50 °C (2 h), 100°C (2 h), and 130 °C (2 h) sequentially in the drybox, and calcined in a tube furnace at 450 °C (3 h) with a ramp rate of 1 °C/min. From scanning electron microscopy, the BCP-Al_2O_3 thin film thickness was 70-80 nm.

Mesoporous Alumina Nanoparticle Thin Films. Mesoporous alumina nanoparticle (NP-Al_2O_3) thin films were prepared by spin coating 2.2 wt% of <50 nm Al_2O_3 NPs in isopropanol on silicon at 2500 rpm (60 s), followed by drying at 150 °C for 1 h.[17] From scanning electron microscopy, the NP-Al_2O_3 thin film thickness was ~100 nm.

Methylammonium Lead Tri-Iodide/Chloride ($CH_3NH_3PbI_{3-x}Cl_x$) Perovskite Thin Films. Methylammonium iodide (CH_3NH_3I) was prepared using 57 wt% hydriodic acid (HI) in water and 33 wt% methylamine solution (CH_3NH_2) in ethanol as reported elsewhere.[15] All of the following procedures were conducted in a nitrogen atmosphere. A 40 wt% solution of methylammonium iodide (CH_3NH_3I) and lead chloride ($PbCl_2$) (3:1 by molarity) dissolved in *N,N*-dimethylformamide was spin coated on the BCP-Al_2O_3 films, Al_2O_3-NP films and silicon substrates at 2000 rpm for 45 s. The wet perovskite samples were allowed to dry at ambient temperature for at least 20 min. All samples were slowly heated from ambient temperature to 100 °C at a ramp rate of 5 °C / 5 min on a Fisher Scientific hotplate (product code: 10049552), *i.e.* we increased the hotplate temperature by 5 °C after every 5 min dwell.

We modified the final annealing step to prepare different crystalline perovskite thin film samples. In the "time-temperature-dependent" annealing procedure, the sample was held at 100 °C for 45 min. In the "flash" annealing procedure, the samples were first held at 100 °C for 5 min, then rapidly heated to the final value of 130 °C (<3 min), and held there for another 5 min. The thermally annealed perovskite samples were removed from the hot plate and quenched on a metal block heat-sink at ambient temperature. The different annealing procedures are displayed in Figure S3.1. We note that the time-temperature-dependent annealing step here is not the usual annealing step we have employed in previous studies. Previously unless otherwise stated we have placed the coated substrates directly in an oven or on a hot plate already set at the crystallization temperature, *i.e.* a very short ramp time. Within this manuscript time-temperature-dependent (TTD) is referring to the slow ramp to 100 °C.

Hybrid perovskite solar cell assembly. The hybrid perovskite solar cell devices were prepared with modifications from previous reports.[17,19,24] HCl-etched FTO glass substrates were coated with a dense TiO_2 compact layer prepared by spin coating a mildly HCl-acidified solution of titanium isopropoxide in ethanol, and sintered at 500 °C for 45 min in air.[19] The respective meso-superstructured Al_2O_3 scaffolds were prepared on the TiO_2/FTO substrates as described above.[17] All perovskite samples were prepared by thermal annealing on a hotplate in a nitrogen glovebox as described above. The hole transport material layer was applied in the glovebox by spin coating 80 mM 2,2',7,7'-tetrakis(*N,N*-di-*p*-methoxyphenylamine)-9,9'-spirobifluorene (spiro-OMeTAD) in chlorobenzene solution with 64 mM tert-butylpyridine (tBP) and 24 mM lithium bis(trifluoromethanesulfonyl)imide (Li-TFSI) additives (170 mg/mL in acetonitrile) and aged overnight in a dessicator (in air). Silver contact electrodes of 150 nm thickness were thermally evaporated to complete the devices.

Scanning Electron Microscopy and Grazing Incidence Wide-Angle X-ray Characterization. Scanning electron microscopy (SEM) images were acquired on Au-Pd coated mesoporous alumina thin films and perovskite films using a LEO 1550 SEM equipped with an in-lens detector. The perovskite surface area coverage was estimated using the ImageJ software.[24] Grazing incidence wide-angle X-ray scattering (GIWAXS) was measured at the D1 beamline of the Cornell High Energy Synchrotron Source (CHESS). The D1 beamline setup consists of a multilayer monochromator of wavelength $\lambda = 0.14715$ nm. GIWAXS patterns were collected on a Dectris Pilatus 300k area detector mounted vertically at a distance of ~142 mm from the sample. The incident beam angle was above the silicon critical angle (~0.25 °) and exposure times <5 s. The resolution of the area detector was 487 × 619 pixels with a 172 μm pixel size. The GIWAXS patterns were analyzed using the FIT2D software[39] and displayed in scattering vector q coordinates, where $q = 4\pi\sin\theta/\lambda$, θ is half of the total scattering angle, and λ is the X-ray wavelength.

UV-vis Spectroscopy. UV-vis absorbance measurements were performed on TTD and flash annealed planar perovskite films on microscope glass slides prepared as described above using a Carry 300 Bio (Agilent Technologies) with an integrating sphere accessory.

Photoluminescence Characterization. Time-resolved and time-integrated photoluminescence (PL) spectra of TTD and flash annealed planar perovskite films without spiro-OMeTAD or top electrodes were acquired using a time-correlated single photon counting (TCSPC) setup (FluoTime 300, PicoQuant GmbH). The respective samples were photo-excited through the glass using a 507nm laser head (LDH-P-C-510, PicoQuant GmbH) with pulse duration of 117 ps, fluence of ~0.03 nJ/cm^2, and a repetition rate of 2 MHz. Time-resolved measurements were acquired from emission at

770 nm.

Hybrid Perovskite Solar Cell Characterization. The solar cells were measured with a Keithley 2400 under AM 1.5G 100 mW/cm^2 simulated sunlight (Abet Technologies Sun 2000) calibrated against an NREL certified KG5 filtered silicon reference diode. The cells were masked with a square aperture defining an active area of typically 0.07 cm^2 and measured in a light-tight sample holder.

Results and Discussion

Characterization of $CH_3NH_3PbI_{3-x}Cl_x$ Perovskites. The organic-inorganic nature of $CH_3NH_3PbX_3$ allows high flexibility and simple processing by either vapor deposition, solution processing, or a combination of both. Various groups investigated different processing parameters to optimize the perovskite film formation *via* single-step spin coating, for example probing solute concentration, solvent selection, environmental atmosphere, spin coating speed and annealing conditions.[24–26,29] We recently observed a "crystalline precursor structure" present in films of the mixed halide ($CH_3NH_3PbI_{3-x}Cl_x$) hybrid material prior to a phase transformation to the final perovskite structure during thermal annealing.[29] We postulated the crystalline precursor promotes more controlled perovskite film formation on mesoporous block copolymer-directed alumina (BCP-Al_2O_3) superstructures and planar substrates by annealing *via* a ramp rate.[29]

Figure 3.1 shows results of grazing incidence wide-angle X-ray scattering (GIWAXS) measurements of $CH_3NH_3PbI_{3-x}Cl_x$ perovskite films prepared on different substrates by controlled ramp thermal annealing. A 40 wt% perovskite solution was deposited on ~100 nm mesoporous alumina nanoparticle thin films (NP-Al_2O_3, Figure

3.1a,b), 70-80 nm mesoporous block copolymer-directed alumina thin films (BCP-Al_2O_3, Figure 3.1c) and planar silicon substrates (Figure 3.1d) in nitrogen atmosphere. After drying at ambient temperature, all the perovskite samples were slowly heated from ambient temperature to 100 °C at a ramp rate of 5 °C / 5 min to promote uniform film formation (see Figure S3.1).[29]

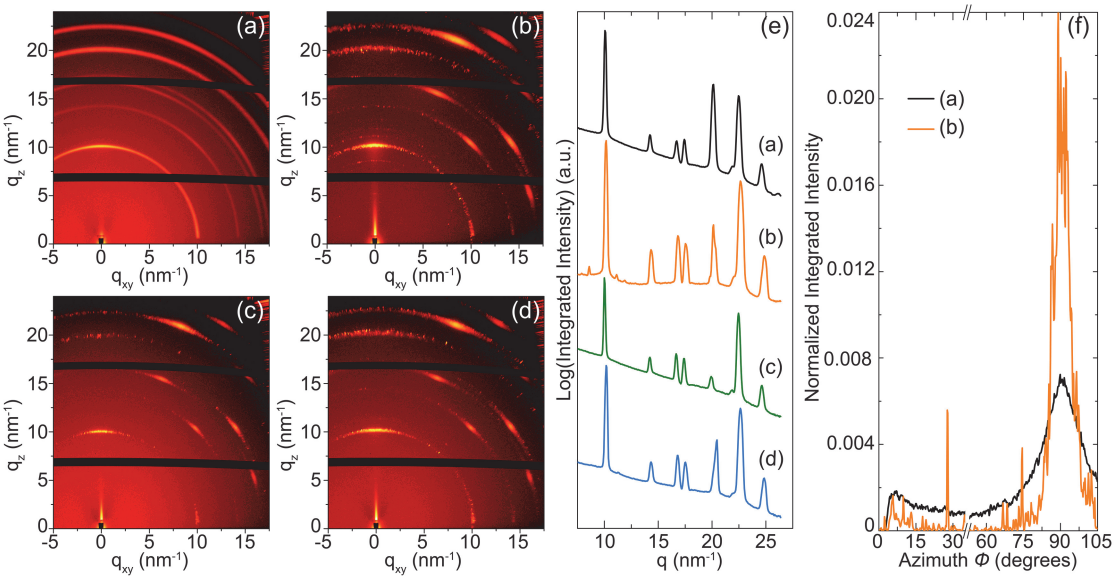

Figure 3.1. GIWAXS profiles of $CH_3NH_3PbI_{3-x}Cl_x$ perovskite films (a) TTD annealed at 100 °C for 45 min on NP-Al_2O_3; flash annealed at 130 °C for 5 min on (b) NP-Al_2O_3, (c) BCP-Al_2O_3, and (d) planar silicon substrates. (e) Azimuthally and (f) radially integrated intensity plots from the corresponding GIWAXS patterns (a)-(d).

To ensure complete phase transformation of the precursors into the perovskite structure, we applied the "time-temperature-dependent" (TTD) annealing treatment holding the NP-Al_2O_3 perovskite sample at 100 °C for 45 min. The corresponding GIWAXS profile in Figure 3.1a displays scattering rings for all seven reflections

along q, indicating the NP-Al_2O_3 perovskite film is polycrystalline. Similar polycrystalline scattering patterns were reported for the same thermal treatment of BCP-Al_2O_3 perovskite samples and perovskite films on planar substrates.[29] Interestingly when we applied a "flash" annealing by rapidly increasing the temperature to 130 °C for 5 min after the ramp to 100 °C (see Figure S3.1), GIWAXS results for all perovskite samples (Figure 3.1b-d) exhibited "spotty" patterns, signifying the formation of highly textured perovskite crystal domains. The azimuthally integrated scattering intensity plots versus scattering vector q (Figure 3.1e) for the different GIWAXS patterns are consistent with the $CH_3NH_3PbI_{3-x}Cl_x$ crystallographic pattern.[29,30] The azimuthal scattering intensity distribution of the peak at $q = 10$ nm^{-1} suggests an orientation in the in-plane direction relative to the substrate. To illustrate the degree of orientation of the perovskite crystal domains in the in-plane direction, we radially integrated over the peak at $q = 10$ nm^{-1} of the two NP-Al_2O_3 perovskite samples (Figure 3.1a,b) and plotted the results against the azimuth angle ϕ (Figure 3.1f). The comparison shows that after the ramp annealing to 100 °C there already is a preferential in-plane orientation, which gets significantly more pronounced after the flash annealing.

Scanning electron microscopy (SEM) images in Figure 3.2 reveal distinctly different perovskite crystal domain sizes depending on the annealing procedure. The TTD annealed perovskite samples at 100 °C for 45 min on NP-Al_2O_3 (Figure 3.2a), BCP-Al_2O_3 (Figure 3.2e) and silicon substrates (Figure 3.2i) display a broad distribution of crystal domain sizes from about 100 to 1000 nm. This is consistent with the polycrystalline pattern we observed for the NP-Al_2O_3 perovskite sample in the GIWAXS measurement (Figure 3.1a). From the cross-sectional SEM images (Figure 3.2b,f,j), the polycrystalline domains form a relatively rough surface. When the perovskite samples were flash annealed to 130 °C, a very different film morphology

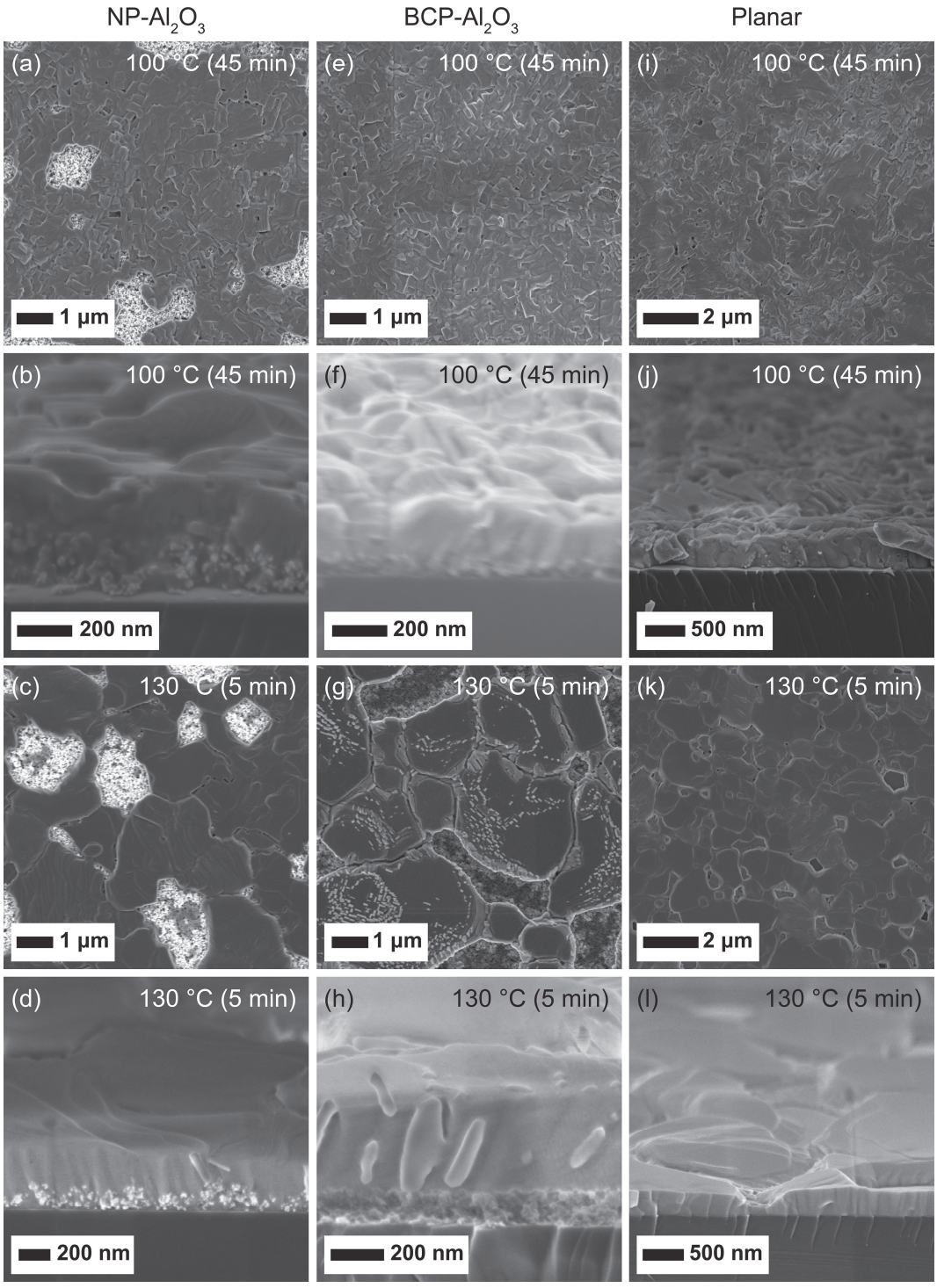

Figure 3.2. Plan view and cross-sectional SEM micrographs of perovskite films on (a-d) NP-Al_2O_3, (e-h) BCP-Al_2O_3 and (i-l) planar silicon substrates prepared by the respective thermal annealing procedures as indicated.

consisting of micron-sized crystal domains (Figure 3.2c,g,k and respective cross-sections in Figure 3.2d,h,l) emerged. This is consistent with the highly oriented spotty patterns obtained from GIWAXS (Figure 3.1b-d). All the resulting perovskite films have a maximum thickness of approximately 400 nm after thermal annealing.

Perovskite-Based Hybrid Solar Cell Performances. We fabricated $CH_3NH_3PbI_{3-x}Cl_x$ meso-superstructured (MSSC) and planar heterojunction perovskite solar cells on the mesoporous NP-Al_2O_3 superstructure and on a planar TiO_2 compact layer/FTO glass, annealed by TTD (100 °C for 45 min) and flash (130 °C for 5 min) procedures after the slow temperature ramp. In the following, the thermally annealed samples are designated by X-Y, where X represents substrate (NP or planar) and Y is the highest temperature at which the perovskite was annealed. Figure 3.3 displays the schematic (Figure 3.3a) and current density/voltage plots (Figure 3.3b,c) of the respective best performing perovskite solar cells along with a table inset of their performance parameters.

In Table 3.1 we summarize the average device performance parameters: short-circuit current (J_{SC}), open-circuit voltage (V_{OC}), fill factor (FF) and power conversion efficiency (PCE) of the TTD 100 °C and flash 130 °C annealed samples. We note that in this study we employed 100 nm thick mesoporous scaffolds, which are thinner than for the best MSSCs thus far which employed ~400 nm thick mesoporous Al_2O_3. [17,20,31,32] Here, a perovskite capping layer was formed on the ~100 nm NP-Al_2O_3 thin films (see Figure 3.2b,d). All NP-Al_2O_3 perovskite MSSCs exhibited similar average values for J_{SC} ~18 mA/cm^2 and V_{OC} around 0.9 V. However, the average FF (0.53 to 0.44) and PCE (8.4% to 6.9%) decreased for the NP-130 MSSCs compared to NP-100 devices. The best performing NP-Al_2O_3 perovskite MSSC was annealed at 100 °C for 45 min

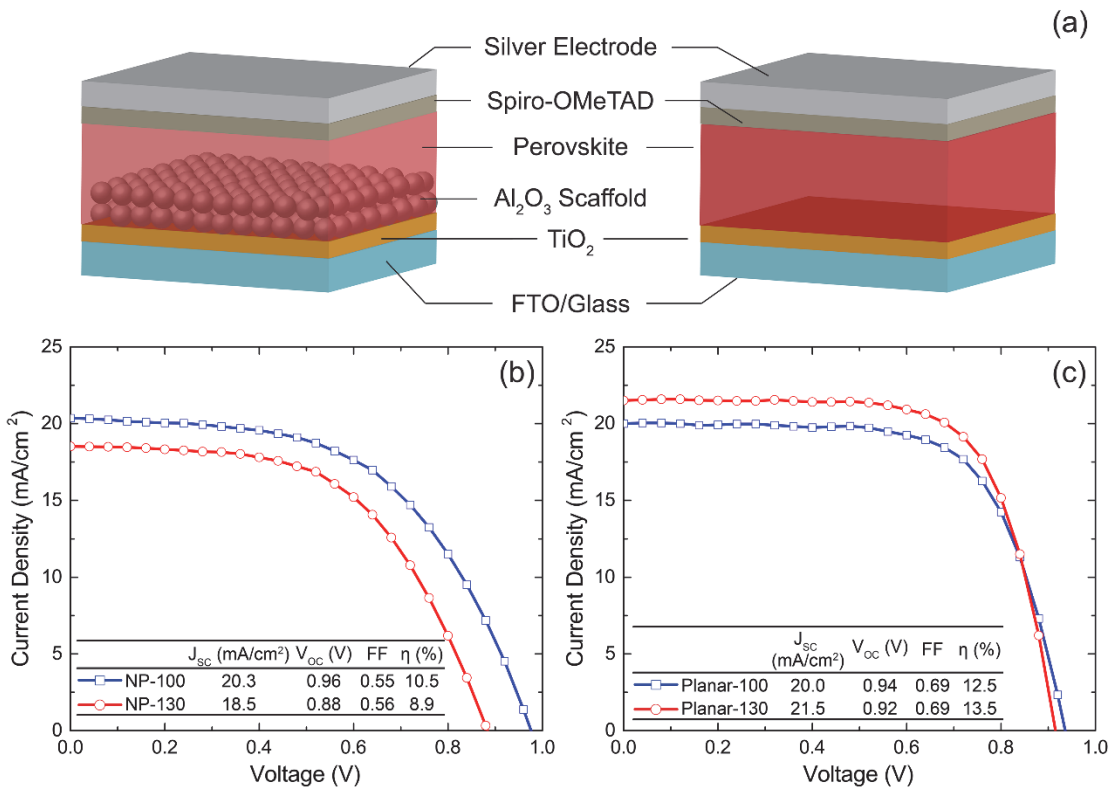

Figure 3.3. (a) Schematic of meso-superstructured and planar heterojunction perovskite solar cells. Current density/voltage curves of differently annealed (b) NP-Al_2O_3 MSSC and (c) planar heterojunction perovskite solar cells measured under stimulated AM1.5 sunlight of 100 mW/cm^2 irradiation.

Table 3.1. Meso-superstructured (≥14 devices) and planar heterojunction (22 devices) perovskite solar cell performance parameters measured under 100 mW/cm^2 stimulated AM1.5 sunlight irradiation.

	short-circuit current density (ma/cm^2)	**open-circuit voltage (v)**	**fill factor**	**power conversion efficiency (%)**
NP-100	17.7 ± 2.9	0.92 ± 0.04	0.53 ± 0.05	8.4 ± 1.8
NP-130	17.5 ± 1.7	0.91 ± 0.07	0.44 ± 0.09	6.9 ± 1.6
Planar-100	17.9 ± 2.2	0.92 ± 0.03	0.61 ± 0.05	9.9 ± 1.5
Planar-130	19.0 ± 1.6	0.91 ± 0.02	0.63 ± 0.04	10.7 ± 1.3

achieving a PCE of 10.5% (Figure 3.3b). However, when the Al_2O_3 perovskite MSSC was flash annealed at 130 °C for 5 min, the PCE decreased to 8.9% due to lower V_{OC} and J_{SC} values (Figure 3.3b).

We attribute the lower FFs and PCEs for the NP-130 MSSC devices to the reduced perovskite surface coverage.[17,24] The higher 130 °C annealing temperature (albeit shorter annealing duration) led to larger pores in the perovskite capping layer and exposed the mesoporous Al_2O_3 scaffold layer (see Figure 3.2a,c). From plan view SEM images, we estimated the perovskite capping layer coverage reduced by 5% (from ~82% to ~77%) for the NP-130 perovskite films compared to TTD annealed samples (Figure 3.4). Moreover, the cross-sectional SEM images in Figure S3.2 indicate that the NP-Al_2O_3 regions with no perovskite capping layer are only partially filled and may permit direct contact of the hole-transporter with the TiO_2 compact layer, resulting in lower shunt resistance.[17,24]

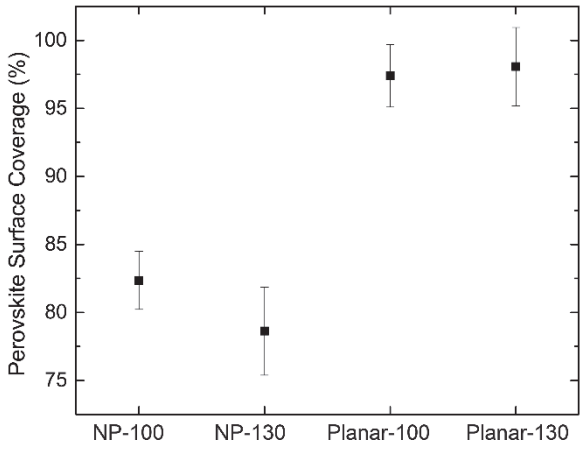

Figure 3.4. Perovskite surface coverage on NP-Al_2O_3 and planar surfaces prepared by TTD and flash thermal annealing.

We applied identical thermal annealing procedures to planar heterojunction perovskite solar cells formed directly on TiO_2 compact layer with the average device parameters summarized in Table 3.1. The first clear observation is that they performed much better than the equivalent MSSCs of the same study. Comparing between the different annealing protocols, while the average V_{OC} (~0.9 V) and FFs (~0.6) are indistinguishable for differently annealed planar perovskite devices, the average J_{SC} and PCE of planar-130 devices improved from 17.9 to 19.0 mA/cm^2 and 9.9% to 10.7%, respectively, as compared to the planar-100 devices. The current density/voltage curves of the best performing devices are plotted in Figure 3.3c. In particular, the FF of 0.69 for our best single-step spin coating processed, thermally annealed planar heterojunction perovskite solar cells are in good agreement or even exceeding other champion perovskite photovoltaic devices prepared by sequential solution processing,[20,28] vapor deposition,[16,35] and combined solution-vapor-processing.[27]

We can attribute the high FF (~0.6) and PCE (>10%) for the planar heterojunction perovskite solar cells to the formation of a uniform perovskite absorber layer with a reduced number of pores by a controlled ramp from ambient temperature to 100 °C (see Figure 3.2i,k).[16,24–27,29] Indeed, as we show in Figure 3.4, we observe perovskite surface coverage greater than 95% for both planar perovskite films thermally annealed at 100 °C for 45 min and 130 °C for 5 min. The higher J_{SC} and PCE values of the planar-130 with respect to planar-100 perovskite solar cells are likely due to the formation of more uniform, micron-sized textured perovskite domains as observed *via* GIWAXS (Figure 3.1d) and SEM (Figure 3.2k). Figure S3.3 displays highly similar planar perovskite film morphologies on TiO_2 compact layer/FTO glass substrates synthesized by TTD and flash thermal annealing. UV-vis absorbance plots for planar-100 and planar-130 perovskite films in Figure S3.4 display similar light absorption spectra for both planar-

100 and planar-130 perovskite films. Non-radiative recombination of charge carriers is likely to occur at the grain boundaries, which we can reason from faster photoluminescence (PL) decay for perovskite films with smaller crystalline domains.[17,23,40] Indeed, we observe longer PL lifetimes and higher steady-state PL intensity for the flash annealed planar-130 films (see Figure S3.5). However, we do note that there could be additional influences of the flash annealing beyond changes to the domain size, such as changes to the stoichiometry of the perovskite material, which could also be influencing the PL lifetime. Whether the charge carrier mobility is strongly influenced by domain size is yet to be observed. In addition, the precise nature of the electronic contact at the perovskite/TiO_2 and perovskite/spiro-OMeTAD interfaces may be strongly influenced by the crystallinity of the perovskite at these contacts.[27] All considered, it appears that the larger domain sizes are advantageous for more optimum photovoltaic operation, as would be expected for a conventional thin film semiconductor. The proviso is that the macroscopic film morphology also has to be as uniform as possible, absent from pinholes.

Conclusion

In summary, we have demonstrated film morphology control in $CH_3NH_3PbI_{3-x}Cl_x$ perovskite thin films by tuning the thermal annealing conditions after a slow ramp. Using grazing incidence wide-angle X-ray scattering and scanning electron microscopy, we found that a short rapid annealing at 130 °C promoted the growth of highly uniform micron-sized textured perovskite domains, while a longer dwell at 100 °C resulted in 100-1000 nm polycrystalline perovskite domains. The rapid 130 °C and longer 100 °C thermal annealing resulted in very different perovskite solar cell performances with the meso-superstructured and planar heterojunction device architectures. In general, the 100

°C annealed MSSC devices performed better than 130 °C annealed samples attributed to the higher perovskite surface coverage. The planar perovskites devices outperformed the MSSC mesostructured counterparts mainly due to higher fill factor and short-circuit currents, obtained from >95% perovskite surface coverage. Moreover, the 130 °C flash thermal annealing resulted in planar heterojunction solar cells with highly textured perovskite domains and average power conversion efficiency improvement from 9.9 to 10.7%, as compared to the 100 °C annealed planar devices. We postulate that improvement arises from reduced recombination losses at the grain boundaries as inferred from PL decay measurements. The best performing planar heterojunction perovskite solar cell achieved a high power conversion efficiency of 13.5%. This study highlights the importance of simultaneously controlling both the macroscopic morphology and the crystalline domain size.

Acknowledgement

This work was financially supported by the National Science Foundation (NSF) through the Materials World Network grant between the US (DMR-1008125) and the UK (Engineering and Physical Sciences Research Council, EPSRC). K.W.T. gratefully acknowledges the Singapore Energy Innovation Programme Office for a National Research Foundation graduate fellowship. This work made use of the research facilities of the Cornell Center for Materials Research (CCMR) with support from the NSF Materials Research Science and Engineering Centers (MRSEC) program (DMR-1120296), Cornell High Energy Synchrotron Source (CHESS) which is supported by the NSF and the NIH/National Institute of General Medical Sciences under NSF award DMR-0936384, and the KAUST-Cornell Center for Energy and Sustainability supported by Award No. KUS-C1-018-02, made by King Abdullah University of

Science and Technology (KAUST). The authors acknowledge A. Abate and S. Stranks of University of Oxford and D. M. Smilgies, M. Koker and R. Li of Cornell University for helpful discussion and kind experimental assistance.

REFERENCES

(1) Kagan, C. R.; Mitzi, D. B.; Dimitrakopoulos, C. D. Organic-Inorganic Hybrid Materials as Semiconducting Channels in Thin-Film Field-Effect Transistors. *Science* **1999**, *286*, 945–947.

(2) Mitzi, D. B.; Chondroudis, K.; Kagan, C. R. Organic-Inorganic Electronics. *IBM J. Res. Dev.* **2001**, *45*, 29–45.

(3) Graetzel, M.; Janssen, R. A. J.; Mitzi, D. B.; Sargent, E. H. Materials Interface Engineering for Solution-Processed Photovoltaics. *Nature* **2012**, *488*, 304–312.

(4) Nayak, P. K.; Cahen, D. Updated Assessment of Possibilities and Limits for Solar Cells. *Adv. Mater.* **2014**, *26*, 1622–1628.

(5) Lotsch, B. V. New Light on an Old Story: Perovskites Go Solar. *Angew. Chem. Int. Ed.* **2014**, *53*, 635–637.

(6) Service, R. F. Turning Up the Light. *Science* **2013**, *342*, 794–797.

(7) Snaith, H. J. Perovskites: The Emergence of a New Era for Low-Cost, High-Efficiency Solar Cells. *J. Phys. Chem. Lett.* **2013**, 3623–3630.

(8) Park, N.-G. Organometal Perovskite Light Absorbers Toward a 20% Efficiency Low-Cost Solid-State Mesoscopic Solar Cell. *J. Phys. Chem. Lett.* **2013**, *4*, 2423–2429.

(9) Kim, H.-S.; Im, S. H.; Park, N.-G. Organolead Halide Perovskite: New Horizons in Solar Cell Research. *J. Phys. Chem. C* **2014**, *118*, 5615–5625.

(10) Poglitsch, A.; Weber, D. Dynamic Disorder in Methylammoniumtrihalogenoplumbates (II) Observed by Millimeter-wave Spectroscopy. *J. Chem. Phys.* **1987**, *87*, 6373–6378.

(11) Kojima, A.; Teshima, K.; Shirai, Y.; Miyasaka, T. Organometal Halide Perovskites as Visible-Light Sensitizers for Photovoltaic Cells. *J. Am. Chem. Soc.* **2009**, *131*, 6050–6051.

(12) Im, J.-H.; Lee, C.-R.; Lee, J.-W.; Park, S.-W.; Park, N.-G. 6.5% Efficient Perovskite Quantum-Dot-Sensitized Solar Cell. *Nanoscale* **2011**, *3*, 4088–4093.

(13) Etgar, L.; Gao, P.; Xue, Z.; Peng, Q.; Chandiran, A. K.; Liu, B.; Nazeeruddin, M. K.; Grätzel, M. Mesoscopic $CH_3NH_3PbI_3/TiO_2$ Heterojunction Solar Cells. *J. Am. Chem. Soc.* **2012**, *134*, 17396–17399.

(14) Kim, H.-S.; Lee, C.-R.; Im, J.-H.; Lee, K.-B.; Moehl, T.; Marchioro, A.; Moon, S.-J.; Humphry-Baker, R.; Yum, J.-H.; Moser, J. E.; et al. Lead Iodide Perovskite Sensitized All-Solid-State Submicron Thin Film Mesoscopic Solar Cell with Efficiency Exceeding 9%. *Sci. Rep.* **2012**, *2*, 591.

(15) Lee, M. M.; Teuscher, J.; Miyasaka, T.; Murakami, T. N.; Snaith, H. J. Efficient Hybrid Solar Cells Based on Meso-Superstructured Organometal Halide Perovskites. *Science* **2012**, *338*, 643–647.

(16) Liu, M.; Johnston, M. B.; Snaith, H. J. Efficient Planar Heterojunction Perovskite Solar Cells by Vapour Deposition. *Nature* **2013**, *501*, 395–398.

(17) Ball, J. M.; Lee, M. M.; Hey, A.; Snaith, H. J. Low-Temperature Processed Meso-Superstructured to Thin-Film Perovskite Solar Cells. *Energy Environ. Sci.* **2013**, *6*, 1739–1743.

(18) Noh, J. H.; Im, S. H.; Heo, J. H.; Mandal, T. N.; Seok, S. I. Chemical Management for Colorful, Efficient, and Stable Inorganic–Organic Hybrid Nanostructured Solar Cells. *Nano Lett.* **2013**, *13*, 1764–1769.

(19) Crossland, E. J. W.; Noel, N.; Sivaram, V.; Leijtens, T.; Alexander-Webber, J. A.; Snaith, H. J. Mesoporous TiO_2 Single Crystals Delivering Enhanced Mobility and Optoelectronic Device Performance. *Nature* **2013**, *495*, 215–219.

(20) Burschka, J.; Pellet, N.; Moon, S.-J.; Humphry-Baker, R.; Gao, P.; Nazeeruddin, M. K.; Grätzel, M. Sequential Deposition as a Route to High-Performance Perovskite-Sensitized Solar Cells. *Nature* **2013**, *499*, 316–319.

(21) Heo, J. H.; Im, S. H.; Noh, J. H.; Mandal, T. N.; Lim, C.-S.; Chang, J. A.; Lee, Y. H.; Kim, H.; Sarkar, A.; Nazeeruddin, M. K.; et al. Efficient Inorganic-Organic Hybrid Heterojunction Solar Cells Containing Perovskite Compound and Polymeric Hole Conductors. *Nat. Photonics* **2013**, *7*, 486–491.

(22) Zhang, W.; Saliba, M.; Stranks, S. D.; Sun, Y.; Shi, X.; Wiesner, U.; Snaith, H. J. Enhancement of Perovskite-Based Solar Cells Employing Core–Shell Metal Nanoparticles. *Nano Lett.* **2013**, *13*, 4505–4510.

(23) Stranks, S. D.; Eperon, G. E.; Grancini, G.; Menelaou, C.; Alcocer, M. J. P.; Leijtens, T.; Herz, L. M.; Petrozza, A.; Snaith, H. J. Electron-Hole Diffusion Lengths Exceeding 1 Micrometer in an Organometal Trihalide Perovskite Absorber. *Science* **2013**, *342*, 341–344.

(24) Eperon, G. E.; Burlakov, V. M.; Docampo, P.; Goriely, A.; Snaith, H. J. Morphological Control for High Performance, Solution-Processed Planar Heterojunction Perovskite Solar Cells. *Adv. Funct. Mater.* **2014**, *24*, 151–157.

(25) Conings, B.; Baeten, L.; De Dobbelaere, C.; D'Haen, J.; Manca, J.; Boyen, H.-G. Perovskite-Based Hybrid Solar Cells Exceeding 10% Efficiency with High Reproducibility Using a Thin Film Sandwich Approach. *Adv. Mater.* **2014**, *26*, 2041–2046.

(26) Jeng, J.-Y.; Chiang, Y.-F.; Lee, M.-H.; Peng, S.-R.; Guo, T.-F.; Chen, P.; Wen, T.-C. $CH_3NH_3PbI_3$ Perovskite/Fullerene Planar-Heterojunction Hybrid Solar Cells. *Adv. Mater.* **2013**, *25*, 3727–3732.

(27) Chen, Q.; Zhou, H.; Hong, Z.; Luo, S.; Duan, H.-S.; Wang, H.-H.; Liu, Y.; Li, G.; Yang, Y. Planar Heterojunction Perovskite Solar Cells via Vapor-Assisted Solution Process. *J. Am. Chem. Soc.* **2014**, *136*, 622–625.

(28) Liu, D.; Kelly, T. L. Perovskite Solar Cells with a Planar Heterojunction Structure Prepared Using Room-Temperature Solution Processing Techniques. *Nat. Photonics* **2014**, *8*, 133–138.

(29) Tan, K. W.; Moore, D. T.; Saliba, M.; Sai, H.; Estroff, L. A.; Hanrath, T.; Snaith, H. J.; Wiesner, U. Thermally Induced Structural Evolution and Performance of Mesoporous Block Copolymer-Directed Alumina Perovskite Solar Cells. *ACS Nano* **2014**, *8*, 4730–4739..

(30) Colella, S.; Mosconi, E.; Fedeli, P.; Listorti, A.; Gazza, F.; Orlandi, F.; Ferro, P.; Besagni, T.; Rizzo, A.; Calestani, G.; et al. $MAPbI_{3-x}Cl_x$ Mixed Halide Perovskite for Hybrid Solar Cells: The Role of Chloride as Dopant on the Transport and Structural Properties. *Chem. Mater.* **2013**, *25*, 4613–4618.

(31) Wang, J. T.-W.; Ball, J. M.; Barea, E. M.; Abate, A.; Alexander-Webber, J. A.; Huang, J.; Saliba, M.; Mora-Sero, I.; Bisquert, J.; Snaith, H. J.; et al. Low-Temperature Processed Electron Collection Layers of Graphene/TiO_2 Nanocomposites in Thin Film Perovskite Solar Cells. *Nano Lett.* **2014**, *14*, 724–730.

(32) Wojciechowski, K.; Saliba, M.; Leijtens, T.; Abate, A.; Snaith, H. J. Sub-150 °C Processed Meso-Superstructured Perovskite Solar Cells with Enhanced Efficiency. *Energy Environ. Sci.* **2014**, *7*, 1142–1147.

(33) You, J.; Hong, Z.; Yang, Y. (Michael); Chen, Q.; Cai, M.; Song, T.-B.; Chen, C.-C.; Lu, S.; Liu, Y.; Zhou, H.; et al. Low-Temperature Solution-Processed Perovskite Solar Cells with High Efficiency and Flexibility. *ACS Nano* **2014**, *8*, 1674–1680.

(34) Docampo, P.; Ball, J. M.; Darwich, M.; Eperon, G. E.; Snaith, H. J. Efficient Organometal Trihalide Perovskite Planar-Heterojunction Solar Cells on Flexible Polymer Substrates. *Nat. Commun.* **2013**, *4*, 2761.

(35) Malinkiewicz, O.; Yella, A.; Lee, Y. H.; Espallargas, G. M.; Graetzel, M.; Nazeeruddin, M. K.; Bolink, H. J. Perovskite Solar Cells Employing Organic Charge-Transport Layers. *Nat. Photonics* **2014**, *8*, 128–132.

(36) O'Regan, B.; Grätzel, M. A Low-Cost, High-Efficiency Solar Cell Based on Dye-Sensitized Colloidal TiO_2 Films. *Nature* **1991**, *353*, 737–740.

(37) Liang, K.; Mitzi, D. B.; Prikas, M. T. Synthesis and Characterization of Organic−Inorganic Perovskite Thin Films Prepared Using a Versatile Two-Step Dipping Technique. *Chem. Mater.* **1998**, *10*, 403–411.

(38) Xing, G.; Mathews, N.; Sun, S.; Lim, S. S.; Lam, Y. M.; Grätzel, M.; Mhaisalkar, S.; Sum, T. C. Long-Range Balanced Electron- and Hole-Transport Lengths in Organic-Inorganic $CH_3NH_3PbI_3$. *Science* **2013**, *342*, 344–347.

(39) Hammersley, A. P.; Svensson, S. O.; Hanfland, M.; Fitch, A. N.; Hausermann, D. Two-Dimensional Detector Software: From Real Detector to Idealised Image or Two-Theta Scan. *High Press. Res.* **1996**, *14*, 235–248.

(40) Wehrenfennig, C.; Eperon, G. E.; Johnston, M. B.; Snaith, H. J.; Herz, L. M. High Charge Carrier Mobilities and Lifetimes in Organolead Trihalide Perovskites. *Adv. Mater.* **2014**, *26*, 1584–1589.

APPENDIX B

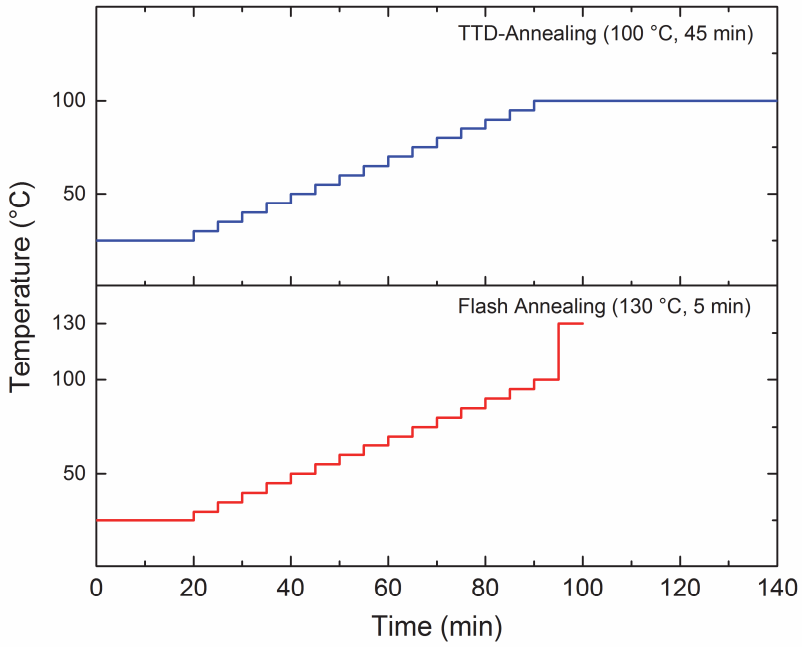

Figure S3.1. Representative plot of TTD and flash thermal annealing protocols.

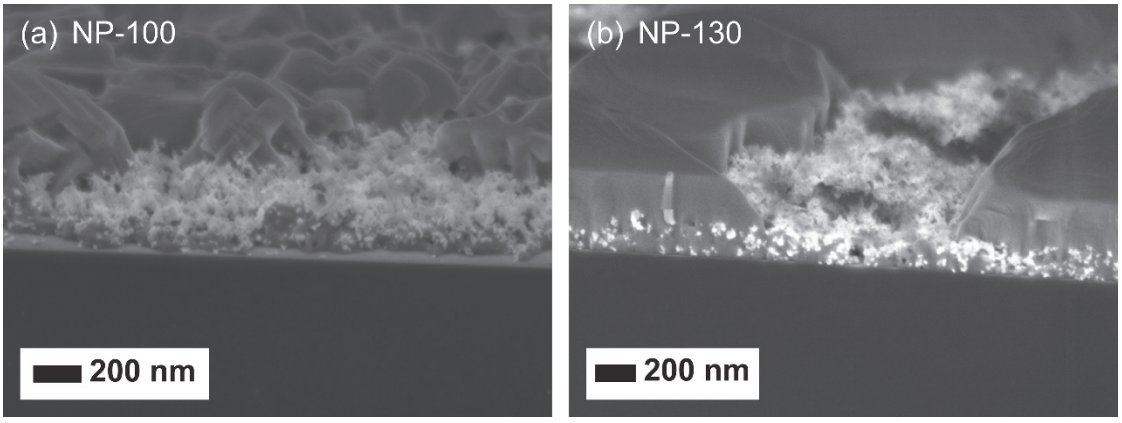

Figure S3.2. Cross-sectional SEM micrographs of perovskite capping layer-free regions on (a) NP-100 and (b) NP-130 mesosuperstructured perovskite thin films.

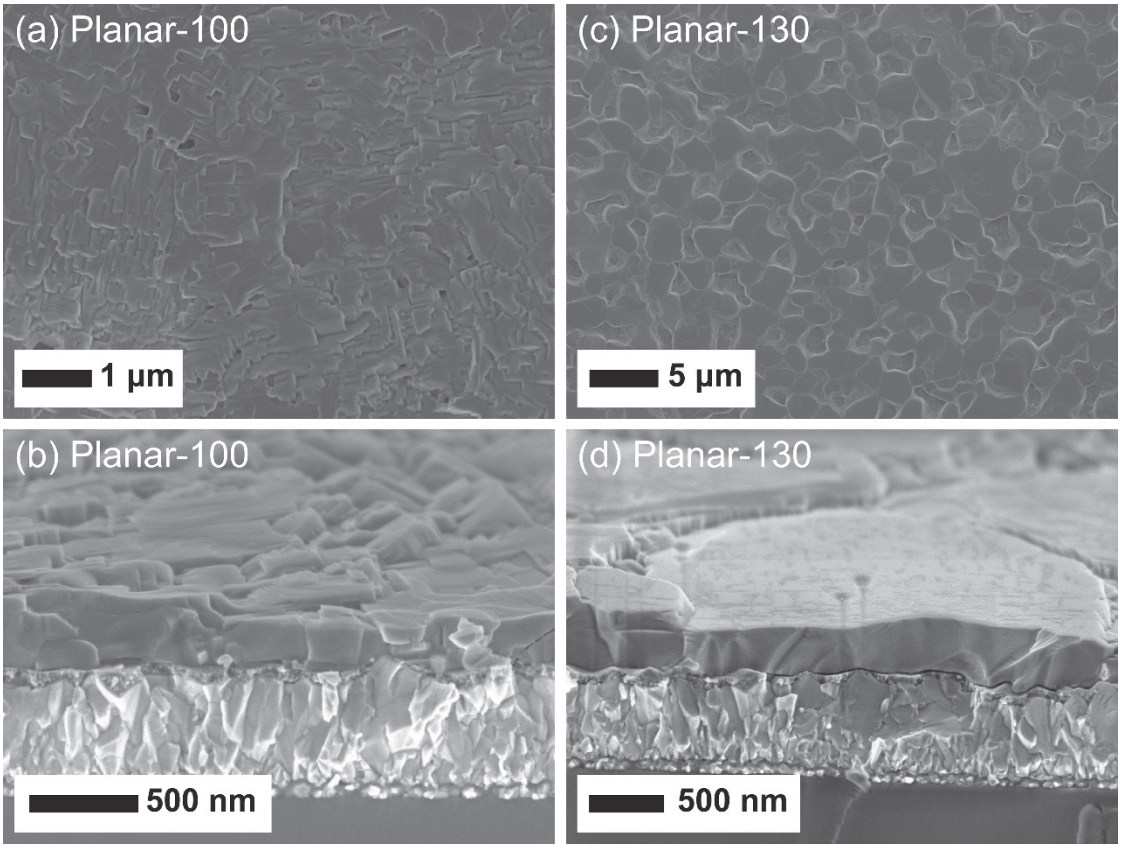

Figure S3.3. Plan view and cross-sectional SEM micrographs of (a, b) planar-100, and (c, d) planar-130 perovskite films on TiO_2 compact layer/FTO glass substrates.

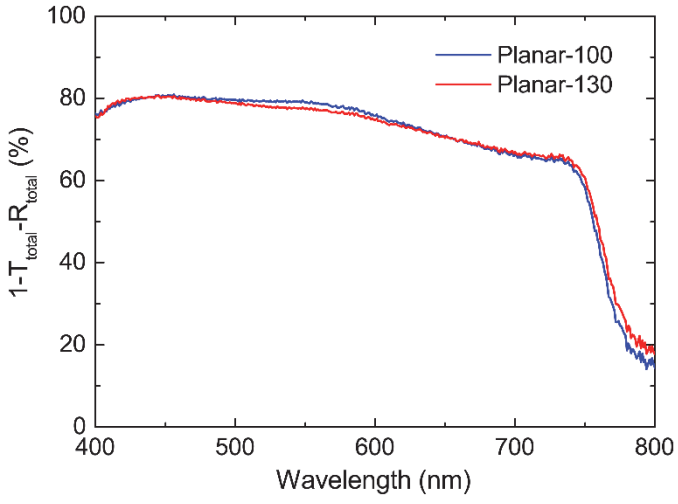

Figure S3.4. UV-vis absorbance plot for the planar-100 (black) and planar-130 (red) perovskite films measured with an integrating sphere accessory.

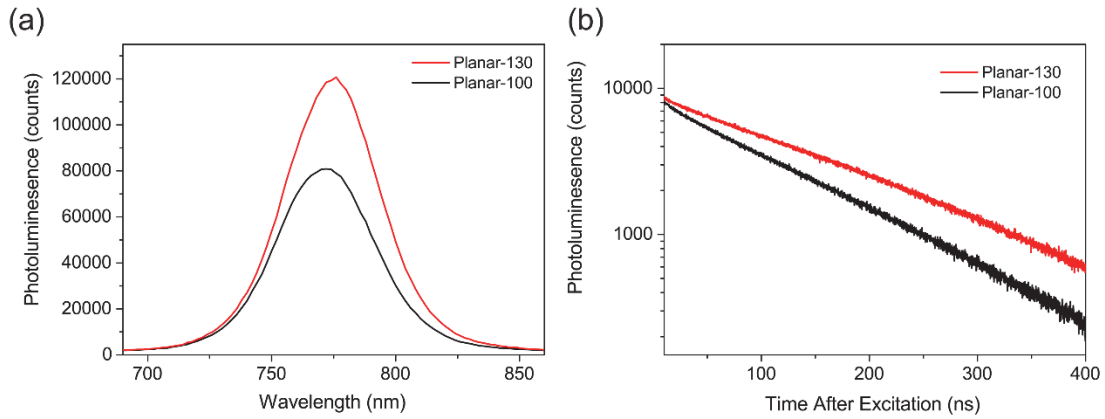

Figure S3.5. (a) Steady-state and (b) time-resolved photoluminescence measurements for planar-130 (red) and planar-100 (black) perovskite films on glass substrates.

CHAPTER 4

COLLOIDAL SELF-ASSEMBLY-DIRECTED LASER-INDUCED NON-CLOSE-PACKED CRYSTALLINE SILICON NANOSTRUCTURES

Abstract

This report describes an ultrafast, large area, and highly flexible method to construct complex two- and three-dimensional silicon nanostructures with deterministic non-close-packed symmetry. Pulsed excimer laser irradiation is used to induce a transient melt transformation of amorphous silicon filled in a colloidal self-assembly-directed inverse opal template, resulting in a nanostructured crystalline phase. The pattern transfer yields are high and long-range order is maintained. This technique represents a potential route to obtain silicon nanostructures of various symmetries and associated unique properties for advanced applications such as energy storage and generation.

Reproduced with permission from Tan, K. W., Saba, S. A., Arora, H., Thompson, M. O. & Wiesner, U. Colloidal self-assembly-directed laser-induced non-close-packed crystalline silicon nanostructures. *ACS Nano* **5**, 7960–7966 (2011). Copyright 2011 American Chemical Society.

Introduction

Silicon-based nanomaterials have great potential for a wide variety of applications due to silicon's abundance and implicit compatibility with current semiconductor processing technologies. Structures based on silicon have been widely adapted as photonic crystals,[1-6] solar cells,[7-12] sensors[13,14] and thermoelectric devices.[15-20] In particular, non-close-packed silicon nanostructures are highly desirable for their wide photonic bandgap and may be beneficial for other surface-enhanced properties.[5,6,21-28]

Non-close-packed silicon nanostructures based on sacrificial inverse opal templates have been demonstrated, but only in the amorphous phase (a-Si).[5,6] While a myriad of methods to obtain crystalline silicon (c-Si) nanostructures exist, including, for example, slow heating of a-Si[2,3,10,29] and magnesium reduction of silica[4,30-32] (SiO_2) into c-Si at 600–675 °C, these thermal crystallization techniques in the solid phase require several hours at elevated temperatures in an inert environment. The stoichiometric yields of c-Si from magnesium reduction of SiO_2 are also relatively low (34.9 vol %).[30] An alternative approach is using pulsed lasers to induce an extremely short transient melt-crystallization conversion of a-Si precursors into c-Si enabling thermal processing on many different substrates such as glass and polyimide.[33,34] Pulsed laser irradiation has been coupled to nanoimprinting,[35,36] nanosphere lithography[37-39] and block copolymer-directed templating[40] to obtain Si nano-gratings, pillars and porous thin films. To the best of our knowledge, however, it has not been applied to rapid transformations of colloidal crystal templates into non-close-packed c-Si structures.

In this work, we demonstrate a facile, rapid and versatile method to fabricate non-close-packed c-Si colloidal nanostructures using a laser-induced transient melt process. We employed a hexagonally arranged close-packed (hcp) sacrificial colloidal crystal

template to define and construct two-dimensional (2D) hexagonal-non-close-packed (hncp) c-Si arrays and 3D ordered macroporous hncp c-Si nanostructures. The crystallinity and non-close-packed symmetry of such highly ordered silicon 2D nanoarrays and 3D interconnecting pore network nanostructures are known to enhance electrical conductivity, photonic, and other surface properties significantly and could improve device performance, for example, in optoelectronics, photovoltaics and thermoelectrics.[2,3,5,6,29]

Results and Discussion

Scheme 4.1 illustrates the experimental processes. Polystyrene (PS) colloids (0.5 wt %) with diameters of either 530 nm or 350 nm were mixed with deionized water and hydrolyzed tetraethylorthosilicate (TEOS) solution.[32] A monolayer colloidal crystal of PS spheres surrounded by TEOS-derived SiO_2 was formed using the flow-controlled vertical deposition (FCVD) method.[41-43] The resulting latex beads were slowly calcined in air at 500 °C, leaving behind a highly ordered hcp SiO_2 inverse monolayer colloidal crystal. This inorganic template was subsequently filled with ~100 nm thick a-Si overlayer by sputter deposition or plasma-enhanced chemical vapor deposition (PECVD) and irradiated with a 40 ns full-width-half-maximum pulsed XeCl excimer laser (308 nm wavelength) in air to induce the melt conversion of a-Si to the crystalline phase. The entire duration of laser-induced melt and solidification was approximately 20–100 ns. Finally, the SiO_2 template was removed in concentrated hydrofluoric (HF) acid solution leaving the hncp Si nanostructured array seen in Scheme 1c.

Scanning electron microscopy (SEM) images in Figure 4.1 show the various stages of the process. A hcp SiO_2 inverse template (530 nm pore size, Figure 4.1b)

obtained from PS monolayer colloidal crystal surrounded by a SiO_2 matrix (Figure 4.1a) was filled with ~100 nm of a-Si by top-down sputter deposition (Figure 4.1c). Melt of the a-Si overlayer was induced by a single 308 nm laser pulse at the single-crystal Si melt threshold of 600 mJ/cm^2 and rapidly solidified after 30 ns.[40] The SiO_2 template is transparent at this wavelength, and the laser irradiation energy is absorbed solely by Si. c-Si is formed when a-Si melts and solidifies as confirmed by characteristic time resolved reflectance measurements (Figure S4.2).[35,40,44,45] From Figure 4.1d the long-range hexagonal order of the resulting ncp c-Si nanostructured arrays was largely preserved after removing the template in an HF acid solution.

We postulate the c-Si nanostructure assumed the observed teardrop-shape due to a combination of templated dewetting[46,47] and the rapid solidification process. Upon irradiation, a-Si in the SiO_2 pore melts and diffuses radially to the center driven by template dewetting. The molten Si would attempt to form a hemispherical shape to minimize the surface tension.[48] However, during this extremely short melt duration, the liquid Si (density of 2.53 g/cm^3) expands upon solidification (density of 2.30 g/cm^3) and perturbs the adjacent liquid Si creating capillary waves.[34,49] These molten capillary waves are confined between coalescing solid grain boundaries from all directions and froze into protruding ridge and hillock features with a teardrop-shape as a result of heterogeneous nucleation and growth mechanism.[34,49] We also observe interconnected nanostructures (*e.g.*, see lower left corner in Figure 4.1d) that may be attributed to insufficient driving force and the ultrashort time scale for the liquid Si to dewet completely into the pores. From SEM data, the c-Si nanostructures are smaller than the pores with an average width and height of around 410 nm and 300 nm, respectively, consistent with other experimental observations.[46]

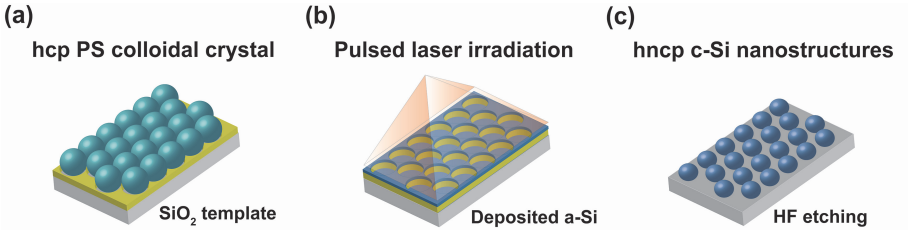

Scheme 4.1. Schematic illustration of hncp c-Si nanostructure generation. (a) The PS monolayer colloidal crystal surrounded by a SiO_2 matrix is grown using a one-step flow-controlled vertical deposition method on Si substrates. (b) PS beads are removed by slow calcination at 500 °C. a-Si is deposited as an overlayer on the hcp SiO_2 inverse colloidal crystal template and irradiated by a pulsed excimer laser. (c) The template is dissolved in HF revealing the 2D hncp c-Si nanostructured arrays on the Si substrate.

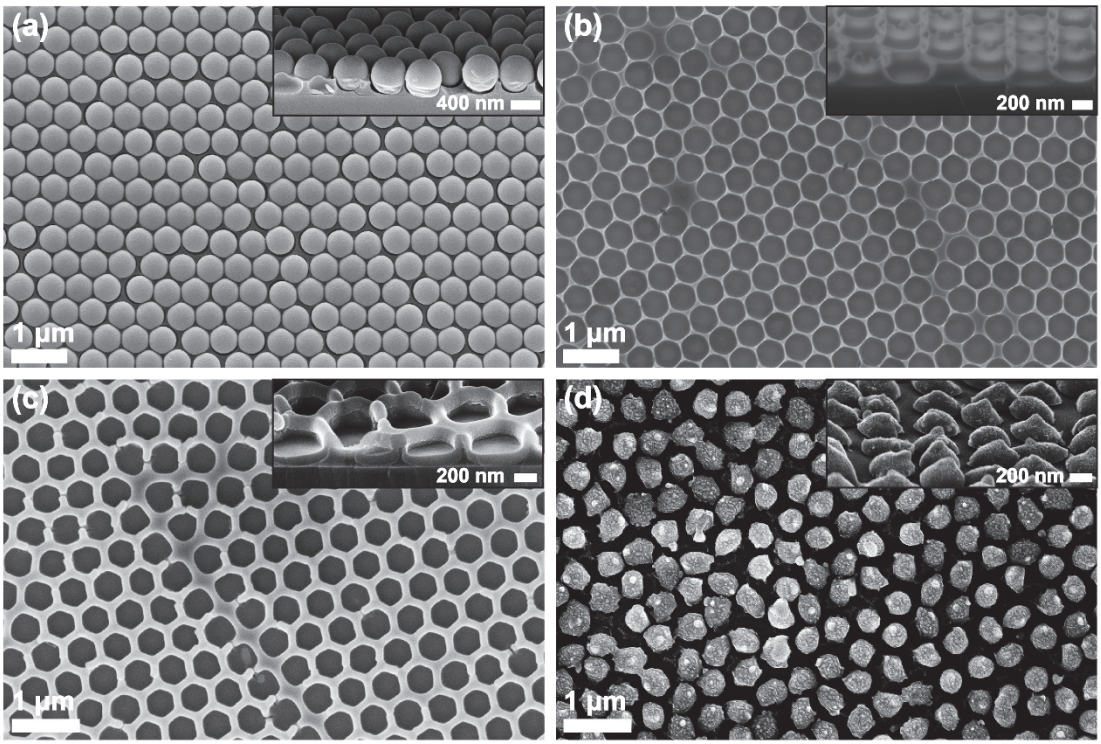

Figure 4.1. Plan view and cross-sectional (insets) SEM micrographs of the sputter-deposited and processed sample. (a) hcp PS monolayer colloidal crystal using 530 nm diameter beads surrounded by the SiO_2 matrix. (b) hcp SiO_2 inverse monolayer colloidal crystal template after calcination. (c) a-Si overlayer back-filled by top-down sputter deposition. (d) hncp c-Si nanostructures after HF etching.

SEM results from a smaller, 350 nm PS colloidal template (Figure 4.2a) are shown in Figure 4.2. A ~100 nm thick a-Si film was deposited into the smaller SiO_2 inverse monolayer colloidal crystal template (Figure 4.2b) using PECVD. Figure 4.2c depicts hydrogenated a-Si deposited conformally within the pores and on the walls of the SiO_2 template. Due to the presence of hydrogen in PECVD a-Si films, microscopic blistering of the surface is observed for films irradiated at high fluences due to the explosive release of the trapped gas upon melting.[34,50,51] Alternatively, the hydrogenated a-Si films were irradiated with 4 sequential laser pulses at 500–700 mJ/cm^2, generating a more controlled and stepwise heating and release of hydrogen. The resulting hncp c-Si nanostructures imaged in Figures 2d with SEM and 3b with atomic force microscopy (AFM) exhibit an average width of around 170 nm and height of 60–70 nm.

Figure 4.3 shows the AFM height profile images and corresponding Voronoi tessellation constructions of both the hcp SiO_2 template and hncp c-Si nanostructured arrays resulting from the laser-induced melting and solidification process. A n-sided polygon represents a SiO_2 template pore or c-Si nanostructure at the center having an equivalent n number of nearest neighbors.[40,52,53] The majority green-colored hexagon (six-fold) spatial areas in the Voronoi diagrams contain a total of 577 six-coordinated template pores (Figure 4.3c) and 571 six-coordinated c-Si nanostructures (Figure 4.3d) over a scan area of 10 × 10 μm^2. Both the AFM results and Voronoi diagrams affirm quantitatively the hexagonal pattern transfer from the cp SiO_2 inverse colloidal template to the ncp c-Si nanostructures with almost 100 % fidelity.

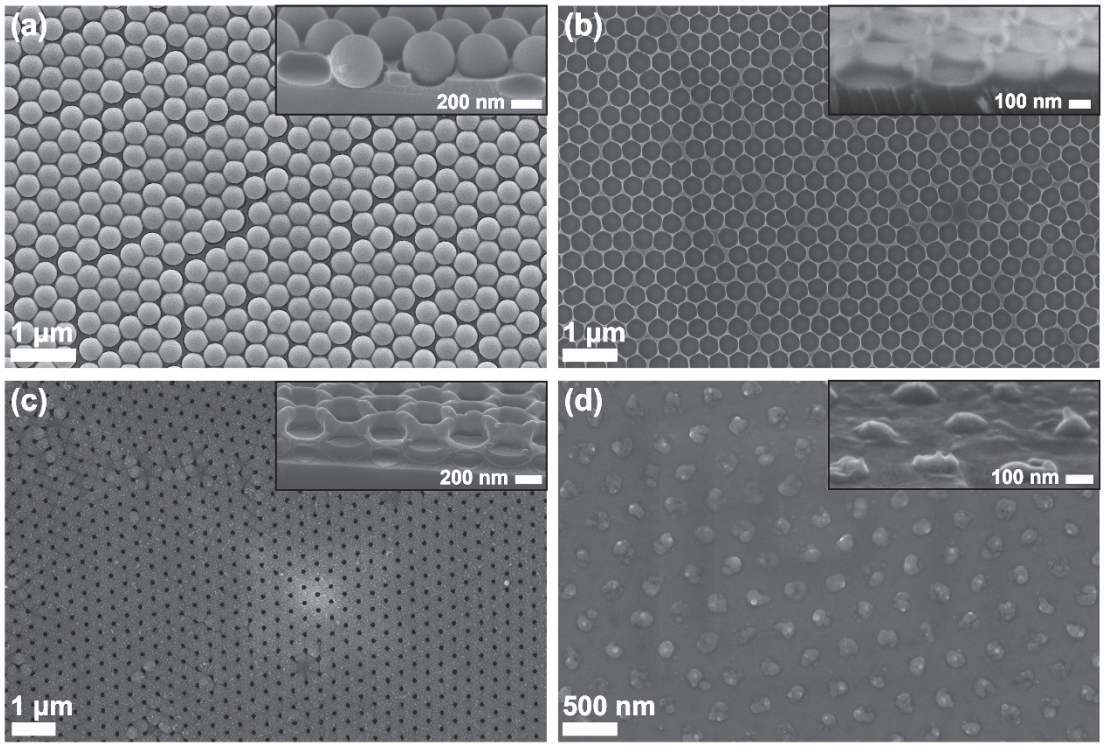

Figure 4.2. Plan view and cross-sectional (insets) SEM micrographs of samples formed and processed with PECVD a-Si deposition. (a) hcp PS monolayer colloidal crystal using 350 nm diameter beads surrounded by the SiO_2 matrix. (b) hcp SiO_2 inverse monolayer colloidal crystal after calcination. (c) a-Si overlayer deposited by PECVD. (d) hncp c-Si nanostructures after HF etching.

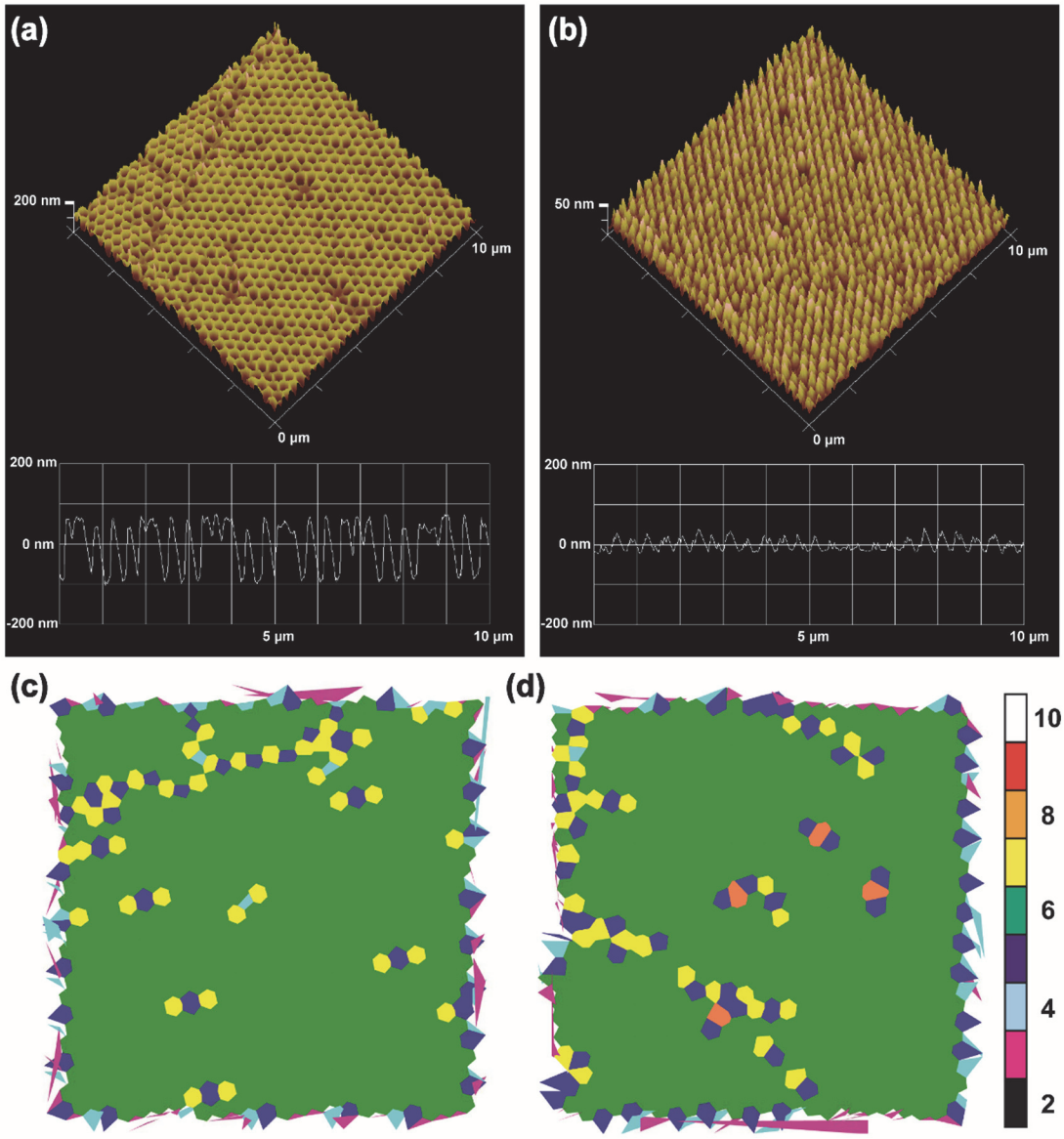

Figure 4.3. 3D AFM height profile images and corresponding Voronoi tessellation constructions of (a,c) the 350 nm hcp SiO_2 inverse monolayer colloidal crystal template and (b,d) the final hncp c-Si nanostructures of the PECVD sample. The vertical height axes range from (a) ±200 nm for the template and (b) ±50 nm for the c-Si nanostructures. The scan area for the AFM images and Voronoi analysis is 10 × 10 µm and the color bar indicates the number of sides of the calculated polygon. The vast majority of the scan areas show 6-fold neighbors with only isolated defect regions.

Beyond two dimensions, we applied the laser-induced transient melt process to obtain 3D ordered macroporous (3DOM) c-Si inverse opals with hncp symmetry based on micromolding in inverse silica opals (MISO).[5] We began with a multilayered SiO_2 inverse opal prepared by the FCVD method with 350 nm PS beads. Figure 4.4a shows the uniform deposition of hydrogenated a-Si by PECVD on the inner walls of the SiO_2 interconnected spherical cavities, yielding an hncp SiO_2/a-Si core-shell inverse colloidal crystal. The SiO_2/a-Si composite material was subsequently irradiated with a total of 43 sequential laser pulses at fluences from 5–550 mJ/cm^2. The low energy fluences allowed for a slow and controlled release of hydrogen while higher energies induced melt and converted the a-Si into c-Si retaining the inverse opal morphology. The open structure and SiO_2 template walls reduced the melt threshold from 600 to 550 mJ/cm^2. Selective HF etching of the SiO_2 template results in an all c-Si single network of hncp inverse opal morphology seen with four- and six-monolayer periodicities in Figures 4b and 4e, respectively. Energy dispersive X-ray (EDX) analysis indicates that the resulting laser-induced c-Si 3DOM material consists almost entirely of silicon (< 9 % residual oxygen content, data not shown).

Figures 4.4c and 4.4d display high magnification SEM micrographs of a-Si and c-Si inverse opals after HF etching, respectively. The darker contrast of the interstitial sites between three interconnecting quasi-spherical shells in both images suggests the placement of air voids that were formed after the removal of SiO_2 template and explicitly confirmed in the interior view of the a-Si inverse opal (Figure 4.4c). The white-dotted regions in Figure 4.4d highlights the quasi-cylindrical air channels connected to the quasi-spherical c-Si shells, a distinctive feature of hncp inverse opals.[5,6,25] From the SEM data, the quasi-spherical pore size in the laser-induced c-Si inverse opal material was reduced up to 40 % which can be attributed to the shrinkage

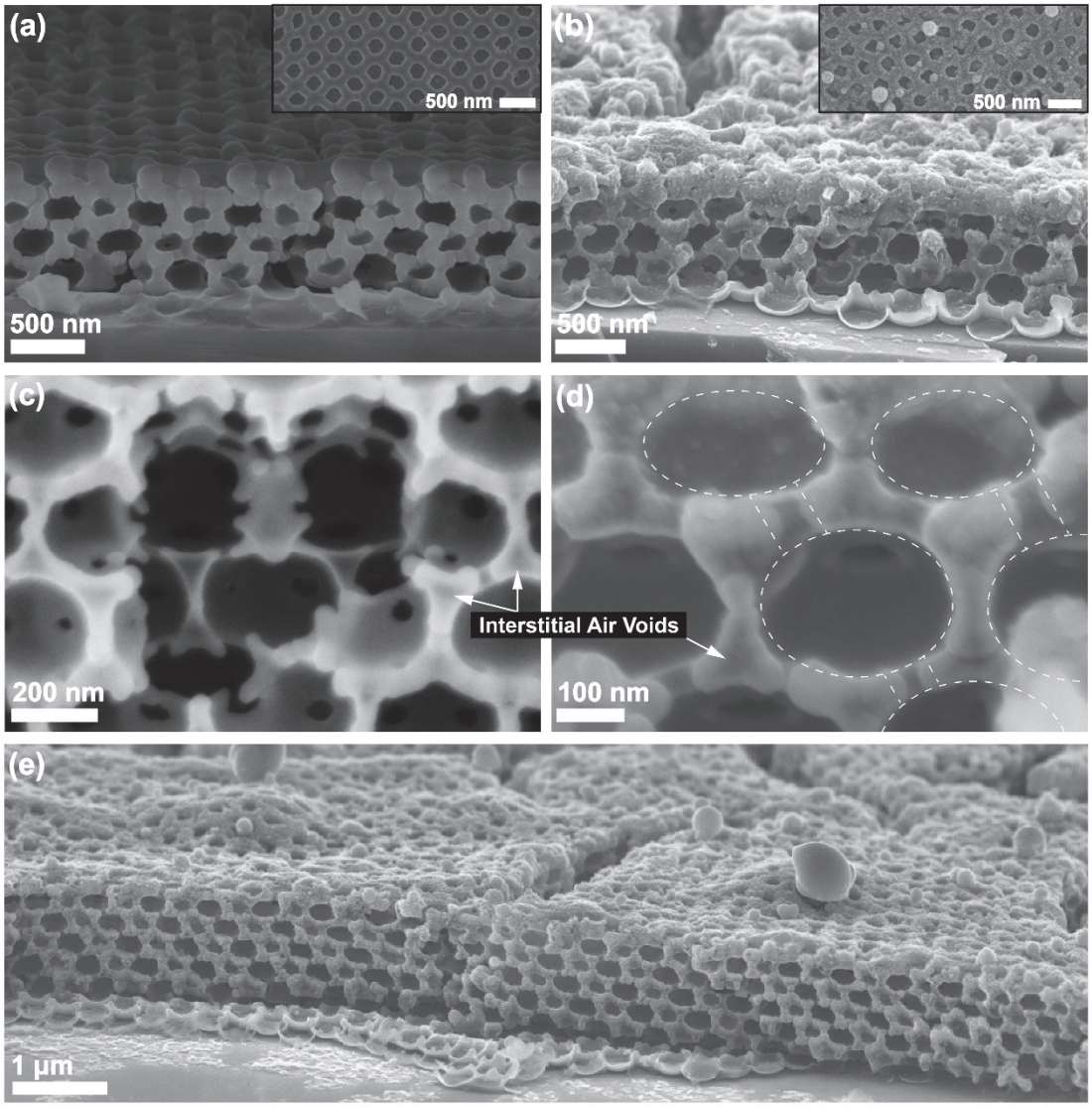

Figure 4.4. Cross-sectional and plan view (insets) SEM micrographs of (a) hncp SiO_2/a-Si core-shell composite inverse opal and (b) laser-induced hncp c-Si inverse opal nanostructures with four-monolayer-periodicity after HF etching. Cross-sectional SEM images of (c) HF-etched a-Si inverse opal and (d) HF-etched laser-induced c-Si inverse opal nanostructures in high magnifications. The white-dotted region lines in Figure 4d highlight the quasi-cylindrical air channels connected to the quasi-spherical c-Si shells. (e) Cross-sectional SEM micrograph of laser-induced hncp c-Si inverse opal nanostructures with six-monolayer-periodicity after HF etching.

of the SiO_2 template during calcination[23] and the thicker Si walls. This shrinkage is crucial to obtain the ncp symmetry. An interesting feature in the 3DOM nanostructures is the absence of dewetting of the molten Si from the SiO_2 pore walls. In contrast to the 2D nanoarrays, the absence of a clearly preferable single-crystal Si substrate could have resulted in the uniform a-Si melting within the porous structure.

For complete shape and structural control, we need to either fully dehydrogenate the PECVD a-Si film, deposit gas-free amorphous precursors, or irradiate in-situ after deposition to reduce the total number of laser pulses and accumulated silicon melt duration. We postulate the best method is to achieve homogenous nucleation and epitaxial growth of a single-crystal silicon nanostructure from the substrate.[40,54,55] In particular, we expect an interconnected and epitaxial ncp single-crystal 3D structure to facilitate optimal electrical charge transport properties and impart improved mechanical properties from the lack of grain boundaries. In analogy to results on block copolymer templates, this approach may not only be applied to form single-crystal homoepitaxial but also heteroepitaxial ncp nanostructured arrays on Si enabling new functionalities and the engineering of novel device prototypes.[40]

Conclusion

In conclusion, we have performed the first experiments to demonstrate a highly rapid and versatile method using colloidal crystal templates coupled with pulsed excimer laser-induced melting to obtain ncp c-Si arrays of varying scales at ambient conditions. The resulting hncp c-Si nanostructured arrays maintain uniform separations and excellent long-range order as established by the hcp colloidal crystal template. Our results suggest a general strategy coupling soft-matter self-assembly with pulsed laser

irradiation to direct and design intricate complex nanopatterned crystalline inorganic materials that could be used in advanced applications such as sensors, catalysis and energy conversion.

Methods

Colloidal Crystal Template Synthesis. PS colloids with diameters of 530 nm and 350 nm from Interfacial Dynamics and PolySciences, respectively, were used as received. Colloidal suspensions of 0.5 wt % were mixed in deionized water and hydrolyzed TEOS solution (TEOS:0.1 M HCl:EtOH, 1:1:1.5 by weight) as described elsewhere.[32] Si substrates used were cleaned with piranha solution (H_2SO_4:H_2O_2, 3:1 by volume) and rinsed profusely with deionized water before use. The PS colloidal crystal and surrounding SiO_2 matrix were grown on these substrates using the FCVD method.[41-43] The PS beads were removed by slow calcination at 500 °C for 2 hours at a ramp rate of 2 °C/min in air. TEOS (98 %, Sigma-Aldrich), HCl acid (37 %, VWR), absolute EtOH (Pharmco), H_2SO_4 acid (97 %, VWR), H_2O_2 (30 %, VWR) were used as received.

a-Si Deposition. a-Si was sputter-deposited into the 530 nm SiO_2 monolayer inverse opal template using a RF magnetron source with argon ions at a base pressure of 1.9×10^{-6} torr and deposition rate of 9.8 nm/min for 10 min. a-Si was deposited into the 350 nm SiO_2 monolayer inverse opal template by PECVD at 400 °C for 2.2 min with a deposition rate of 46 nm/min. a-Si was deposited into the (350 nm) multilayered SiO_2 inverse opal template by PECVD at 400 °C for 3.3 min with a deposition rate of 46 nm/min.

Excimer Laser Irradiation. The laser irradiation setup is described elsewhere.[40] Briefly, a 40 ns full-width-half-maximum pulsed XeCl excimer laser (308 nm wavelength) was used to melt the a-Si in the SiO_2 template. Reflectance of the sample surface was monitored using a 650 nm diode laser. The laser irradiated area on the sample was 3.2 × 3.2 mm. A single laser pulse of 600 mJ/cm^2 energy fluence was used to melt the 530 nm sputter-deposited a-Si monolayer sample. Four sequential laser pulses of 600, 700, 700 and 500 mJ/cm^2 energy fluences were used to melt the 350 nm PECVD a-Si monolayer sample. A total of 43 sequential laser pulses at fluences from 5 to 550 mJ/cm^2 were used to dehydrogenate and melt the 350 nm PECVD a-Si multilayered sample.

Template Removal. The sputter-deposited samples were treated in 20 % HF acid solution and PECVD samples were treated in 49 % HF acid solution for 3–5 min to completely dissolve the SiO_2 templates.

Characterization. AFM images were obtained on a Veeco Nanoscope III in tapping mode with TappingMode Etched Si Probe (325 kHz resonance frequency, 27 N/m force constant, 10 nm tip radius of curvature; all other values nominal) at ambient conditions. A LEO 1550 field emission SEM equipped with an in-lens detector and an EDX spectrometer (Quantax EDS, XFlash 3000 silicon drift detector, Bruker Nano GmbH) was used to image and identify the EDX signals of the samples. Voronoi tessellation diagrams were constructed using a self-written algorithm.[40,53]

Acknowledgement

This work was supported by a National Science Foundation (NSF) creativity award (grant no. DMR-0605856) and support by the U.S. Department of Homeland

Security under Cooperative Agreement Number 2009-ST-108-LR0004. K.W.T. gratefully acknowledges the Singapore Energy Innovation Programme Office for a National Research Foundation graduate fellowship. S.A.S. gratefully acknowledges Cornell University and the Semiconductor Research Corporation with support from Intel Foundation for an Engineering Learning Initiatives undergraduate research award. M.O.T. gratefully acknowledges financial support from Panasonic Corporation. The use of facilities of the Cornell Center for Materials Research, with funding from the Materials Research Science and Engineering Center program of NSF (under cooperative agreement no. DMR-0520404), and of the Cornell Nanoscale Science and Technology Facility supported by NSF (under grant no. ECS-0335765) is gratefully acknowledged. The authors also thank Prof. C. Liddell, J. Drewes, J. Drumheller, E. Riley, and H. Sai of Cornell University and Prof. Q. Yan of Tsinghua University for helpful discussions and kind experimental assistance.

REFERENCES

(1) Lin, S. Y.; Fleming, J. G.; Hetherington, D. L.; Smith, B. K.; Biswas, R.; Ho, K. M.; Sigalas, M. M.; Zubrzycki, W.; Kurtz, S. R.; Bur, J. A Three-Dimensional Photonic Crystal Operating at Infrared Wavelengths. *Nature* **1998**, *394*, 251-253.

(2) Blanco, A.; Chomski, E.; Grabtchak, S.; Ibisate, M.; John, S.; Leonard, S. W.; Lopez, C.; Meseguer, F.; Miguez, H.; Mondia, J. P. *et al*. Large-Scale Synthesis of a Silicon Photonic Crystal with a Complete Three-Dimensional Bandgap near 1.5 Micrometres. *Nature* **2000**, *405*, 437-440.

(3) Vlasov, Y. A.; Bo, X.-Z.; Sturm, J. C.; Norris, D. J. On-Chip Natural Assembly of Silicon Photonic Bandgap Crystals. *Nature* **2001**, *414*, 289-293.

(4) Ibisate, M.; Golmayo, D.; López, C. Silicon Direct Opals. *Adv. Mater.* **2009**, *21*, 2899-2902.

(5) Míguez, H.; Tétreault, N.; Yang, S. M.; Kitaev, V.; Ozin, G. A. A New Synthetic Approach to Silicon Colloidal Photonic Crystals with a Novel Topology and an Omni-Directional Photonic Bandgap: Micromolding in Inverse Silica Opal (MISO). *Adv. Mater.* **2003**, *15*, 597-600.

(6) Blanco, A.; López, C. Silicon Onion-Layer Nanostructures Arranged in Three Dimensions. *Adv. Mater.* **2006**, *18*, 1593-1597.

(7) Tian, B.; Zheng, X.; Kempa, T. J.; Fang, Y.; Yu, N.; Yu, G.; Huang, J.; Lieber, C. M. Coaxial Silicon Nanowires as Solar Cells and Nanoelectronic Power Sources. *Nature* **2007**, *449*, 885-889.

(8) Garnett, E. C.; Yang, P. Silicon Nanowire Radial p−n Junction Solar Cells. *J. Am. Chem. Soc* **2008**, *130*, 9224-9225.

(9) Kelzenberg, M. D.; Boettcher, S. W.; Petykiewicz, J. A.; Turner-Evans, D. B.; Putnam, M. C.; Warren, E. L.; Spurgeon, J. M.; Briggs, R. M.; Lewis, N. S.; Atwater, H. A. Enhanced Absorption and Carrier Collection in Si Wire Arrays for Photovoltaic Applications. *Nat. Mater.* **2010**, *9*, 239-244.

(10) Suezaki, T.; Chen, J. I. L.; Hatayama, T.; Fuyuki, T.; Ozin, G. A. Electrical Properties of p-Type and n-Type Doped Inverse Silicon Opals - Towards Optically Amplified Silicon Solar Cells. *Appl. Phys. Lett.* **2010**, *96*, 242102.

(11) Taira, K.; Nakata, J. Silicon Cells: Catching Rays. *Nat. Photon.* **2010**, *4*, 602-603.

(12) Xu, S.; Huang, S. Y.; Levchenko, I.; Zhou, H. P.; Wei, D. Y.; Xiao, S. Q.; Xu, L. X.; Yan, W. S.; Ostrikov, K. Highly Efficient Silicon Nanoarray Solar Cells by a Single-Step Plasma-Based Process. *Adv. Energy Mater.* **2011**, *1*, 373-376.

(13) Lin, V. S.-Y. Motesharei, K. Dancil, K.-P. S. Sailor, M. J.; Ghadiri, M. R. A Porous Silicon-Based Optical Interferometric Biosensor. *Science* **1997**, *278*, 840 -843.

(14) Cui, Y.; Wei, Q.; Park, H.; Lieber, C. M. Nanowire Nanosensors for Highly Sensitive and Selective Detection of Biological and Chemical Species. *Science* **2001**, *293*, 1289 -1292.

(15) Li, D.; Wu, Y.; Kim, P.; Shi, L.; Yang, P.; Majumdar, A. Thermal Conductivity of Individual Silicon Nanowires. *Appl. Phys. Lett.* **2003**, *83*, 2934.

(16) Boukai, A. I.; Bunimovich, Y.; Tahir-Kheli, J.; Yu, J.-K.; Goddard III, W. A.; Heath, J. R. Silicon Nanowires as Efficient Thermoelectric Materials. *Nature* **2008**, *451*, 168-171.

(17) Hochbaum, A. I.; Chen, R.; Delgado, R. D.; Liang, W.; Garnett, E. C.; Najarian, M.; Majumdar, A.; Yang, P. Enhanced Thermoelectric Performance of Rough Silicon Nanowires. *Nature* **2008**, *451*, 163-167.

(18) Lee, J.-H.; Galli, G. A.; Grossman, J. C. Nanoporous Si as an Efficient Thermoelectric Material. *Nano Lett.* **2008**, *8*, 3750-3754.

(19) Yu, J.-K.; Mitrovic, S.; Tham, D.; Varghese, J.; Heath, J. R. Reduction of Thermal Conductivity in Phononic Nanomesh Structures. *Nat. Nano.* **2010**, *5*, 718-721.

(20) Tang, J.; Wang, H.-T.; Lee, D. H.; Fardy, M.; Huo, Z.; Russell, T. P.; Yang, P. Holey Silicon as an Efficient Thermoelectric Material. *Nano Lett.* **2010**, *10*, 4279-4283.

(21) Li, Y.; Cai, W.; Duan, G. Ordered Micro/Nanostructured Arrays Based on the Monolayer Colloidal Crystals. *Chem. Mater.* **2008**, *20*, 615-624.

(22) Zhang, J.; Li, Y.; Zhang, X.; Yang, B. Colloidal Self-Assembly Meets Nanofabrication: From Two-Dimensional Colloidal Crystals to Nanostructure Arrays. *Adv. Mater.* **2010**, *22*, 4249-4269.

(23) Stein, A.; Li, F.; Denny, N. R. Morphological Control in Colloidal Crystal Templating of Inverse Opals, Hierarchical Structures, and Shaped Particles. *Chem. Mater.* **2008**, *20*, 649-666.

(24) Fenollosa, R.; Meseguer, F. Non-Close-Packed Artificial Opals. *Adv. Mater.* **2003**, *15*, 1282-1285.

(25) King, J. S.; Gaillot, D. P.; Graugnard, E.; Summers, C. J. Conformally Back-Filled, Non-Close-Packed Inverse-Opal Photonic Crystals. *Adv. Mater.* **2006**, *18*, 1063-1067.

(26) Li, Y.; Sasaki, T.; Shimizu, Y.; Koshizaki, N. A Hierarchically Ordered TiO_2 Hemispherical Particle Array with Hexagonal-Non-Close-Packed Tops: Synthesis and Stable Superhydrophilicity without UV Irradiation. *Small* **2008**, *4*, 2286-2291.

(27) Gao, S.; Koshizaki, N.; Li, Y.; Li, L. Unique Hexagonal Non-Close-Packed Arrays of Alumina Obtained by Plasma Etching/Deposition with Catalytic Performance. *J. Mater. Chem.* **2011**, *21*, 2087.

(28) Isa, L.; Kumar, K.; Müller, M.; Grolig, J.; Textor, M.; Reimhult, E. Particle Lithography from Colloidal Self-Assembly at Liquid−Liquid Interfaces. *ACS Nano* **2010**, *4*, 5665-5670.

(29) Suezaki, T.; O'Brien, P. G.; Chen, J. I. L.; Loso, E.; Kherani, N. P.; Ozin, G. A. Tailoring the Electrical Properties of Inverse Silicon Opals - A Step Towards Optically Amplified Silicon Solar Cells. *Adv. Mater.* **2009**, *21*, 559-563.

(30) Bao, Z.; Weatherspoon, M. R.; Shian, S.; Cai, Y.; Graham, P. D.; Allan, S. M.; Ahmad, G.; Dickerson, M. B.; Church, B. C.; Kang, Z. *et al*. Chemical Reduction of Three-Dimensional Silica Micro-Assemblies into Microporous Silicon Replicas. *Nature* **2007**, *446*, 172-175.

(31) Richman, E. K.; Kang, C. B.; Brezesinski, T.; Tolbert, S. H. Ordered Mesoporous Silicon through Magnesium Reduction of Polymer Templated Silica Thin Films. *Nano Lett.* **2008**, *8*, 3075-3079.

(32) Hatton, B.; Mishchenko, L.; Davis, S.; Sandhage, K. H.; Aizenberg, J. Assembly of Large-Area, Highly Ordered, Crack-Free Inverse Opal Films. *P. Natl. Acad. Sci. USA* **2010**, *107*, 10354 -10359.

(33) Poate, J. M.; Mayer, J. W. *Laser Annealing of Semiconductors*; Academic Press: New York, 1982.

(34) Street, R. *Technology and Applications of Amorphous Silicon*; Springer: New York, 2000.

(35) Chou, S. Y.; Keimel, C.; Gu, J. Ultrafast and Direct Imprint of Nanostructures in Silicon. *Nature* **2002**, *417*, 835-837.

(36) Mendu, K. K.; Shi, J.; Lu, Y. F.; Li, L. P.; Batta, N.; Doerr, D. W.; Alexander, D. R. Fabrication of Multi-Layered Inverse Opals Using Laser-Assisted Imprinting. *Nanotechnology* **2005**, *16*, 1965-1968.

(37) Lu, Y.; Chen, S. C. Nanopatterning of a Silicon Surface by Near-Field Enhanced Laser Irradiation. *Nanotechnology* **2003**, *14*, 505-508.

(38) Brodoceanu, D.; Landström, L.; Bäuerle, D. Laser-Induced Nanopatterning of Silicon with Colloidal Monolayers. *Appl. Phys. A* **2006**, *86*, 313-314.

(39) Li, L.; Guo, W.; Wang, Z. B.; Liu, Z.; Whitehead, D.; Luk'yanchuk, B. Large-Area Laser Nano-Texturing with User-Defined Patterns. *J. Micromech. Microeng.* **2009**, *19*, 054002.

(40) Arora, H.; Du, P.; Tan, K. W.; Hyun, J. K.; Grazul, J.; Xin, H. L.; Muller, D. A.; Thompson, M. O.; Wiesner, U. Block Copolymer Self-Assembly–Directed Single-Crystal Homo- and Heteroepitaxial Nanostructures. *Science* **2010**, *330*, 214 -219.

(41) Zhou, Z.; Zhao, X. S. Opal and Inverse Opal Fabricated with a Flow-Controlled Vertical Deposition Method. *Langmuir* **2005**, *21*, 4717-4723.

(42) Tan, K. W.; Li, G.; Koh, Y. K.; Yan, Q.; Wong, C. C. Layer-by-Layer Growth of Attractive Binary Colloidal Particles. *Langmuir* **2008**, *24*, 9273-9278.

(43) Tan, K. W.; Koh, Y. K.; Chiang, Y.-M.; Wong, C. C. Particulate Mobility in Vertical Deposition of Attractive Monolayer Colloidal Crystals. *Langmuir* **2010**, *26*, 7093-7100.

(44) Auston, D. H.; Surko, C. M.; Venkatesan, T. N. C.; Slusher, R. E.; Golovchenko, J. A. Time-Resolved Reflectivity of Ion-Implanted Silicon During Laser Annealing. *Appl. Phys. Lett.* **1978**, *33*, 437.

(45) Thompson, M. O.; Galvin, G. J.; Mayer, J. W.; Peercy, P. S.; Poate, J. M.; Jacobson, D. C.; Cullis, A. G.; Chew, N. G. Melting Temperature and Explosive Crystallization of Amorphous Silicon During Pulsed Laser Irradiation. *Phys. Rev. Lett.* **1984**, *52*, 2360.

(46) Giermann, A. L.; Thompson, C. V. Solid-State Dewetting for Ordered Arrays of Crystallographically Oriented Metal Particles. *Appl. Phys. Lett.* **2005**, *86*, 121903.

(47) Oh, Y.-J.; Ross, C. A.; Jung, Y. S.; Wang, Y.; Thompson, C. V. Cobalt Nanoparticle Arrays Made by Templated Solid-State Dewetting. *Small* **2009**, *5*, 860-865.

(48) Li, J. G.; Hausner, H. Wetting and Adhesion in Liquid Silicon/Ceramic Systems. *Mater. Lett.* **1992**, *14*, 329-332.

(49) Fork, D. K.; Anderson, G. B.; Boyce, J. B.; Johnson, R. I.; Mei, P. Capillary Waves in Pulsed Excimer Laser Crystallized Amorphous Silicon. *Appl. Phys. Lett.* **1996**, *68*, 2138.

(50) Mei, P.; Boyce, J. B.; Hack, M.; Lujan, R. A.; Johnson, R. I.; Anderson, G. B.; Fork, D. K.; Ready, S. E. Laser Dehydrogenation/Crystallization of Plasma-Enhanced Chemical Vapor Deposited Amorphous Silicon for Hybrid Thin Film Transistors. *Appl. Phys. Lett.* **1994**, *64*, 1132.

(51) McCulloch, D. J.; Brotherton, S. D. Surface Roughness Effects in Laser Crystallized Polycrystalline Silicon. *Appl. Phys. Lett.* **1995**, *66*, 2060.

(52) Riley, E. K.; Liddell, C. M. Confinement-Controlled Self Assembly of Colloids with Simultaneous Isotropic and Anisotropic Cross-Section. *Langmuir* **2010**, *26*, 11648-11656.

(53) Voronoi and Nearest Neighbor Pattern Analysis Algorithms. http://people.ccmr.cornell.edu/~uli/pages/idl.htm (accessed Mar 11, 2011).

(54) Hu, S.; Leu, P. W.; Marshall, A. F.; McIntyre, P. C. Single-Crystal Germanium Layers Grown on Silicon by Nanowire Seeding. *Nat. Nano.* **2009**, *4*, 649-653.

(55) Nelson, E. C.; Dias, N. L.; Bassett, K. P.; Dunham, S. N.; Verma, V.; Miyake, M.; Wiltzius, P.; Rogers, J. A.; Coleman, J. J.; Li, X.; *et al*. Epitaxial Growth of Three-Dimensionally Architectured Optoelectronic Devices. *Nat. Mater.* **2011**, *10*, 676-681.

APPENDIX C

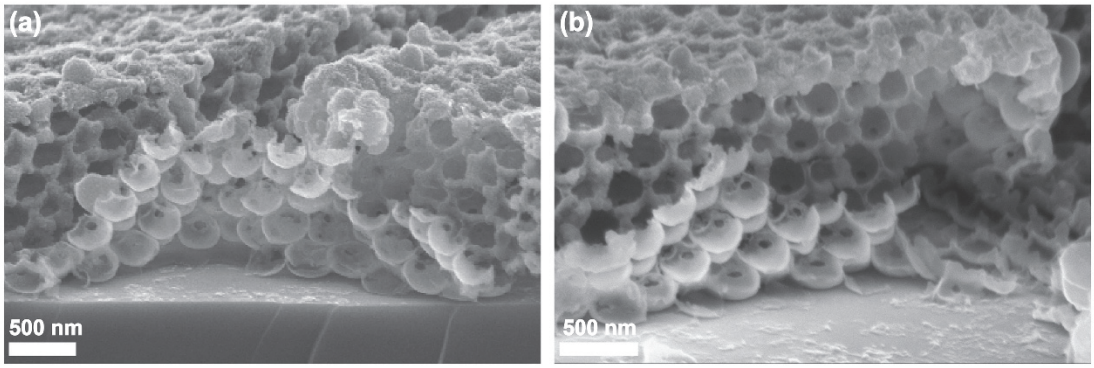

Figure S4.1. (a,b) Cross-sectional SEM micrographs of the laser-induced 3DOM hncp crystalline silicon nanostructures showing the open quasi-spherical shells.

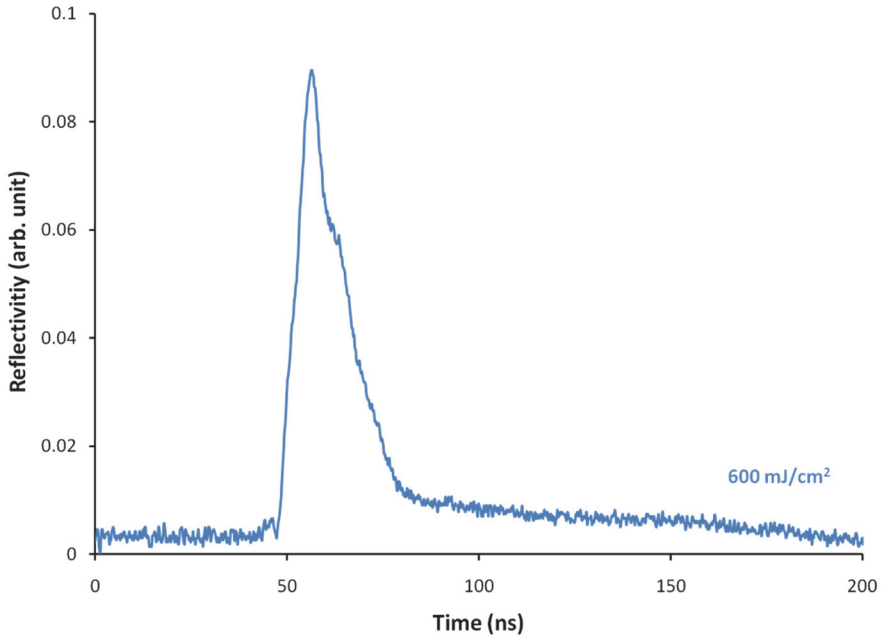

Figure S4.2. Time resolved reflectance signal of sample. The silicon surface is irradiated by a single 40 ns XeCl excimer laser pulse (308 nm wavelength) of 600 mJ/cm^2 energy fluence. The higher reflectivity indicates silicon in the molten state. The signal trace clearly establishes recrystallization into crystalline silicon after 30 ns.

CHAPTER 5

DIRECT LASER WRITING OF BLOCK COPOLYMER SELF-ASSEMBLY-DIRECTED HIERARCHICAL POROUS STRUCTURES

Abstract

Bottom-up synthetic methods using atomic and molecular building blocks provide access to complex and composite porous materials at the mesoscale (2-50 nm) for emerging technologies and applications[1–3]. In particular, block copolymer (BCP) self-assembly has been adapted to synthesize mesoporous and hierarchical porous structures for catalysis, membrane filtration and bioengineering[4–9]. Despite significant progress in the field of organic molecule-directed self-assembly to fabricate tunable pore size structures, time-consuming post-processing treatments are often required to generate the desired final properties[10–19]. Moreover, a rapid single-step process that can simultaneously provide control over mesoscopic pore structure and macroscopic material shape has not yet been demonstrated. Here we describe a method providing direct access to porous three-dimensionally (3D) continuous polymer network structures and shapes by combining BCP-resol co-assembly with CO_2 laser-induced transient heating. The CO_2 laser source transiently heats the BCP-directed resol hybrid films to high temperatures at the beam position, inducing locally controlled resol theromopolymerization and BCP decomposition. This enables shaping of BCP-directed porous resin structures with tunable 3D interconnected pores in a single process. Pore size can be varied from as small as 10 nm to sub-micrometer scale of ~600 nm. Carbonization at high temperatures imparts additional electrical conductivity to the porous structures. Together with the chemical, mechanical and thermal properties of the

hierarchical porous resin structures, the method may enable further adaptation to a number of applications, including microfluidics, sensing and energy storage[3,9,20,21].

Tan, K. W., Jung, B., Werner, J. G., Rhoades, E. R., Thompson, M. O. & Wiesner, U. To be submitted for publication.

Introduction

Porous materials with structures bridging from nano- to macroscopic length scales are expected to open new frontiers for a wide variety of emerging applications[1–3]. Well-ordered mesoporous materials derived from small-molecule surfactant and BCP self-assembly have been explored extensively over the past two decades in the form of amorphous[4,5,10–13,15,22,23], polycrystalline[14,16–18] and single crystal[19] solids. Multiple time consuming processing steps are often required to generate the final structures. For example, the removal of organic components by conventional thermal processing to create the desired porosity typically takes several hours (~10^4-10^5 s)[4,5,13,14,17–19,22,23]. Several methods to fabricate hierarchical porous polymer scaffolds using BCPs have recently been devised that circumvent some of the complexities of previous approaches, but they still involve multiple steps, and control over macroscopic shape is limited[6–9].

Laser-induced transient heating of organic materials has been explored as an alternative thermal annealing approach to alter morphology as well as materials properties and to enable direct pattern transfer[24–27]. By reducing the heating duration to 0.5 ms, CO_2 laser-induced transient heating (λ = 10.6 μm) significantly enhanced the temperature stability of a methacrylate based photoresist by ~400 °C compared to a 60 s hotplate heat treatment[24]. However, severe film degradation and extensive damage was observed for CO_2 laser spike annealing of polystyrene-*block*-polymethyl methacrylate copolymer thin films on longer dwells (>10 ms)[25]. One dimensional (1D) grating patterns were formed in polystyrene thin films by thermocapillary dewetting effects induced with a green laser (λ = 532 nm) of ~10 ms dwell, however, the line-edge roughness increased as line spacing widths decreased[26]. A contrasting example is transient heating of semiconducting polyaniline nanofibers with a near-infrared laser (λ = 788 nm) resulting in welded films with reduced electrical conductivity[27].

Here we demonstrate a simple and rapid method for the direct generation of 3D porous organic structures and shapes in a single process by combining BCP self-assembly directed resol structure formation with CO_2 laser-induced transient heating. A schematic of block copolymer-based writing induced by transient heating experiments (B-WRITE) method is shown in Fig.1a. Two polyisoprene-*block*-polystyrene-*block*-polyethylene oxide (PI-*b*-PS-*b*-PEO, ISO) triblock terpolymers were synthesized by anionic polymerization with polydispersity indexes of 1.07 and 1.04, molar masses of 38.3 kg/mol and 68.9 kg/mol, and compositions of, 68.4 wt% PI, 18.0 wt% PS, and 13.6 wt% PEO (ISO-38) and 29.6 wt% PI, 64.8 wt% PS, and 5.6 wt% PEO (ISO-69), respectively[23]. In Stage I, the structure-directing ISO was mixed with resorcinol-formaldehyde resol oligomers to form an organic-organic hybrid thin film by spin-coating on a highly boron-doped silicon (Si) substrate and cured at 100 °C[23]. In Stage II, the hybrid thin film was heated by a continuous wave CO_2 laser focused into a ~90 μm by 600 μm beam of a 0.5 ms dwell[24]. The hybrid film does not strongly interact the far infrared photons below a critical thickness (vide infra) with Si absorbing most of the photons to heat the surface and cooled by thermal conduction on sub-millisecond timeframes[24]. The cured resol additives were thermopolymerized by a series of increasing laser powers (10-35 W ≈ 125-550 °C) to form highly crosslinked phenolic resins[22,23]. Finally, a higher laser power (40 W ≈ 670 °C) induced transient ISO decomposition and resulted in nanoporous phenolic resin structures in Stage III. This unique combination of positive-tone ISO and negative-tone resol additives with CO_2 laser-induced transient heating enables direct writing of mesoporous resin structures in a single process. In the following, the samples are designated as ISO-X-R-Y, where X is the ISO molar mass, R denotes the resols and Y represents the heat treatment method (BW: B-WRITE; CA: calcination-in-air; CN: calcination-in-nitrogen). Temperatures associated with laser heating experiments were determined using a method described

elsewhere[24].

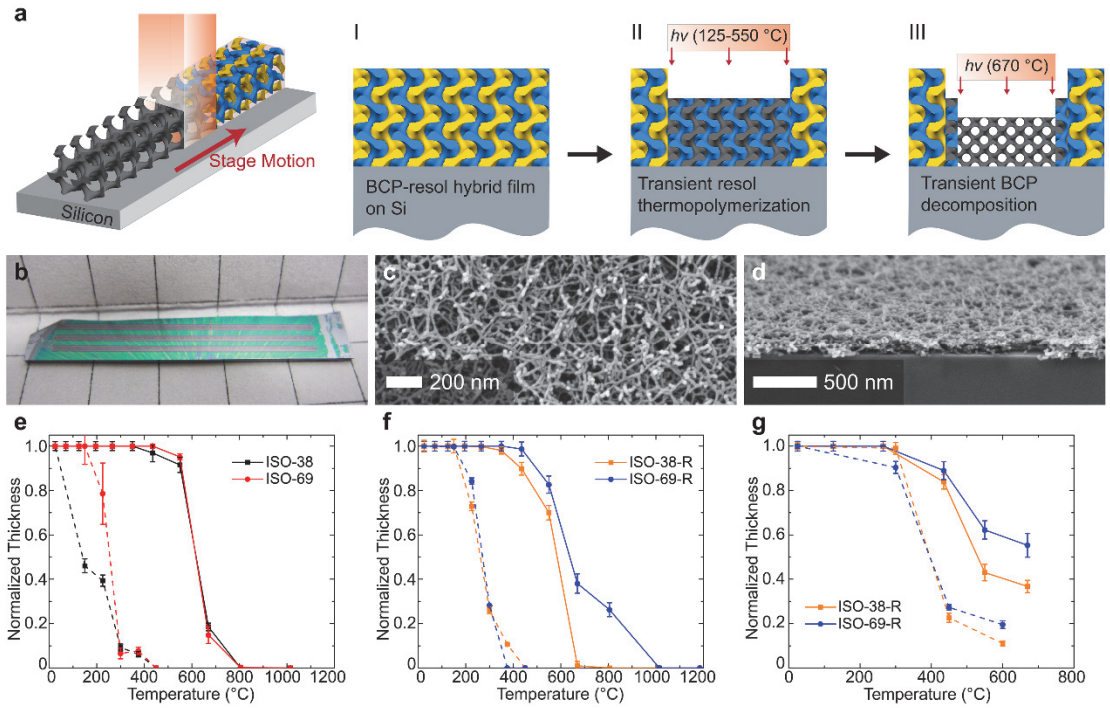

Figure 5.1. Direct laser writing of BCP-directed resol hybrid samples using the B-WRITE method. a, Schematic representation. b-d, Optical (b), plan view (c) and cross-sectional (d) SEM micrographs of nanoporous phenolic resin grating pattern in a 6 wt% ISO-38-R hybrid sample. Each trench was direct-laser-written in less than 5 min. The grid paper has 5 mm markings. e and f, Normalized thickness plots of neat 5 wt% ISO (e) and 6 wt% ISO-resol (f) thin film samples remaining after heated by a single CO_2 laser irradiation (solid lines) and furnace calcination in air (dotted lines). g, Normalized thickness plot of 6 wt% ISO-resol hybrid samples heated by multiple passes of CO_2 laser irradiation (solid lines) and furnace calcination in nitrogen (dotted lines).

As a first example, a 6 wt% ISO-38-R hybrid sample was deposited on Si by spin-coating a solution of ISO-38 terpolymer mixed at a mass ratio of 3:1 with oligomeric resols in tetrahydrofuran (THF), followed by curing at 100 °C (Table S5.1). We

determined 20 passes at sequential laser powers of 10-30 W (125-435 °C) and 10 passes at 35 W (550 °C) were able to crosslink the cured resols into resin and inhibit thermocapillary dewetting[26]. A total of 10 passes at 40 W laser power (670 °C) induced ISO decomposition to generate porosity. The optical image in Fig. 5.1b shows linear trenches in the cured ISO-38-R hybrid film generated by the B-WRITE method. Each trench was ~2 cm long and took roughly 4 min 35 s (~10^2 s) to fabricate in air. Scanning electron microscopy (SEM, Fig. 5.1c,d) and profilometry (Fig. S5.1b) show that the ~150 μm wide trench consists of a ~200 nm thick nanoporous resin thin film with continuous 3D network structure. In order to better understand the thermal behavior of the organic films under CO_2 laser-induced transient heating, we employed SEM, profilometry, and Fourier transform infrared spectroscopy (FTIR) to investigate film morphology, thickness and chemical composition for different laser heating temperatures as compared to furnace calcination.

We first investigated films on Si spin coated from 5 wt% neat ISO-38/69 solutions and 6 wt% ISO-38/69-R mixed solutions (Table S5.1) in THF and annealed by either furnace calcination (dotted lines) in air for 1 h or by a single CO_2 laser irradiation (solid lines) of 0.5 ms dwell (Fig.1e,f). The ISO-69-R sample was prepared by mixing ISO-38 terpolymer with oligomeric resols at a mass ratio of 2.4:1 in tetrahydrofuran (THF), followed by curing at 100 °C. It is apparent from Fig. 5.1e and f that for both neat ISO and mixed ISO-resol thin film samples, thermal stability is dramatically increased by more than 300 °C when moving from annealing durations of 1 h in a furnace to 0.5 ms with CO_2 laser-induced transient heating. We note that the nanoporous resin structure was formed by a single laser irradiation at 670 °C, however, film delamination occurred attributed to thermocapillary dewetting effects[26]. To this end, we introduced multiple passes of sequential CO_2 laser powers for the B-WRITE method. The lower laser powers

(125-550 °C) allowed for a more controlled polymerization of the cured resols, while the higher power (670 °C) induced ISO decomposition, leaving an uniform nanoporous resin network structure (Fig. 5.1b-d, 5.2 and S5.1).

Two similar annealing temperature regimes were also observed in Fig. 5.1g for both neat ISO and ISO-resol thin film samples heated by furnace calcination in nitrogen for 1-3 h (dotted lines) and multiple CO_2 laser irradiation passes of 0.5 ms dwell (solid lines). During calcination in nitrogen, both ISO and resol components in the hybrid samples remained thermally stable up to 300 °C retaining over 90% film thickness; however, film thickness decreased rapidly to 20-30% at 450 °C and 10-20% at 600 °C. The rapid thickness loss is attributed mainly to crosslinking of resols[22,23] and ISO decomposition at 450 °C (see thermogravimetric analysis, Fig. S5.2) to form the mesoporous resin structure observed in SEM (Fig. 5.2d,h). This is consistent with most of the FTIR intensity peaks vanishing at 450 and 600 °C in nitrogen (Fig. S5.2b,c)[22,28]. The mesoporous structure is constituted of crosslinked phenolic resin at 450 °C and amorphous carbon at 600 °C[22,23]. ISO-resol hybrid samples heated by the B-WRITE method in air retained over 80% of the original thickness below 435 °C and a high 35-55% at 670 °C (Fig. 5.1g). From FTIR (Fig. S5.2b,c), the hydroxyl intensity peak in the 3200-3500 cm^{-1} band decreased steadily from ambient to 435 °C, indicating crosslinking of cured resols into resin by transient heating[22,23,28]. The alkyl stretching vibrational peaks in the 2800-3000 cm^{-1} band assigned to the ISO terpolymers remained relatively unchanged up to 435 °C and diminished significantly from 550-670 °C, indicating ISO decomposition[22,23,28]. Taken together with SEM characterization, we infer the cured ISO-resol hybrid films (Fig. 5.2a,e) underwent densification attributed to crosslinking of resols and loss of low molecular weight by-products with increasing transient temperatures up to 435 °C[22]. At 550 °C there was sufficient thermal energy to

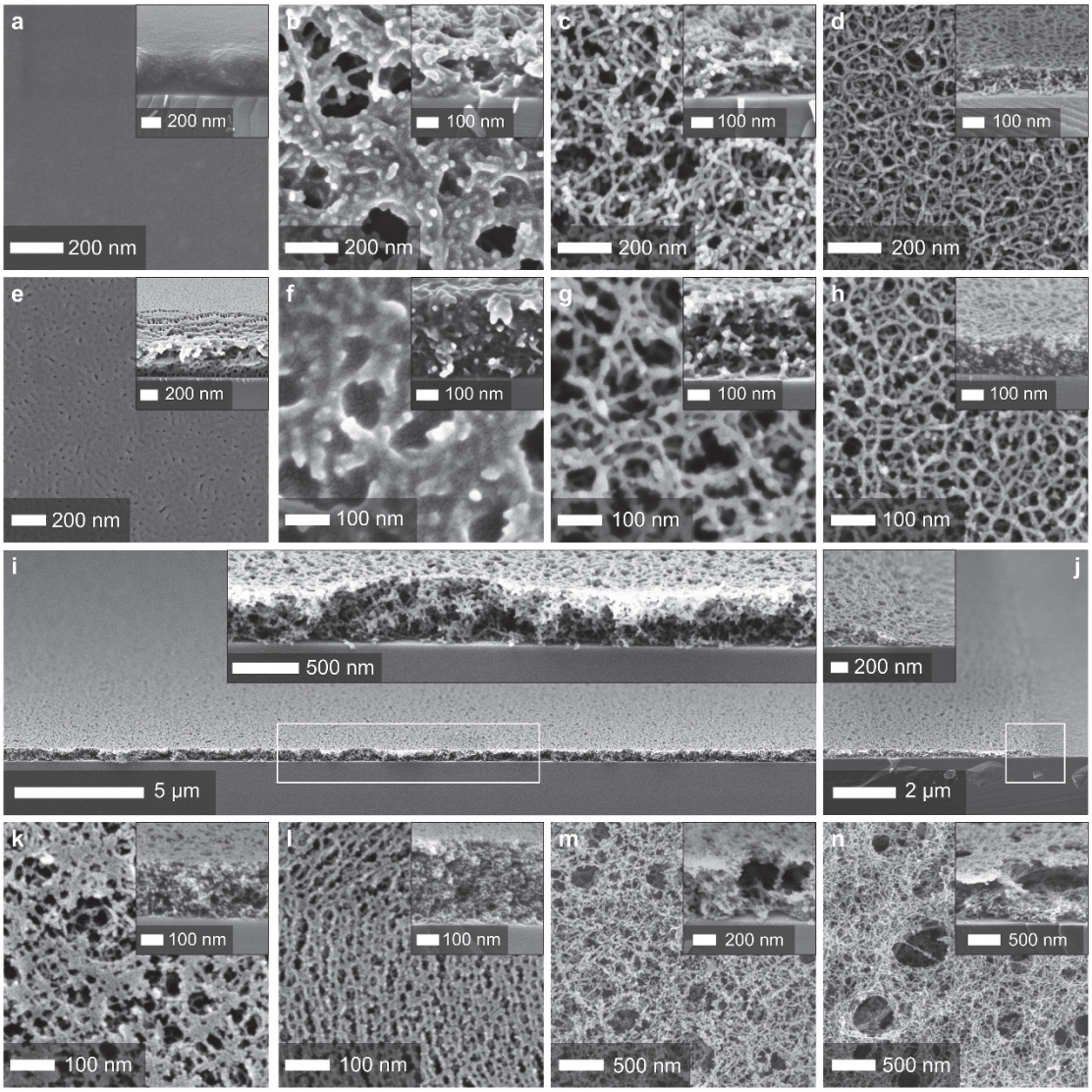

Figure 5.2. SEM characterization of porous resin structures. a to h, Plan view and cross-sectional (insets) images of 6 wt% ISO-38-R (a-d) and 6 wt% ISO-69-R (e-h) samples at ambient temperature after curing (a and e); 550 °C (b and f) and 670 °C (c and g) by transient heating; and 450 °C (d and h) by furnace calcination in nitrogen, respectively. i and j, Macroscopic cross-sectional SEM images of 6 wt% ISO-69-R-BW nanoporous resin network structure. Insets show the white boxed cross-sections in high magnifications. The straight edge in (j) was formed by a single CO_2 laser irradiation at 30 W of 25 ms dwell. k and l, Plan view and cross-sectional (inset) images of 20 wt% F127-R-BW mesoporous resin samples of 1:1 (k) and 1:2 (l) mass ratios, respectively. m and n, Plan view and cross-sectional (inset) images of 10 wt% (m) and 12.5 wt% (n) ISO-38-R-BW hierarchical porous resin structures.

initiate ISO decomposition (Fig. 5.2b,f). The resulting nanoporous resin network structure was formed when ISO terpolymers mostly decomposed at 670 °C (Fig. 5.2c,g).

Although thermal stability of ISO-resol hybrid thin films was enhanced by a smaller value of ~200 °C, the nanoporous resin structure generated by B-WRITE method were thicker than conventional pyrolysed resin structure by approximately threefold at the respective final annealing temperatures (Fig. 5.1g). SEM suggests pore size and porosity of the resin structure is dependent on the heat treatments (compare Fig. 5.2c,d and 5.2g,h). We performed fast Fourier transform (FFT) analysis on plan view SEM images of ISO-69-R resin structures and plotted the radially integrated intensity against the reciprocal space scattering vector q (Fig. S5.3a). The integrated intensity peak for ISO-69-R-CN mesoporous resin samples formed at 450 °C in nitrogen corresponds to an estimated homogenous characteristic length scale of ~48.2 nm in the in-plane direction. In contrast, porosity of ISO-69-R-BW samples is estimated to be macroscopically inhomogeneous with a wide pore size distribution of 30-200 nm (Fig. 5.2g and S5.3a). Nonetheless, lower magnification cross-sectional view SEM images in Fig. 5.2i and j show the ISO-69-R-BW nanoporous resin network structure is highly uniform over large areas defined by the CO_2 laser. The increase in porosity is ascribed to the rapid evolution and release of gaseous decomposition products during transient heating causing the local expansion of pores and structure thicknesses[29,30].

To illustrate the versatility of the B-WRITE method, we varied the structure-directing BCP and experimental parameters to control pore formation during transient heating. First, we changed the hybrid system using the smaller molecular weight Pluronic F127 BCP surfactant mixed with phenol-formaldehyde resols at 1:1 mass ratio in ethanol[22,23] to form mesoporous resin structure with pore sizes of 20-50 nm (Fig. 5.2k). By decreasing the F127 to resol mass ratio to 1:2, the pore size of the resulting

resin structure was reduced to 10-30 nm with a different morphology (Fig. 5.2l). Similar pore size reduction effects were observed for the ISO-38-R and ISO-69-R hybrid systems with lower BCP to resol mass ratios (Fig. S5.3). Keeping ISO-38 to resol mass ratio constant at 3:1, we increased the hybrid film thickness from ~500 nm (6 wt%) to ~1.0 μm and ~1.6 μm by increasing the mixed solution concentrations (10 and 12.5 wt%, respectively). Fig. 5.2m and n show thicker hierarchical porous resin structures with pore sizes of 50-400 nm and 50-600 nm for 10 wt% and 12.5 wt% ISO-38-R samples, respectively. Clearly the unique combination of BCP-directed self-assembly with transient thermal annealing allows tuning of film morphology, pore size and porosity of the 3D continuous network structure. We note the ~1.6 μm thick ISO-38-R hybrid sample set the empirical critical film thickness for the B-WRITE method, *i.e.*, the thicker hybrid film strongly absorbs the CO_2 laser photons.

The excellent material properties of transient-heated porous resin structure permit further heat and chemical processing. Fig. 5.3a shows a majority blue-colored ISO-69-R-CN sample containing seven brown-colored laser-irradiated lines with varying widths (150-1,000 μm) formed by the B-WRITE method, followed by heating to 450 °C in nitrogen for 1 h. Profilometry (Fig. 5.3b) and SEM (Fig. 5.3c) of laser-irradiated lines confirmed the transient-heated crosslinked resin mostly retained the thickness and porosity after the subsequent conventional heat treatment. We found the B-WRITE method can be further simplified by applying CO_2 laser-induced transient heating on as-deposited ISO-resol hybrid samples (with no thermal curing). For the as-deposited ISO-69-R hybrid samples, CO_2 laser irradiations were increased to 40 passes of 10-30 W laser powers to crosslink the resol oligomers and inhibit thermocapillary dewetting[26]. Fig. 5.3d and f display the nanoporous resin line patterns after laser-induced transient heating and removal of non-irradiated ISO-69 terpolymer and resol oligomers by rinsing

in THF. We further adjusted the macroscopic line dimensions by ablating the resin material directly with a 30 W laser power (25 ms dwell) to form nanoporous resin lines with highly straight edges (see SEM in Fig. 5.2j and profilometry profile in Fig. 5.3e). We note only 20 passes of sequential laser powers (10-30 W) were required for the as-deposited ISO-38-R hybrid samples, attributed to the elastomeric nature of majority PI block.

Raman spectroscopy on ISO-69-R-BW nanoporous resin structure indicates negligible graphitic carbon was formed by the B-WRITE method (Fig. 5.3g). Pyrolysis heat treatment at higher temperatures led to carbonization of phenolic resin at 600 °C with the D- and G-band centered at approximately 1326 and 1596 cm^{-1}, respectively; carbonization at 800 °C led to the narrowing and shifting of the D- and G-bands to 1312 and 1598 cm^{-1}, respectively, suggesting a higher degree of graphitization[22,23]. Cross-sectional SEM in Fig. 5.3i reveal the ISO-69-R-BW nanoporous carbon sample contracted by 50-60% in the out-of-plane direction during carbonization at 800 °C. We performed four-point probe measurements on carbonized ISO-69-R-BW samples on Si substrates with a ~100 nm SiO_2 overlayer. Applying linear fit to the current/voltage curves, the electrical conductance of ISO-69-R-BW nanoporous carbon sample heated at 600 °C was ~0.05 mS (Fig. S5.4a). At 800 °C, the conductance improved to 4.38 mS, giving a sheet resistance of 144.8 Ω/□ (Fig. 5.3h). Even with the high porosity, the conductance of ISO-69-R-BW nanoporous carbon sample was slightly lower than that of the dense carbonized resin film (13.0 mS) heated under identical conditions at 800 °C (Fig. S5.4b).

As a proof of concept experiment, we fabricated a microfluidic device that connect multiple length scales to demonstrate the versatility of hierarchical structure formation with the B-WRITE method. First, a trench was written into a cured resol film on Si with

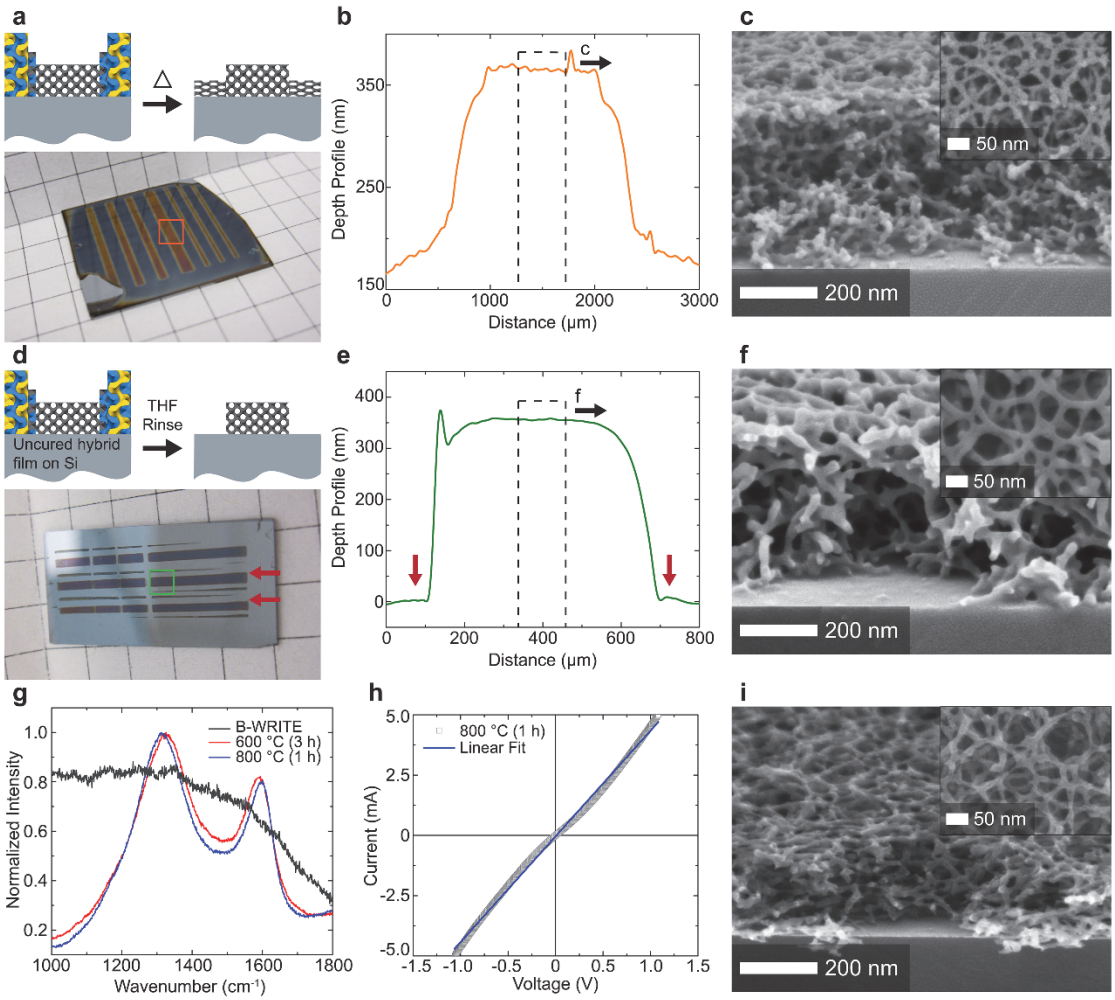

Figure 5.3. Grating pattern inversion and carbonization of ISO-69-R-BW nanoporous resin films. a-f, Optical (a and d), profilometry profile (b and e), cross-sectional and plan view (inset) SEM (c and f) images of pattern inversion by furnace calcination at 450 °C in nitrogen (a-c) and THF rinsing (d-f). The grid paper has 5 mm markings. Profilometry measurements were performed in the colored box regions of (a) and (d). Representative cross-sectional SEM were taken in the dotted box regions shown in (b) and (e). Red arrows in (d) and (e) indicate straight line edges of the resin network structure formed by a single CO_2 laser irradiation pass at 30 W of 25 ms. g, Raman spectroscopy of ISO-69-R-BW samples as prepared by B-WRITE method (grey curve), and carbonized at 600 °C (red curve) and 800 °C (blue curve) in nitrogen. h-i, Current-voltage plot (h) and cross-sectional and plan view (inset) SEM micrographs (i) of ISO-69-R-BW nanoporous samples carbonized at 800 °C in nitrogen.

a 30 W laser power (25 ms dwell), followed by depositing a 6 wt% ISO-38-R hybrid film on the trench and resol film as an overlayer. We then applied the B-WRITE method to form the ISO-38-R-BW nanoporous resin network structure in the trench and sealed with a polydimethylsiloxane film (Fig. 5.4a). From profilometry and SEM (Fig. S5.5), the B-WRITE microfluidic device channel was about 13 mm in length (port-to-port), 630 μm in width and 1.4 μm in thickness, containing a ~200 nm thick ISO-38-R-BW nanoporous resin network structure in the channel to provide additional surface areas that may be desirable for microfluidic sensing and catalysis applications[31]. The bright field and fluorescence optical micrographs in Fig. 5.4b and c confirmed dimethyl sulfoxide containing 2.82 mM tetramethylrhodamine (TRITC) dye flowed through the B-WRITE microfluidic channel using a pressure-controlled pump. For more complex structure formation, we combined photolithography, ISO-resol co-assembly and laser-induced transient heating techniques together. Fig. 5.4d displays the top overview of the ISO-69-R hybrid sample deposited on a patterned Si substrate prepared by photolithography and transformed to nanoporous resin network structure by the B-WRITE method. Cross-sectional SEM in Fig. 5.4e-g show conformal adhesion of the nanoporous resin film to the curved Si surfaces, demonstrating the compatibility of the B-WRITE method with established semiconductor processing technologies.

Finally, we employed the nanoporous resin structure as template for an all-laser-induced organic-inorganic nanostructure fabrication method. We applied the B-WRITE method to form an ISO-69-R-BW nanoporous resin network structure and heated in nitrogen at 400 °C to enhance adhesion, followed by backfilling with amorphous Si by chemical vapor deposition (CVD)[32]. The resin/a-Si core-shell composite sample was irradiated with a single 40 ns XeCl excimer laser pulse at 550 mJ/cm^2 to induce transient melt-crystallization of amorphous precursor into polycrystalline Si[19], verified by 2D X-

ray diffraction and Raman spectroscopy (Fig. S5.6). SEM images in Fig. 5.4h-j display the resulting nanoporous polycrystalline silicon nanostructures after CF_4 reactive ion etching, piranha solution and hydrofluoric acid (HF) treatments, confirming successful pattern transfer via BCP organic templating. Remarkably, the organic resin template not only permit amorphous silicon CVD directly at 350 °C[32], it even withstood the transient melt-crystallization of Si at 1414 °C. In analogy to the single crystal epitaxial nanostructure results[19], organic BCP pattern transfer by laser annealing could be enhanced, for example, applying thermal/solvent annealing on as-deposited BCP-resol hybrid thin films to form ordered morphologies, and complete removal of native SiO_2 layer in diluted HF using the inert resin template.

The synergetic coupling of BCP-directed self-assembly with CO_2 laser-induced transient heating has multiple advantages, including: (1) BCP-directed resol self-assembly provides direct access to 3D continuous network structure formation and pore size control; (2) a deterministic direct pattern transfer by the CO_2 laser; (3) enhanced materials properties that permit further processing for new functionalities and applications. This facile and scalable methodology may be used to create novel arbitrary-shaped miniaturized devices that require high surface areas and connectivity, spanning from micro-batteries and electrochemical capacitors to microfluidic sensors and catalytic reactors[3,20,21,31].

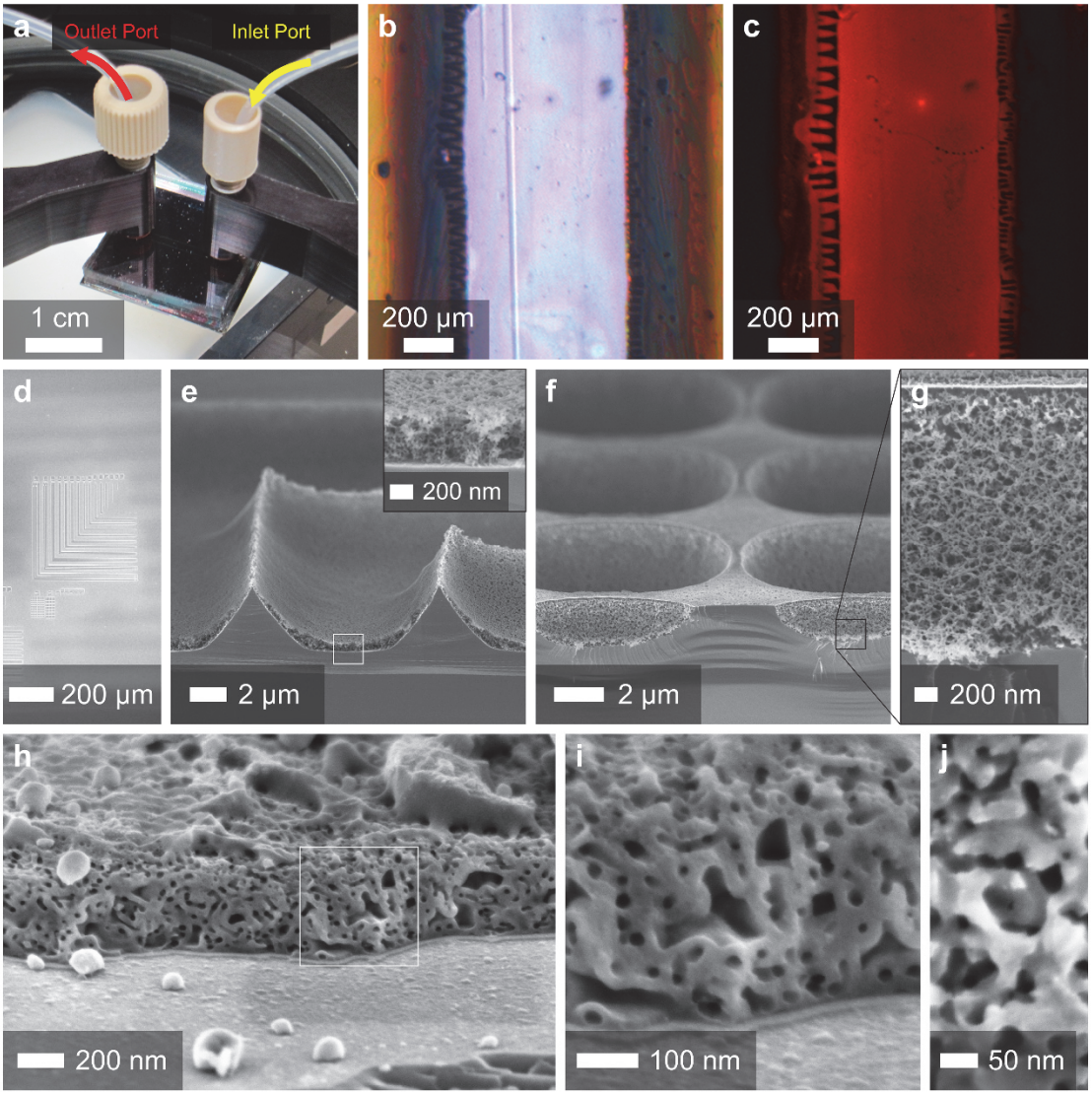

Figure 5.4. Hierarchical porous resin structure formation and pattern transfer. a, Optical micrograph of the resol-based microfluidic device fabricated by the B-WRITE method on the probe station. b and c, Bright-field (b) and fluorescence (c) optical micrographs of dimethyl sulfoxide with TRITC dye in the microfluidic channel. d-g, Plan view (d) and cross-sectional (e-g) SEM micrographs of hierarchical porous resin structure formation coupling photolithography, ISO-resol co-assembly and B-WRITE method. Inset in (e) shows the white boxed cross-section in higher magnification. h, Cross-sectional SEM micrograph of nanoporous polycrystalline Si nanostructures formed by organic templating using an all-laser nanostructure fabrication approach. i and j, Higher resolution cross-sectional (i) and plan view (h) SEM micrographs of the laser-induced polycrystalline Si nanostructure in (h).

Methods

Materials. Synthesis of ISO terpolymers by sequential anionic polymerizationm, resorcinol-formaldehyde resol oligomers and phenol-formaldehyde resol oligomers were reported elsewhere[23]. Anhydrous tetrahydrofuran and Pluronic F127 were obtained from Sigma Aldrich. Absolute ethanol (200 proof), sulfuric acid (97%) and hydrogen peroxide (30%) were obtained from Koptec, Fisher Chemical and Macron Fine Chemicals, respectively. 0.01-0.02 Ω.cm boron-doped Si substrates (4P0.01-.02SSP-INV) were obtained from WRS Materials. Sylgard 184 silicone elastomer kit was obtained from Dow Corning.

Block Copolymer-Directed Resol Hybrid Thin Film Synthesis. Si substrates were treated in piranha solution (sulfuric acid/hydrogen peroxide = 3:1, v/v) and rinsed profusely in deionized water before use. All organic thin film samples were deposited on Si by spin-coating at 2000 rpm for 45 s in a nitrogen drybox. ISO-directed resol hybrid thin films (Table S5.1) were prepared by mixing the ISO terpolymers with resorcinol-formaldehyde resols in tetrahydrofuran for 1 h prior to deposition on Si[23]. 20 wt% F127-directed resol hybrid thin films (Table S5.1) were prepared by mixing F127 BCP surfactant with phenol-formaldehyde resols in ethanol for 2 h prior to deposition on Si[22,23]. Unless noted otherwise, the hybrid samples were cured in a vacuum oven at 100 °C overnight (>12 h).

Block Copolymer Based Writing Induced by Transient Heating Experiments (B-WRITE) Method. The CO_2 laser-induced transient heating setup is described elsewhere[24]. The transient temperature of Si substrate during laser irradiation is determined by the laser power and dwell time. The scan type may be a unidirectional single pass (in the lateral x direction), bidirectional multiple pass (non-overlapping), or bidirectional multiple pass with overlap of 55 μm scan step (in the transverse y

direction), to cover the irradiated area. The irradiated area is approximately rectangular, having a width *w* defined by the full-width-half-maximum of the laser intensity profile (x direction), and length *l* defined by the substrate dimension (y direction). To prevent thermocapillary dewetting effects during transient heating, the irradiated width *w* is approximately 40% wider for the sequential 10-35 W laser powers (*e.g.,* $w = 0.7$ mm) than the final 40 W laser power (*e.g.*, $w = 0.5$ mm). Unless noted otherwise, the CO_2 laser-induced transient heating dwell is 0.5 ms.

Transient Resol Thermopolymerization. (1) All cured BCP-resol hybrid samples were irradiated with 20 passes (overlap) laser powers at 10 W, 20 W, 30 W, and 10 passes (overlap) at 35 W, sequentially. (2) The as-deposited ISO-38-R hybrid samples were irradiated with 20 passes (overlap) laser powers at 10 W, 20 W, 30 W, and 10 passes (overlap) at 35 W, sequentially. (3) The as-deposited ISO-69-R hybrid samples were irradiated with 40 passes (overlap) laser powers at 10 W, 20 W, 30 W, and 10 passes (overlap) at 35 W, sequentially.

Transient BCP Decomposition. For trenches with <150 μm width, the samples were irradiated with 10 passes (non-overlap) at 40 W. For trenches with >150 μm width, the samples were irradiated with 5 passes (overlap) at 40 W.

Furnace Heat Treatment. For calcination in air, the organic samples were slowly heated in a tube furnace at 1 °C/min rate to the respective temperature of 150, 225, 300, 275 and 450 °C, and held at the final temperature for 1 h. For calcination in nitrogen, the organic samples were slowly heated in a tube furnace at 1 °C/min rate to the respective temperature of 150, 300, 450 and 600 °C, and held at the final temperature for at least 1 h (3 h at 600 °C).

Electrical Conductivity Measurements. The 6 wt% ISO-69-R hybrid samples

(ISO/resol = 2.4:1, w/w) were deposited on Si with a thermally grown ~100 nm thick SiO_2 overlayer by spin-coating. ISO-69-R-BW nanoporous resin samples were prepared using as-deposited samples by the B-WRITE method as described above, followed by rinsing in THF to remove non-irradiated BCP and resol components. For carbonization, the samples were heated in nitrogen at 1 °C/min rate and held at 600 °C for 3 h, and/or raised to 800 °C for 1 h at 5 °C/min rate. Current/voltage data were collected using a Cascade Microtech CPS-05 four-point probe station with a Keithley 2400 source meter. From optical microscopy and SEM, the dimensions of the ISO-69-R-BW nanoporous carbon sample heated at 800 °C were w = 634 μm in width and t = 92 nm in thickness. The sheet resistance was calculated using $R_{sheet} = (V/I) \times (w/s)$, where w is the line width and s is the inter-probe spacing (1 mm)[33].

A 20 wt% resorcinol-formaldehyde resol solution was spin-coated on the SiO_2/Si substrate and cured in a vacuum oven at 100 °C overnight (>12 h). From profilometry, the dense film thickness was approximately 660 nm after carbonization at 800 °C for 1 h in nitrogen.

Resol-Based Microfluidic Device Fabrication by B-WRITE Method. 20 wt% resorcinol-formaldehyde resol solution was spin-coated on Si at 2000 rpm for 60 s to form a dense resol film, followed by curing in a vacuum oven at 100 °C overnight (>12 h). The trench (channel) was formed with a single pass of CO_2 laser irradiation at 30 W of 25 m dwell (175 μm scan step). A 6 wt% ISO-38-R hybrid thin film (ISO/resol = 3:1, w/w) was spin-coated on the trench and resol film as an overlayer and cured in a vacuum oven at 100 °C overnight (>12 h). The ISO-38-R-BW nanoporous resin structure was formed in the trench by the B-WRITE method as described above. A (3-aminopropyl)-trimethoxysilane (APTMS) surface coating was deposited on the sample by vapor deposition using the Applied MicroStructures MVD100 tool, followed by heating in an

oven at 80 °C for at least 1 h. A ~2 mm thick PDMS film was prepared by mixing the Sylgard 184 monomer and curing agent at 10:1 mass ratio in a petri dish, degassed in a vacuum desiccator and cured at 60 °C for 4 h. Holes were punched in the PDMS film for the inlet and outlet ports. Finally, the APTMS surface-functionalized sample and PDMS were exposed to an oxygen plasma (50 W, Harrick Plasma) for 30-40 s and placed in conformal contact at room temperature for >1 h. The microfluidic device flow experiment was conducted on the CorSolutions microfluidic probe station with a PV-1500 packing vessel pump delivering a pulse-free flow of 2.82 mM TRITC dye dissolved in dimethyl sulfoxide into the channel with 10-20 psi dry nitrogen.

Photolithography Patterning of Si Substrates. A thin layer of P-20 primer (20 % hexamethyldisilazane in propylene glycol monomethyl ether acetate) was spin-coated on Si at 4000 rpm for 30 s to promote photoresist adhesion. A ~1.3 μm thick positive-tone Shipley 1813 photoresist was spin-coated on the primed Si surface at 4000 rpm for 30 s and (soft) baked at 90 °C for 60 s. The resist was exposed with a 365 nm UV irradiation at a dose of 34.5 mJ/cm^2 using the Karl Suss MA6 tool. The exposed sample was (hard) baked at 90 °C for 60 s, followed by development in 0.26 N tetramethylammonium hydroxide (TMAH) solution and subsequent deionized water rinse and nitrogen blow drying. The substrate was subjected to SF_6 reactive ion etching (RIE) for 140 s (30 sccm, 200 mTorr, 200 W) to form Si trenches using the Oxford PlasmaLab 80+ RIE System. Finally, the remaining photoresist was stripped by oxygen plasma using the Gasonics Aura 1000 tool.

The 6 wt% ISO-69-R hybrid thin film samples (ISO/resol = 2.4:1, w/w) were spin-coated on the photolithography patterned Si substrates and cured in a vacuum oven at 100 °C overnight (>12 h). The ISO-69-R-BW nanoporous resin thin film was formed in the Si trenches by the B-WRITE method as described above.

Laser-Melt-Induced Polycrystalline Si Nanostructure Fabrication. The 6 wt% ISO-69-R-BW resin structure was prepared by the B-WRITE method using as-deposited ISO-69-R hybrid sample (ISO/resol = 2.4:1, w/w) as described above and further heated in nitrogen at 400 °C for 1 h with a ramp rate of 1 °C/min to improve adhesion to the Si substrate. Amorphous silicon was deposited in the porous organic template by static chemical vapor deposition using disilane as precusor at 350 °C for 3 h[32]. A single pulse of 40 ns FWHM XeCl excimer laser (λ = 308 nm) at 550 mJ/cm^2 was used to melt-crystallize the amorphous Si in a homebuilt vacuum chamber (<1 Torr) with a UV-transparent quartz window[19]. The excimer laser-irradiated sample was treated in CF_4 RIE for 15 s (30 sccm, 40 mTorr, 150 W) to remove the Si overlayer, hot piranha solution for 3 h (sulfuric acid/hydrogen peroxide, 3:1 v/v, 75 °C) to remove the organic template, and 49% hydrofluoric acid for 10-20 s to remove the SiO_2 layer.

Characterization. SEM images were acquired on Au-Pd coated organic thin film samples using a LEO 1550 SEM equipped with an in-lens detectors. FFT analysis was performed on plan view SEM micrographs in the ImageJ software using a Radial Profile Extended plugin script written by Philippe Carl[7]. Profilometery measurements were acquired using a Tencor P-10 profilometer and smoothened with a FFT filter function in the GenPlot software. Organic thin film and nanoporous resin structure thickness were measured using SEM and profilometer. FTIR data were acquired using a Bruker Hyperion FTIR microscope in the attenuated total reflectance and specular reflectance modes. The baseline subtraction function was applied using the OriginPro 9.1 software. Raman spectroscopy measurements were conducted using a Renishaw InVia confocal Raman microscope with the 785 nm and 488 nm excitation laser sources for the carbonized ISO-69-R-BW samples and silicon samples, respectively. Optical microscopy images were acquired using an Olympus BX51 microscope (upright

fluorescence microscope) equipped with a mercury lamp source and a Chroma 41002B (605/75) fluorescence filter. 2D X-ray diffraction measurement was performed on a Bruker General Area Detector Diffraction System (GADDS) equipped with a Bruker HI-STAR area detector using Cu Kα radiation (40 kV, 40 mA, λ = 0.15418 nm). Thermogravimetric analysis (TGA) was conducted using a Seiko Exstar TG/DTA 6200 thermal analyser at a heating rate of 5 °C/min in helium.

Acknowledgment

This work was supported by the National Science Foundation (NSF) Single Investigator Award (DMR-1409105). K.W.T. gratefully acknowledges the Singapore Energy Innovation Programme Office for a National Research Foundation graduate fellowship. This work made use of research facilities at the Cornell Center for Materials Research (CCMR) with support from the NSF Materials Research Science and Engineering Centers (MRSEC) program (DMR-1120296); Cornell NanoScale Science & Technology Facility (CNF), a member of the National Nanotechnology Infrastructure Network, which is supported by the National Science Foundation (Grant ECCS-0335765); Nanobiotechnology Center shared research facilities at Cornell University; and KAUST-Cornell Center for Energy and Sustainability supported by Award No. KUS-C1-018-02, made by King Abdullah University of Science and Technology (KAUST). The authors gratefully acknowledge experimental assistance from: P. Carubia and T. Yuasa for ATR-FTIR spectroscopy measurements; D. Lynch for electrical conductivity measurements; Y. Sun, Q. Zhang and T. Corso (CorSolutions LLC) for microfluidic device fabrication and probe station setup; M. Goodman and Prof. P. Braun (University of Illinois at Urbana Champaign) for amorphous silicon chemical vapor deposition. We also thank Prof. L. Estroff, T. Porri, M. Weathers, Y. Gu and H.

Sai for helpful discussions.

REFERENCES

1. Hemminger, J., Crabtree, G. & Sarrao, J. *From Quanta to the Continuum: Opportunities for Mesoscale Science*. (U.S. Department of Energy Basic Energy Sciences Advisory Committee Report, 2012). at <http://science.energy.gov/~/media/bes/pdf/reports/files/OFMS_rpt.pdf>

2. Service, R. F. The Next Big(ger) Thing. *Science* **335,** 1167–1167 (2012).

3. Davis, M. E. Ordered porous materials for emerging applications. *Nature* **417,** 813–821 (2002).

4. Kamperman, M. *et al.* Integrating Structure Control over Multiple Length Scales in Porous High Temperature Ceramics with Functional Platinum Nanoparticles. *Nano Lett.* **9,** 2756–2762 (2009).

5. Yang, P. *et al.* Hierarchically Ordered Oxides. *Science* **282,** 2244–2246 (1998).

6. Peinemann, K.-V., Abetz, V. & Simon, P. F. W. Asymmetric superstructure formed in a block copolymer via phase separation. *Nat. Mater.* **6,** 992–996 (2007).

7. Phillip, W. A. *et al.* Tuning Structure and Properties of Graded Triblock Terpolymer-Based Mesoporous and Hybrid Films. *Nano Lett.* **11,** 2892–2900 (2011).

8. Sai, H. *et al.* Hierarchical Porous Polymer Scaffolds from Block Copolymers. *Science* **341,** 530–534 (2013).

9. Dorin, R. M., Sai, H. & Wiesner, U. Hierarchically Porous Materials from Block Copolymers. *Chem. Mater.* **26,** 339–347 (2014).

10. Yanagisawa, T., Shimizu, T., Kuroda, K. & Kato, C. The Preparation of Alkyltriinethylaininonium–Kaneinite Complexes and Their Conversion to Microporous Materials. *Bull. Chem. Soc. Jpn.* **63,** 988–992 (1990).

11. Kresge, C. T., Leonowicz, M. E., Roth, W. J., Vartuli, J. C. & Beck, J. S. Ordered mesoporous molecular sieves synthesized by a liquid-crystal template mechanism. *Nature* **359,** 710–712 (1992).

12. Templin, M. *et al.* Organically Modified Aluminosilicate Mesostructures from Block Copolymer Phases. *Science* **278,** 1795–1798 (1997).

13. Zhao, D. *et al.* Triblock Copolymer Syntheses of Mesoporous Silica with Periodic 50 to 300 Angstrom Pores. *Science* **279,** 548–552 (1998).

14. Yang, P., Zhao, D., Margolese, D. I., Chmelka, B. F. & Stucky, G. D. Generalized syntheses of large-pore mesoporous metal oxides with semicrystalline frameworks. *Nature* **396,** 152–155 (1998).

15. Joo, S. H. *et al.* Ordered nanoporous arrays of carbon supporting high dispersions of platinum nanoparticles. *Nature* **412,** 169–172 (2001).

16. Malenfant, P. R. L., Wan, J., Taylor, S. T. & Manoharan, M. Self-assembly of an organic–inorganic block copolymer for nano-ordered ceramics. *Nat. Nanotechnol.* **2,** 43–46 (2007).

17. Lee, J. *et al.* Direct access to thermally stable and highly crystalline mesoporous transition-metal oxides with uniform pores. *Nat. Mater.* **7,** 222–228 (2008).

18. Warren, S. C. *et al.* Ordered Mesoporous Materials from Metal Nanoparticle–Block

Copolymer Self-Assembly. *Science* **320,** 1748–1752 (2008).

19. Arora, H. *et al.* Block Copolymer Self-Assembly–Directed Single-Crystal Homo- and Heteroepitaxial Nanostructures. *Science* **330,** 214–219 (2010).

20. Simon, P. & Gogotsi, Y. Materials for electrochemical capacitors. *Nat. Mater.* **7,** 845–854 (2008).

21. Orilall, M. C. & Wiesner, U. Block copolymer based composition and morphology control in nanostructured hybrid materials for energy conversion and storage: solar cells, batteries, and fuel cells. *Chem. Soc. Rev.* **40,** 520–535 (2011).

22. Meng, Y. *et al.* Ordered Mesoporous Polymers and Homologous Carbon Frameworks: Amphiphilic Surfactant Templating and Direct Transformation. *Angew. Chem. Int. Ed.* **44,** 7053–7059 (2005).

23. Werner, J. G., Hoheisel, T. N. & Wiesner, U. Synthesis and Characterization of Gyroidal Mesoporous Carbons and Carbon Monoliths with Tunable Ultralarge Pore Size. *ACS Nano* **8,** 731–743 (2014).

24. Jung, B. *et al.* Kinetic Rates of Thermal Transformations and Diffusion in Polymer Systems Measured during Sub-millisecond Laser-Induced Heating. *ACS Nano* **6,** 5830–5836 (2012).

25. Tang, J.-L. & Tsai, M.-A. Rapid formation of block copolymer thin film based on infrared laser irradiation. in *Conference on Lasers and Electro-Optics - Pacific Rim, 2007. CLEO/Pacific Rim 2007* 1–2 (2007). doi:10.1109/CLEOPR.2007.4391384

26. Singer, J. P. *et al.* Direct-Write Thermocapillary Dewetting of Polymer Thin Films by a Laser-Induced Thermal Gradient. *Adv. Mater.* **25,** 6100–6105 (2013).

27. Strong, V. *et al.* Direct Sub-Micrometer Patterning of Nanostructured Conducting Polymer Films via a Low-Energy Infrared Laser. *Nano Lett.* **11,** 3128–3135 (2011).

28. Silverstein, R. M., Bassler, G. C. & Morrill, T. C. *Spectrometric identification of organic compounds*. (Wiley, 1991).

29. Gao, W. *et al.* Direct laser writing of micro-supercapacitors on hydrated graphite oxide films. *Nat. Nanotechnol.* **6,** 496–500 (2011).

30. El-Kady, M. F., Strong, V., Dubin, S. & Kaner, R. B. Laser Scribing of High-Performance and Flexible Graphene-Based Electrochemical Capacitors. *Science* **335,** 1326–1330 (2012).

31. Elvira, K. S., i Solvas, X. C., Wootton, R. C. R. & deMello, A. J. The past, present and potential for microfluidic reactor technology in chemical synthesis. *Nat. Chem.* **5,** 905–915 (2013).

32. Rinne, S. A., García-Santamaría, F. & Braun, P. V. Embedded cavities and waveguides in three-dimensional silicon photonic crystals. *Nat. Photonics* **2,** 52–56 (2008).

33. Smits, F. Measurement of Sheet Resistivities with the 4-Point Probe. *AT&T Tech. J.* **37,** 711–718 (1958).

APPENDIX D

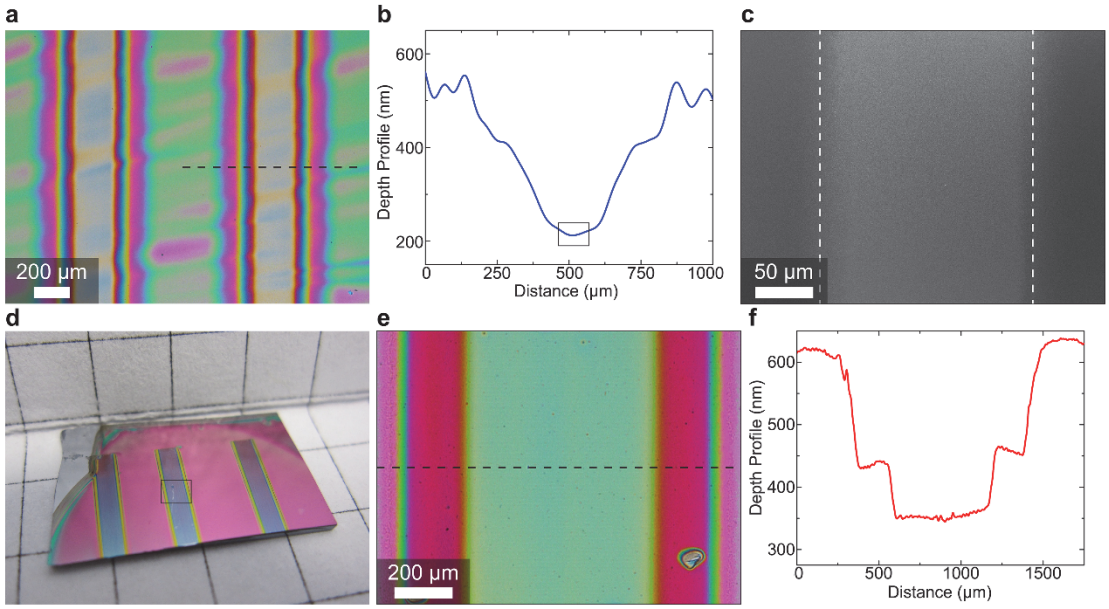

Figure S5.1. Characterization of nanoporous resin structures in ISO-resol hybrid thin films formed by B-WRITE method. a-c, Optical (a), profilometry (b), and plan view SEM (c) characterization of 6 wt% ISO-38-R-BW nanoporous resin trenches in the hybrid sample. The black box in (b) indicate the nanoporous resin trench region shown in the plan view SEM image in (c). The white dotted lines in (c) highlight the contrast difference formed by the CO_2 laser-induced transient heating. d-f, Optical (d and e) and profilometry (f) characterization of 6 wt% ISO-69-R-BW nanoporous trenches in the hybrid sample. The black box in (d) indicate the plan view optical image in higher magnification displayed in (e). The black dotted lines in the optical images (a and e) indicate the profilometry scan direction acquiring the corresponding cross-sectional profiles (b and f). The grid paper has 5 mm markings.

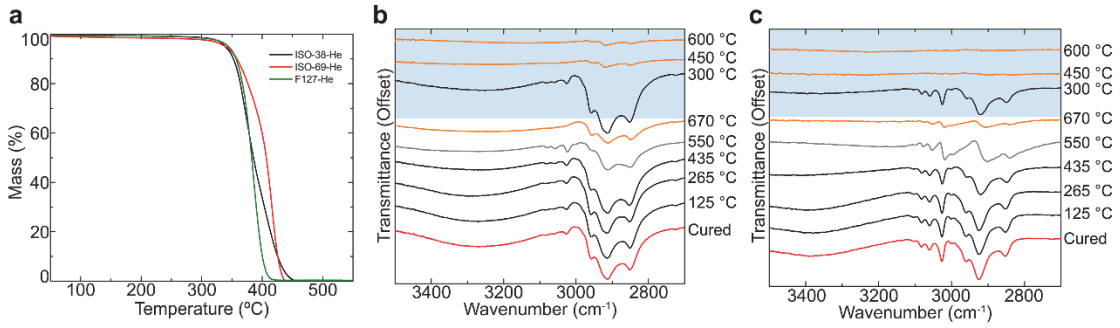

Figure S5.2. a, TGA plots of ISO-38, ISO-69 and F127 BCPs measured at a heating rate of 5 °C/min in helium. b and c, FTIR spectroscopy of cured ISO-38-R (b) and ISO-69-R (c) hybrid samples annealed by CO_2 laser-induced transient heating in air (white color-coded) and furnace calcination in nitrogen (blue color-coded) measured in ATR and specular reflectance modes, respectively, after baseline subtraction. The ISO-resol hybrid samples (red curves) display multiple intensity peaks in two wavenumber bands: hydroxyl stretching vibrations in 3200-3500 cm^{-1} band assigned to the hydrogen bonds and free phenolic hydroxyl group, and alkyl stretching vibrations in 2800-3000 cm^{-1} band assigned to the ISO terpolymers[33]. During CO_2 laser-induced transient heating (white color-coded), the hydroxyl peak started to decrease from ambient to 435 °C attributed to crosslinking of resols. The alkyl peaks of ISO terpolymers significantly diminished from 550-670 °C indicating ISO decomposition. The hydroxyl and alkyl stretching vibrational intensity peaks (blue color-coded) indicate the ISO-resol hybrid samples remained stable at 300 °C during calcination in nitrogen. All the peaks mostly vanished at 450 °C indicating decomposition of ISO terpolymers to form mesoporous resin structures.

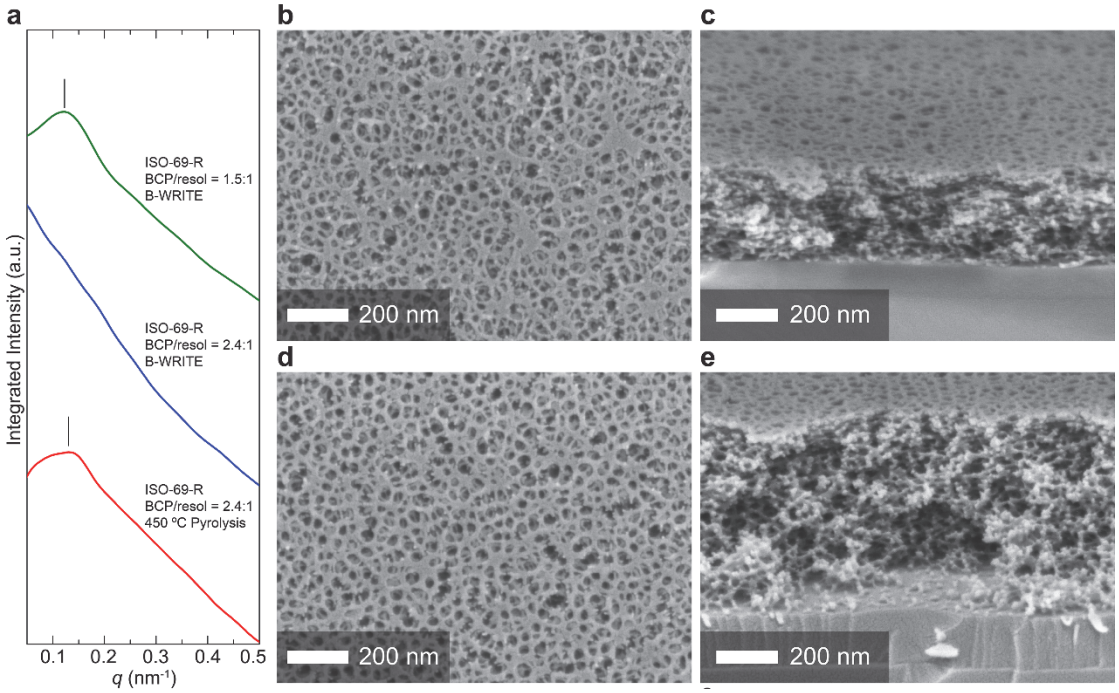

Figure S5.3. a, FFT analysis of plan view SEM images of ISO-69-R porous resin samples annealed by B-WRITE method and calcination in nitrogen as indicated, plotted again the scattering vector *q*. The ISO-69-R porous resin structure prepared by slow heating in nitrogen at 450 °C (red curve) has a macroscopically homogenous characteristic length scale of ~48.2 nm, whereas the porous resin sample prepared by the B-WRITE method in air (blue curve) is macroscopically inhomogeneous (ISO/resol = 2.4:1, w/w). The peak for the ISO-69-R porous resin structure with higher resol contents formed by B-WRITE method in air indicates a macroscopically homogenous characteristic length scale of ~51.2 nm (ISO/resol = 1.5:1, w/w). b to e, Plan view (b and d) and cross-sectional (c and e) SEM micrographs of ISO-38-R-BW and ISO-69-R-BW porous resin samples prepared by the B-WRITE method with ISO to resol mass ratio of 1.5:1, respectively.

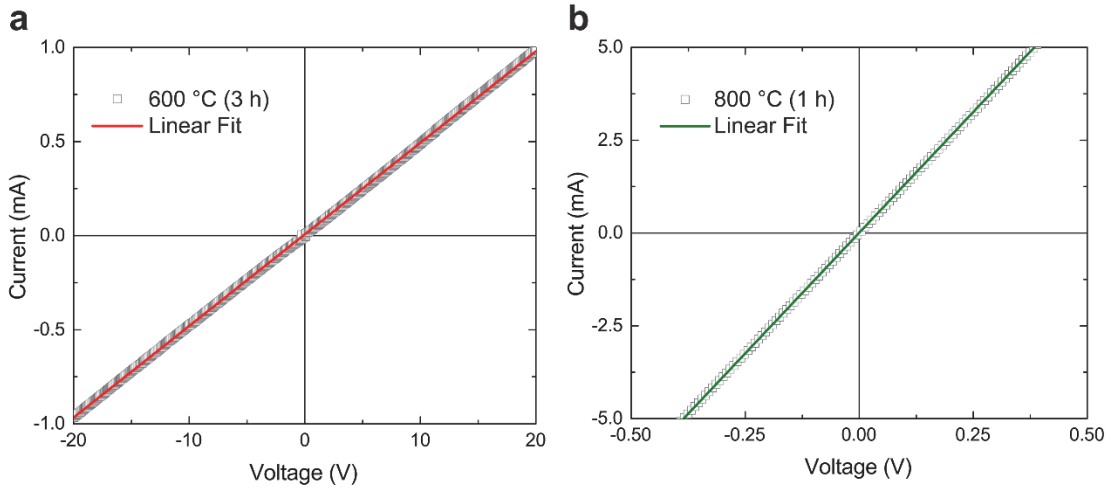

Figure S5.4. Current-voltage plots of carbonized ISO-69-R-BW nanoporous sample (a) and dense resol film (b) annealed at 600 °C for 3 h and 800 °C for 1 h in nitrogen, respectively.

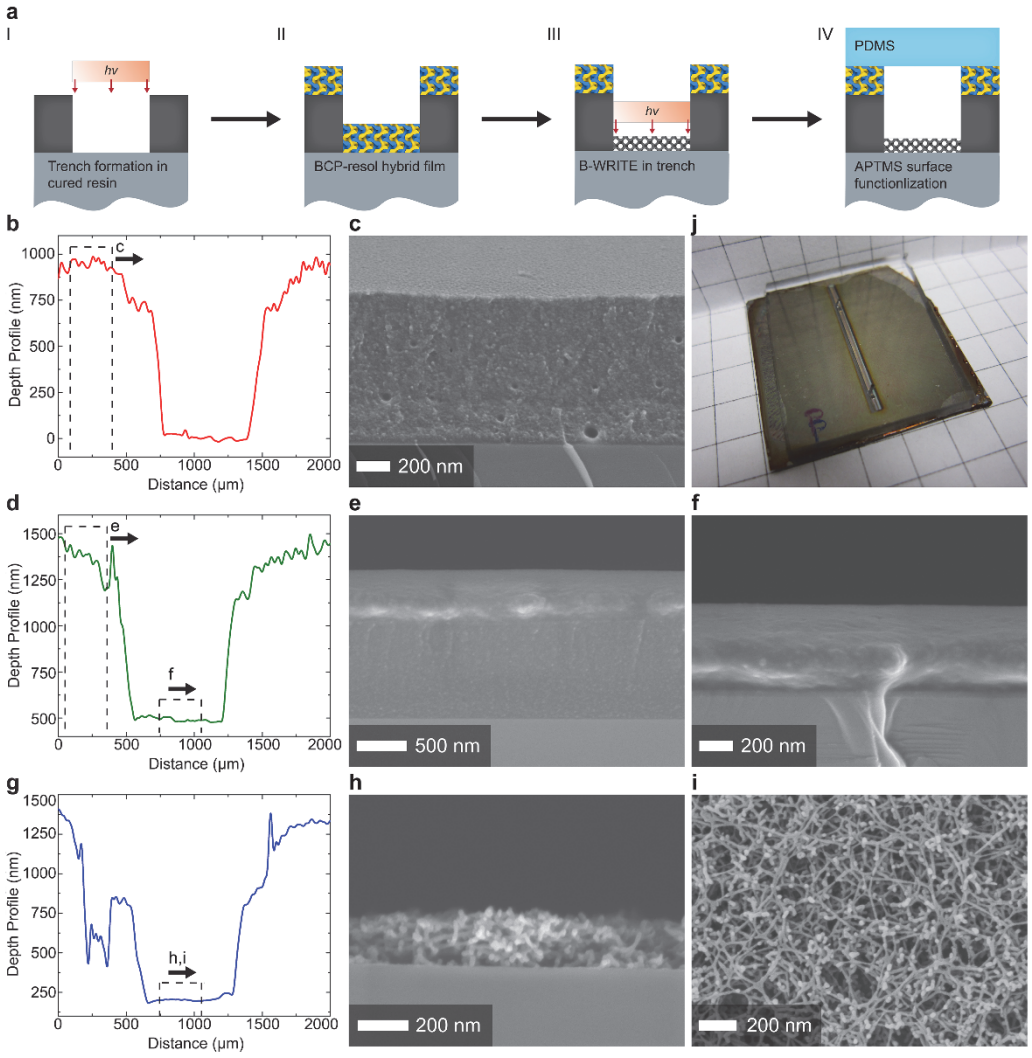

Figure S5.5. Fabrication of the resol-based microfluidic device by the B-WRITE method. a, Schematic repsentation. A 20 wt% resol solution was spin-coated on a Si substrate and cured at 100 °C. A trench was directly written into a cured resol film with a 30 W laser power (25 ms dwell) (Stage I). An ISO-38-R hybrid film was deposited on the trench and resol film as an overlayer and cured at 100 °C (Stage II). The nanoporous resol network structure was formed in the trench by the B-WRITE method (Stage III). The device was completed by sealing with a ~2 mm thick polydimethylsiloxane film after (3-aminopropyl)-trimethoxysilane surface functionalization (Stage IV). b and c, Profilometry profile and cross-sectional SEM micrographs at Stage I. d-f, Profilometry profile and cross-sectional SEM micrographs at Stage II. g-i, Profilometry profile and cross-sectional SEM micrographs at Stage III. j, Optical micrograph of the resol-based microfluidic device at Stage IV. The grid paper has 5 mm markings.

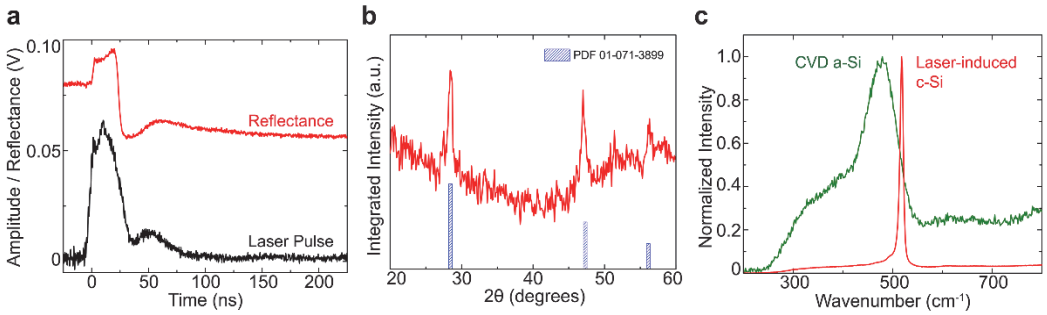

Figure S5.6. Characterization of all-laser-induced polycrystalline Si nanostructure fabrication by organic templating. a, The top red curve displays the time-resolved reflectance signal of the melt and crystallization of Si in ~50 ns using a 650 nm HeNe diode probe laser. The lower black curve indicates the incident excimer laser pulse profile. b, Integrated intensity plot of the X-ray diffraction pattern of pulsed excimer laser-induced polycrystalline Si sample (PDF 01-071-3899) after organic template removal. c, Raman spectroscopy of the amorphous Si overlayer in the organic template (green curve) and laser-induced polycrystalline Si sample after template removal (red curve). The shift of intensity peaks from ~479 cm^{-1} (green curve) and ~520 cm^{-1} (red curve) indicates the conversion of Si from amorphous to crystalline phase after pulse excimer laser annealing.

Table S5.1. Experimental parameters of organic thin film synthesis.

Organic Film	BCP/Resol Mass Ratio	Solution Concentration (Solvent)	Average Hybrid Film Thickness (nm)
ISO-38-R	3:1	6 wt% (Tetrahydrofuran)	503 ± 5
		10 wt% (Tetrahydrofuran)	1063 ± 7
		12.5 wt% (Tetrahydrofuran)	1606 ± 36
ISO-69-R	1.5:1	6 wt% (Tetrahydrofuran)	569 ± 3
	2.4:1	6 wt% (Tetrahydrofuran)	621 ± 13
F127-R	1.5:1	20 wt% (Ethanol)	656 ± 4
	1:1		875 ± 9
	1:2		661 ± 15
ISO-38		5 wt% (Tetrahydrofuran)	450 ± 9
ISO-69			471 ± 4
Resorcinol-Formaldehyde Resols		20 wt% (Tetrahydrofuran)	944 ± 3

CHAPTER 6

BLOCK COPOLYMER-DIRECTED ORGANIC TEMPLATING OF LASER-INDUCED CRYSTALLINE SILICON NANOSTRUCTURES

Abstract

Three-dimensional (3D) porous polycrystalline silicon network nanostructures are formed by coupling mesoporous block copolymer-directed organic resin template formation, backfilling of the pore network with amorphous Si and pulsed excimer laser irradiation. The mesoporous resin network structure remained highly stable above 1400 °C when heated below sub-millisecond time frames. Raman spectroscopy indicates the nanoporous resin network structure condenses into amorphous carbon phase during transient heating to support the melt and subsequent solidification of silicon, yielding 3D mesoporous crystalline silicon nanostructures. This pattern transfer route may represent a direct conversion pathway from ordered block copolymer nanostructures to functional materials such as crystalline silicon for potential hybrid photovoltaics, photonic, and energy storage applications.

Tan, K. W., Werner, J. G., Goodman, M. D., Jung, B., Sai, H., Kim, H. S., Braun, P. V, Thompson, M. O. & Wiesner, U. To be submitted for publication.

Introduction

Three-dimensional (3D) nanostructured materials are gaining increasing importance for use in current and emerging applications,[1–3] for example, microelectronics,[4] photonic crystals and metamaterials,[5–8] membrane separation,[9–11] and energy conversion and storage.[2,12–15] The inherent 3D nature of block copolymer (BCP) self-assembly provides a direct pathway to fabricate sub-100 nm structural features with well-defined ordered morphologies ranging from 1D lamellae, 2D hexagonal cylinders to 3D continuous network morphologies.[1,2,16,17] To further advance materials selection and functional properties, BCPs have been combined as structure directing agents with organic or inorganic additives as to form ordered porous structures with mesoscopic (2-50 nm) and higher length scale features.[10,15,18–34] This is often termed as the "soft" templating method. In the alternative "hard" templating approach, the porous organic/inorganic BCP structure is utilized as a pattern transfer scaffold for backfilling with the functional material, followed by etching to yield functional structures with the inverse morphology.[20,24,28,35] Mesoporous 3D continuous network morphologies are of particular interest for their high surface area, connectivity, pore accessibility and mechanical stability. For example, crystalline titania nanostructures with bicontinuous gyroidal morphologies have been synthesized by soft and hard BCP templating methods for use in hybrid photovoltaic devices.[12,13] The titania gyroidal electrodes facilitate backfilling of the hole transport material through the interconnected pore network and enable continuous connectivity of the titania struts for enhanced electron collection and transport.[12,13] Moreover, it is desirable to construct a mesoporous BCP gyroid structure with high refractive index contrast to harness photonic properties of the chiral continuous network, *e.g.*, an alternating gyroidal mesoporous silicon (Si) nanostructure.[5] These Si network structures with 3D

connectivity and high surface area may also be of interest for hybrid photovoltaics,[2,12,13,15,36] energy storage[14,37] and sensors[38].

We have previously demonstrated the generation of 3D single-crystal Si and NiSi nanostructures connected epitaxially to the Si substrate by combining BCP-directed aluminosilicate/niobia hard templating with pulsed excimer laser annealing.[35] The critical step to achieve single-crystal epitaxy was to ensure a clean interface between the amorphous overlayer and Si substrate. However, we have not yet identify an ideal template material: (1) BCP-directed inorganic hybrid systems are typically kinetically trapped in non-equilibrium morphologies after spin-coating due to rapid sol-gel condensation reactions, enhanced solvent evaporation during spin-coating and interfacial energy contributions;[1,17,35] (2) chemical inertness and/or high selective etch resistance relative to SiO_2 is required for complete native oxide removal; (3) excellent template stability is necessary during the transient melt-crystallization process for high pattern transfer fidelity. We postulate here that a mesoporous BCP-directed all-organic hybrid system may be able to fulfill all of the above requirements. Firstly, BCP thin films with well-ordered periodic morphologies can be achieved after deposition by many different methods, such as thermal/solvent annealing and/or graphoepitaxy.[1,17,25] Secondly, many organic systems have high resistance to SiO_2 etchants (*e.g.*, hydrofluoric acid). Thirdly, thermal stability of polymers is greatly enhanced by applying very short transient heating.[39] Here we describe the first example for coupling mesoporous BCP-directed organic template formation, backfilling with amorphous Si (a-Si), and transient laser annealing to generate 3D porous crystalline Si (c-Si) network structures.

The process is shown schematically in Figure 6.1a-c. We deposited an all-organic hybrid thin film on a Si substrate employing a polyisoprene-*block*-polystyrene-*block*-

polyethylene oxide (ISO) triblock terpolymer to structure-direct resorcinol-formaldehyde resol oligomer additives.[26] After curing at 100 °C, the hybrid samples were pyrolysed at 450 °C in nitrogen. During pyrolysis, the cured resols crosslinked into phenolic resins while the ISO terpolymer decomposed, yielding mesoporous BCP-directed resin thin films with network structure (Figure 6.1a).[22,26] Mesoporous resin thin films of different thicknesses were obtained by varying the BCP-resol solution concentrations as shown in the scanning electron microscopy (SEM) images (Figure 6.1d,g,j). After immersing the mesoporous resin template in 0.5% hydrofluoric (HF) acid solution for ~2 min to remove native oxide on the Si substrate, we immediately loaded the sample into the chemical vapor deposition (CVD) chamber for a-Si deposition at 350 °C (Figure 6.1b).[6] SEM micrographs in Figure 6.1e,h,k show the near-complete backfilling of a-Si in the mesoporous resin templates with a 60-90 nm thick dense overlayer. The resin/a-Si composite nanostructure was then irradiated with a single 40 ns full-width-half-maximum 308 nm wavelength pulsed XeCl excimer laser at 700 mJ cm^{-2} energy fluence, with the ultraviolet photons mostly absorbed by the Si material to melt the a-Si precursor that subsequently solidified into c-Si within 50 ns (Figure S6.1, Appendix E).[35] Finally, the template was removed by CF_4 reactive ion etching (RIE), hot piranha solution and concentrated HF acid solution treatments to obtain the resulting porous inverse c-Si nanostructures (Figure 6.1c,f,i,l and S6.2).

Plan view and cross-sectional SEM micrographs in Figure 6.1d,g,j show mesoporous resin thin films of about 100, 200 and 400 nm thickness after pyrolysis, respectively, with interconnected pores in both in-plane and out-of-plane directions. From SEM and grazing incidence X-ray scattering (GISAXS), the average pore diameter is ~39.5 ± 9.3 nm with a macroscopically homogeneous characteristic length

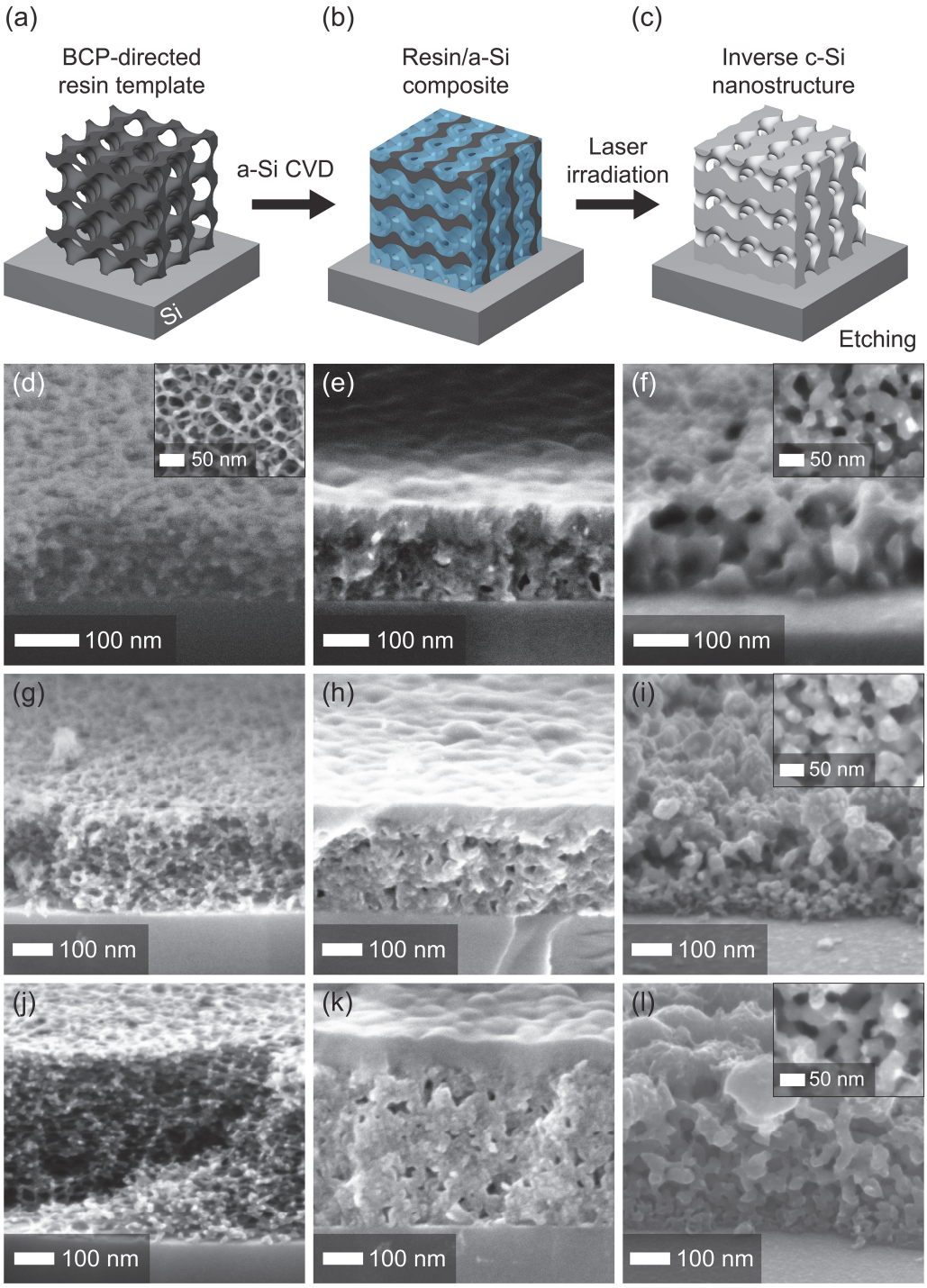

Figure 6.1. Schematic illustration, as well as, cross-sectional and plan view (insets) SEM micrographs of (a,d,g,j) mesoporous BCP-directed resin templates after pyrolysis; (b,e,h,k) a-Si deposition into organic template by CVD followed by pulsed laser irradiation; (c,f,i,l) resulting porous inverse c-Si nanostructures after template removal.

scale of $2\pi/q_{xy} \approx 43.9$ nm in the in-plane direction (Figure 6.2a),[15,31,32] where $q = 4\pi \sin\theta/\lambda$, θ is half of the total scattering angle, and λ is the X-ray wavelength ($\lambda = 1.18$ Å). The highly crosslinked resin exhibited remarkable materials properties throughout the hard templating and transient laser annealing processes. First the chemically inert organic template remained highly stable during the ~2 min immersion in 0.5% HF acid solution with no observable film delamination. We further note that a-Si CVD was performed directly on the thermally stable organic template at 350 °C without requiring an additional inorganic material backfilling process.[6] After pulsed excimer laser irradiation and template removal, SEM in Figure 6.1f,i,l and S6.2 show that the resulting porous inverse c-Si nanostructures were approximately 100-400 nm thick, respectively. Closer examination at higher magnifications revealed characteristic mesoscopic length scale features of the interconnected Si struts and pores. Figure 6.2b shows the GISAXS profile of a 350-400 nm thick inverse c-Si network structure with two diffuse diffraction peaks around $q = \pm 0.140$ nm^{-1}. From the integrated intensity GISAXS curves in Figure 6.2c, the proximity of the scattering peaks around $q = 0.143$ nm^{-1} (dotted line) suggests a moderate degree of pattern transfer fidelity from the mesoporous resin template to laser-induced mesoporous c-Si structures. This indicates that the organic template maintained excellent structural integrity during the transient melt-recrystallization of silicon at 1414 °C (vide infra). We note that despite immersing the organic template in 0.5% HF acid solution for ~2 min prior to a-Si CVD, the resulting laser-induced Si network nanostructures was unexpectedly polycrystalline, *i.e.*, the laser-induced Si crystal orientation was not directed epitaxially by the substrate during transient melt-solidification process (Figure S6.1b).[35] The cause is currently unknown; as the CVD chamber lacks a load-lock mechanism, we speculate that a new native SiO_2 layer may have regrown on the Si substrate due to small amounts of oxygen or moisture remaining after chamber evacuation prior to a-Si deposition.[6]

In order to understand the organic template behavior thermally annealed by transient heating, we irradiated the ~200 nm thick mesoporous resin templates with a 10.6 μm wavelength CO_2 laser on sub-millisecond time frames. The mesoporous resin template is transparent to the CO_2 laser (below a critical thickness) with Si absorbing the laser irradiation and converting into thermal energy to heat the surface, subsequently cooled by thermal conduction at the respective dwell time frames.[39] Figure 6.3a and S6.3a show the plots of the mesoporous resin template remaining thickness after a single CO_2 laser irradiation as a function of laser power and corresponding annealing temperature[39,40] on 0.05, 0.2, 0.5 and 2 ms dwells, respectively. Looking at Figure 6.3a the first clear observation is that thermal stability of mesoporous organic template increased as dwell duration was reduced over nearly two orders of magnitude on the sub-millisecond time frame. Notably the organic film thickness remained unchanged up to 1320 °C (92 W) of 0.05 ms dwell. Around the melting temperature of Si (1414 °C), mesoporous resin film thickness decreased by about 20% (75 W of 0.2 ms), 40% (62 W of 0.5 ms) and 90% (48 W of 2 ms) heated on increasing dwell time frames. Despite the decrease of film thickness with increasing laser powers, representative SEM images of 0.2 and 2 ms dwells in Figure 6.3b confirm that the laser irradiated samples retained their mesoporous network film morphology. From these SEM measurements, the resin network strut width (9.1 ± 1.7 nm) decreased by approximately 10% and 14% at 90 W (0.2 ms dwell) and 44 W (2 ms dwell), respectively. We performed Raman spectroscopy on CO_2 laser-irradiated samples of 0.2 and 2 ms dwells to investigate the associated chemical changes by transient heating (Figure S6.3b,c). Prior to CO_2 laser irradiation (0 W), broad D and G bands were detected for mesoporous resin templates pyrolysed at 450 °C around 1340 and 1560 cm^{-1}, respectively. The bands shifted and became narrower as laser powers increased, suggesting laser-induced condensation of the phenolic networks by transient heating.[22,26] The Raman spectra of samples irradiated

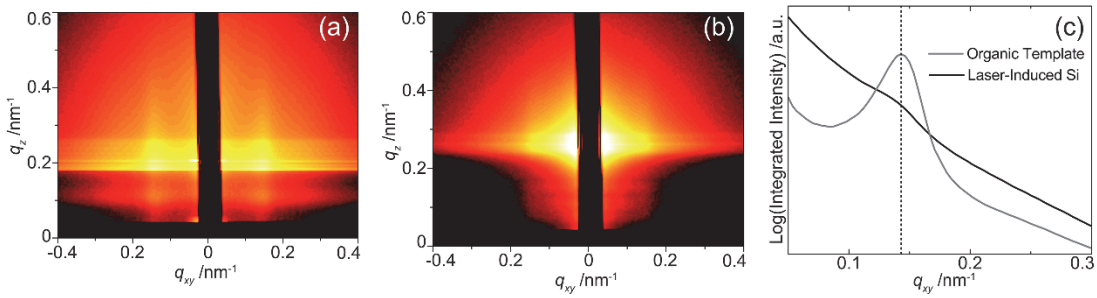

Figure 6.2. GISAXS profiles of (a) mesoporous resin template and (b) 350-400 nm thick laser-induced c-Si nanostructures at incidence angles of 0.12 ° and 0.15°, respectively. (c) Integrated intensity plots of corresponding GISAXS patterns.

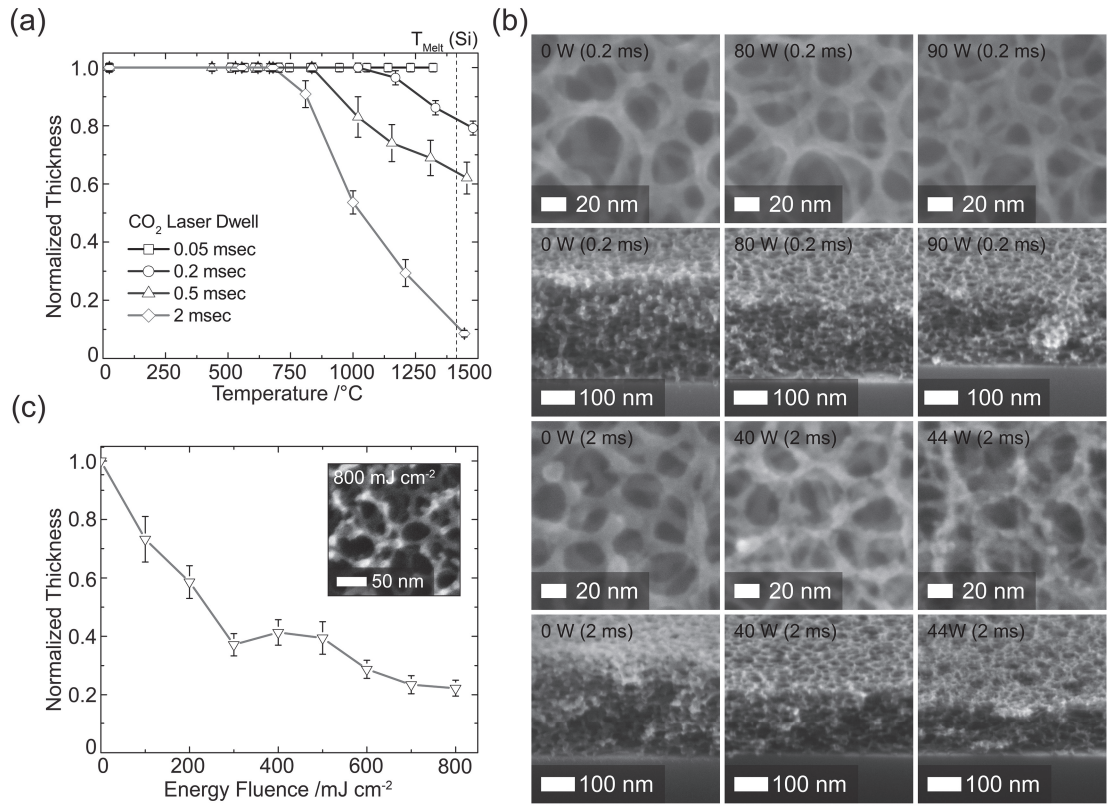

Figure 6.3. (a) Film thickness plots of mesoporous resin template remaining versus transient heating temperature by a single pass of CO_2 laser irradiation of 0.05, 0.2, 0.5 and 2 ms dwells. (b) Plan view and cross-sectional SEM micrographs of mesoporous templates after CO_2 laser-induced transient heating as indicated. (c) Film thickness plots of resin template remaining after a single 40 ns pulsed excimer laser irradiation at energy fluences between 100 and 800 mJ cm^{-2}. Inset shows the plan view SEM of a mesoporous sample after laser irradiation at the highest fluence of 800 mJ cm^{-2}.

at 75 W (0.2 ms dwell; extrapolated to 1480 °C) and 40 W (2 ms dwell; extrapolated to 1000 °C) in Figure S6.3b and c, respectively, are very similar to that of the Raman spectrum of a mesoporous amorphous carbon film pyrolysed in a furnace at 600 °C for 3 h. The phenolic network condensation into amorphous carbon at higher temperatures corroborates well with thermal stability enhancement of mesoporous resin samples at shorter dwells. At even higher laser powers, *e.g.*, 48 W of 2 ms dwell (extrapolated to 1445 °C), thermal decomposition of the mesoporous template resulted in significant film thickness losses (Figure 6.3a) and diminished Raman spectrum intensities (Figure S6.3c).

Figure 6.3c shows the evolution of the thickness of the mesoporous organic template after a single 40 ns pulsed excimer laser irradiation at fluences of 100-800 mJ cm^{-2}. We observe a rapid film thickness loss of over 60% from 100 to 300 mJ cm^{-2}, and a more gradual decrease at higher energy fluences of 400 to 800 mJ cm^{-2}. We hypothesize that the thickness loss is partially due to laser ablation as phenolic resin readily absorbs the ultraviolet excimer laser irradiation[41,42] and gets heated transiently to temperatures much greater than the melting point of Si (>1414 °C). Raman spectroscopy indicates that the phenolic resin networks condensed into amorphous carbon along with a ~30% film thickness loss at 100 mJ cm^{-2} energy fluence (Figure S6.3d). Interestingly the template retained mesoporous structural features for all excimer laser energy fluences up to 800 mJ cm^{-2} (see plan view SEM inset in Figure 6.3c).

We observed that the dense a-Si overlayer in Figure 6.1e,h,k plays a key role for successful 3D pattern transfer from mesoporous organic resin template to the excimer laser-induced c-Si nanostructures. Upon laser irradiation at 700 mJ cm^{-2}, most of the photons are absorbed by the a-Si overlayer and converted into thermal energy to induce

Si melting as indicated by the sharp spike in time-resolved reflectance measurements (Figure S6.1a).[35,43] As the Si melt front (at 1414 °C) propagates through the a-Si into the substrate, the resin scaffold condenses into amorphous carbon and acts as a "hard" support for liquid Si that subsequently solidifies after ~40 ns.[28,29] In our control experiments we indeed observed no mesoporous structural features for samples with little or no a-Si overlayer after pulsed excimer laser annealing and template removal, confirming the critical role of the dense a-Si overlayer (Figure S6.4). Some photons (*e.g.* at the 700 mJ cm^{-2} energy fluence) may get absorbed by the resin material causing ablation near the top of the mesoporous organic template. This results in the formation of asymmetrical laser-induced c-Si network nanostructures with graded nanoporosity; in Figure 6.1f,i,l (and Figure S6.2) the largest pores are observed at the air/Si interface and get increasingly smaller towards the Si substrate interface (see Figure 6.1f,i,l and S6.2).

As discussed in the introduction one of the advantages of working with all-organic over inorganic thin film templates is the accessibility of well-ordered complex 3D BCP morphologies which subsequently could be transferred into the corresponding c-Si structures *via* pulsed laser annealing. In order to demonstrate this potential we performed a proof-of-principle experiment to generate laser-induced gyroidal c-Si nanostructures by BCP-directed organic templating. BCP gyroid structures usually consist of two interpenetrating gyroidal sub-volumes related by an inversion operation. If these two sub-volumes are constituted by the same material (*e.g.* in AB diblock copolymers), the structure is referred to as a double gyroid ($G^D, Ia\bar{3}d$). In the case that the two sub-volumes are made up of different materials (*e.g.* in ABC triblock terpolymers) the structure is called the alternating (or single) gyroid ($G^A, I4_132$). For our experiments, ISO-resol hybrid samples with alternating gyroid (G^A) morphology

were first prepared by evaporation-induced self-assembly.[26] Subsequently, 700-900 nm thick cryo-microtomed sections of such a highly ordered G^A ISO-resol hybrid sample and collected on the Si substrate. SEM images in Figure 6.4a and b show a highly porous resin thin film with mesoscopic G^A network morphology obtained after removing ISO terpolymer by pyrolysis at 450 °C. Lower magnification SEM images in Figure S6.5a and b demonstrate that the ~600 nm thick G^A mesoporous resin films adhered smoothly on Si substrate with no observable crack formation or delamination, attributed to the "soft" nature of the all-organic hybrid thin films. SEM images in Figure 6.4c-f demonstrate that periodically ordered 3D porous Si inverse nanostructures could be obtained after a-Si CVD, excimer laser annealing at a lower energy fluence of 500 mJ cm^{-2}, and template removal. Plan view SEM images show that the interconnected pores of the G^A mesoporous resin template (Figure 6.4a) and the network struts of the resulting laser-induced Si nanostructures (Figure 6.4e) shared similar dimensions of 60-70 nm. Cross-sectional SEM images in Figure 6.4d and f also reveal that the excimer laser-induced melt-crystallization of Si was incomplete as the bottom third of the samples show a dense layer. Despite only having about two thirds of the backfilled a-Si transformed into mesoporous gyroidal c-Si structures by melt infiltration,[44] this proof-of-concept experiment has demonstrated the possibility to generate highly ordered and periodic gyroidal c-Si nanostructures by combining mesoporous BCP-directed organic templating with pulsed laser annealing.

In conclusion, we have described the first examples of coupling mesoporous BCP-directed organic resin templating with transient laser-induced melt-crystallization to generate 3D porous c-Si network nanostructures. The mesoporous resin remained highly stable up to the melting temperature of Si (1414 °C) in air when heated with a 10.6 μm CO_2 laser on sub-millisecond time frames. It was found that a dense a-Si overlayer was

critical to shield the mesoporous resin template from strongly absorbing the 308 nm excimer laser irradiation to prevent massive template ablation and structural collapse. Raman spectroscopy revealed that the mesoporous resin scaffold material further crosslinked into amorphous carbon phase during transient heating thereby supporting the excimer laser-induced Si melt-crystallization to form 3D porous c-Si nanostructures. Besides disordered network structures, we have demonstrated the transition from BCP-directed inorganic to organic templating enables the formation of periodically ordered gyroidal c-Si nanostructures *via* pulsed laser annealing. We expect that the methodology introduced here can be further enhanced, for example, achieving ordered morphologies in ISO-resol hybrid thin films directly *via* solvent annealing[21,25] and/or laser spike annealing[39,45] before the pyrolysis heat treatment. For complete melt-conversion into the crystalline phase, the Si melt time can be extended by increasing the transient heating dwell to enhance the Si melt flow and infiltration into the resin template before solidification. Finally, by arresting the regrowth of a new SiO_2 layer on the Si substrate before a-Si deposition, it should be possible to generate mesoporous single-crystal epitaxial Si nanostructures[35] with different periodically ordered morphologies that may enable new functionalities and advanced applications.

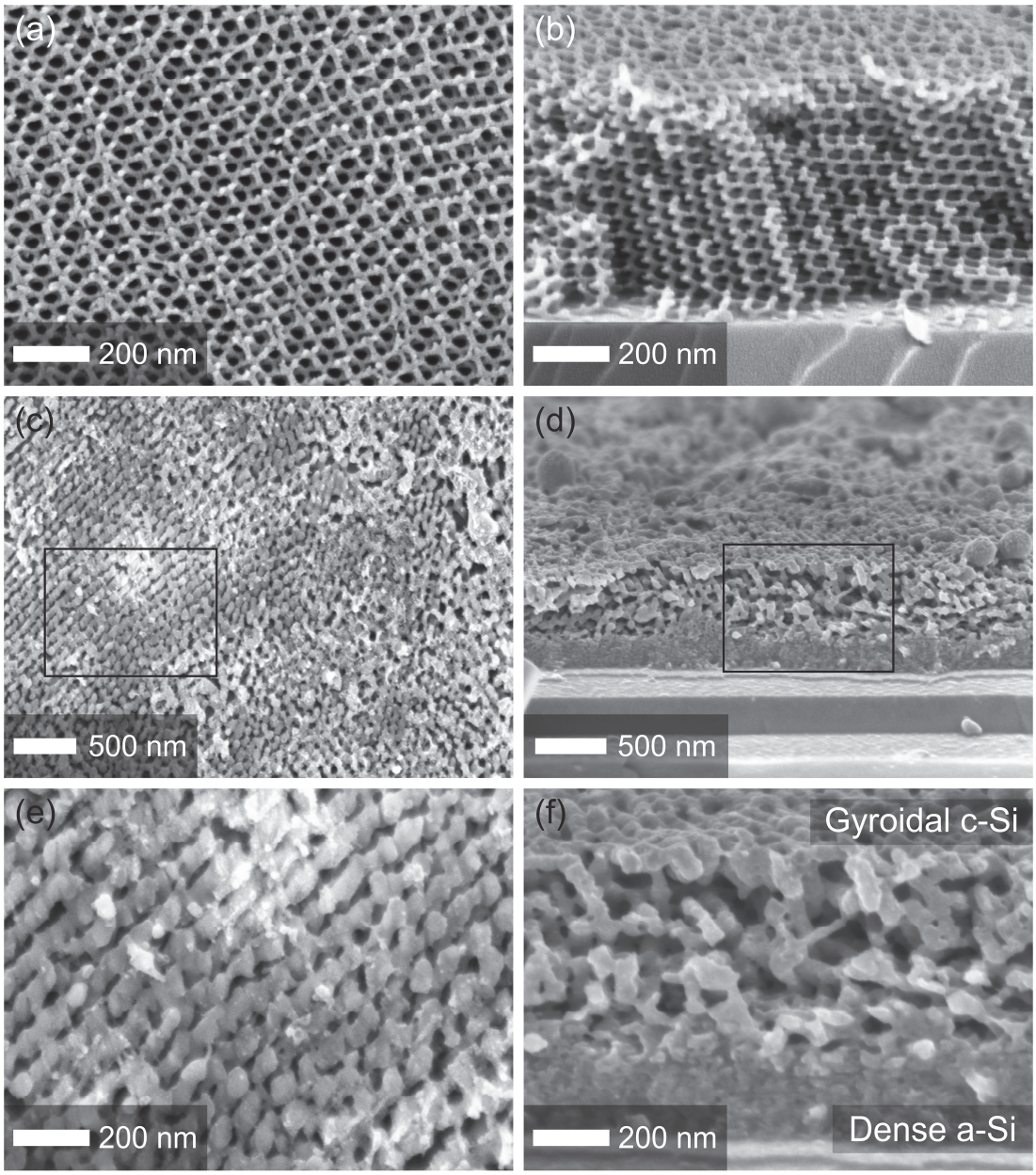

Figure 6.4. Plan view and cross-sectional SEM micrographs of (a,b) cryo-microtomed G^A mesoporous resin template and (c,d) periodically ordered gyroidal Si inverse nanostructures after pulsed excimer laser annealing and template removal. (e,f) Higher magnification SEM images of the black boxes annotated in (c,d), respectively.

Experimental Section

Mesoporous BCP-directed resin template synthesis. 4, 6 and 8 wt% ISO-resol solutions were prepared by dissolving polyisoprene-*block*-polystyrene-*block*-polyethylene oxide triblock terpolymer (PI-*b*-PS-*b*-PEO, ISO, M_n = 68.9 kg/mol, with a polydispersity index of 1.04 containing 29.6% PI, 64.8 wt% PS and 5.4 wt% PEO) with resorcinol-formaldehyde resol oligomers (ISO/resol = 2.4:1, w/w) in anhydrous tetrahydrofuran (Sigma Aldrich) and stirred for 1 h. ISO terpolymer and oligomeric resorcinol-formaldehyde resols were synthesized according to protocols described elsewhere.[26] Hybrid thin films with disordered network morphology were spin-coated on Si substrates (4P0.01-.02SSP-INV, WRS Materials) at 2000 rpm (45 s) in a nitrogen drybox, followed by curing at 100 °C in a vacuum oven overnight (>12 h). The ISO-resol hybrid samples with G^A morphology (ISO/resol = 3.125:1, w/w) were prepared by evaporation-induced self-assembly as reported elsewhere.[26] The G^A hybrid samples were sectioned with a Leica Ultracut UC7 cryo-ultramicrotome at -60 °C, collected on a water/dimethyl sulfoxide (6:4, v/v) solution surface and transferred to Si substrates. Mesoporous phenolic resin thin films were formed by heating the hybrid samples in a tube furnace at 450 °C (1 h) in nitrogen with a ramp rate of 1 °C/min. For Raman spectroscopy measurements, mesoporous resin samples were heated in a tube furnace at 600 °C (3 h) in nitrogen with a ramp rate of 1 °C/min for conversion into amorphous carbon.

Native SiO_2 layer removal and amorphous silicon chemical vapor deposition. The mesoporous resin template was first immersed in 0.5% HF acid solution (100:1) for about 2 min, blown dry with nitrogen and immediately loaded into the CVD chamber prior to chamber evacuation for a-Si deposition. A static CVD system was used to

deposit a-Si into the mesoporous resin template at 350 °C (3 h) with disilane as precursor.[6]

10.6 µm Wavelength CO_2 Laser Irradiation. The CO_2 laser-induced transient heating setup used in the experiments is described elsewhere.[39] Mesoporous resin thin films with ~200 nm thickness were irradiated with a single pass of CO_2 laser irradiation at 28-92 W and dwells of 0.05, 0.2, 0.5 and 2 ms dwells.

308 nm Wavelength Pulsed Excimer Laser Irradiation. The 40 ns pulsed XeCl excimer laser setup used here with some modifications is described elsewhere.[35] All samples were held in a homebuilt vacuum chamber holder (<1 Torr) with a quartz window for excimer laser irradiation. Mesoporous resin thin film samples were irradiated at 100-800 mJ cm^{-2} energy fluences. The resin/a-Si composite samples with disordered network morphology were irradiated with a single pulse of 700 mJ cm^{-2} energy fluence. The G^A resin/a-Si composite samples were irradiated with a single pulse of 500 mJ cm^{-2} energy fluence.

Template Removal. The excimer laser-irradiated samples were sequentially treated in CF_4 RIE for 10-20 s (30 sccm, 40 mTorr, 150 W) to remove the Si overlayer, hot piranha solution (97% H_2SO_4/30% H_2O_2 = 3:1, v/v) held at 75 °C for 3 h to remove the template, and 49% HF for 10-30 s to remove the SiO_2 layer.

Characterization. SEM images were acquired on Au-Pd coated mesoporous resin samples using a LEO 1550 SEM equipped with an in-lens detectors. Thin film thickness was determined from SEM and profilometry measurements using a Tencor P-10 profilometer. Raman spectroscopy measurements were conducted using a Renishaw InVia confocal Raman microscope with a 785 nm excitation laser source. 2D X-ray diffraction measurements were performed on a Bruker General Area Detector

Diffraction System (GADDS) equipped with a Bruker HI-STAR area detector using Cu Kα radiation (40 kV, 40 mA, λ = 0.15418 nm). GISAXS was measured at the G1 beamline of the Cornell High Energy Synchrotron Source (CHESS). The G1 beamline setup consists of a multilayer monochromator of wavelength λ = 0.118 nm with a Dectris Pilatus 200k area detector mounted vertically at a distance of 2.657 m from the sample. The resolution of the area detector was 487 × 407 pixels with a 172 μm pixel size. The incident angle of the beam was varied between 0.1 ° and 0.3 ° with typical exposure times <2 sec. GISAXS patterns were analyzed with the FIT2D program.[46]

Acknowledgement

This work was supported by the National Science Foundation (NSF) Single Investigator Award (DMR-1409105). K.W.T. gratefully acknowledges the Singapore Energy Innovation Programme Office for a National Research Foundation graduate fellowship. This work made use of research facilities at Cornell Center for Materials Research (CCMR) with support from the NSF Materials Research Science and Engineering Centers (MRSEC) program (DMR-1120296); Cornell NanoScale Science & Technology Facility (CNF), a member of the National Nanotechnology Infrastructure Network, which is supported by the National Science Foundation (Grant ECCS-0335765); Cornell High Energy Synchrotron Source (CHESS) which is supported by the NSF and the National Institutes of Health/National Institute of General Medical Sciences under NSF award DMR-1332208. The authors gratefully acknowledge Prof. Lara Estroff and Dr. Maura Weathers of Cornell University for helpful discussions.

REFERENCES

[1] C. A. Ross, K. K. Berggren, J. Y. Cheng, Y. S. Jung, J.-B. Chang, *Adv. Mater.* **2014**, *26*, 4386.

[2] M. C. Orilall, U. Wiesner, *Chem. Soc. Rev.* **2011**, *40*, 520.

[3] D. Van Gough, A. T. Juhl, P. V. Braun, *Mater. Today* **2009**, *12*, 28.

[4] M. Ieong, B. Doris, J. Kedzierski, K. Rim, M. Yang, *Science* **2004**, *306*, 2057.

[5] A. M. Urbas, M. Maldovan, P. DeRege, E. L. Thomas, *Adv. Mater.* **2002**, *14*, 1850.

[6] S. A. Rinne, F. García-Santamaría, P. V. Braun, *Nat. Photonics* **2008**, *2*, 52.

[7] E. C. Nelson, N. L. Dias, K. P. Bassett, S. N. Dunham, V. Verma, M. Miyake, P. Wiltzius, J. A. Rogers, J. J. Coleman, X. Li, P. V. Braun, *Nat. Mater.* **2011**, *10*, 676.

[8] K. Hur, Y. Francescato, V. Giannini, S. A. Maier, R. G. Hennig, U. Wiesner, *Angew. Chem. Int. Ed.* **2011**, *50*, 11985.

[9] K.-V. Peinemann, V. Abetz, P. F. W. Simon, *Nat. Mater.* **2007**, *6*, 992.

[10] Y. Gu, R. M. Dorin, U. Wiesner, *Nano Lett.* **2013**, *13*, 5323.

[11] R. M. Dorin, H. Sai, U. Wiesner, *Chem. Mater.* **2014**, *26*, 339.

[12] E. J. W. Crossland, M. Kamperman, M. Nedelcu, C. Ducati, U. Wiesner, D.-M. Smilgies, G. E. S. Toombes, M. A. Hillmyer, S. Ludwigs, U. Steiner, H. J. Snaith, *Nano Lett.* **2009**, *9*, 2807.

[13] P. Docampo, M. Stefik, S. Guldin, R. Gunning, N. A. Yufa, N. Cai, P. Wang, U. Steiner, U. Wiesner, H. J. Snaith, *Adv. Energy Mater.* **2012**, *2*, 676.

[14] H. Zhang, P. V. Braun, *Nano Lett.* **2012**, *12*, 2778.

[15] K. W. Tan, D. T. Moore, M. Saliba, H. Sai, L. A. Estroff, T. Hanrath, H. J. Snaith, U. Wiesner, *ACS Nano* **2014**, *8*, 4730.

[16] F. S. Bates, *Science* **1991**, *251*, 898.

[17] J. N. L. Albert, T. H. Epps III, *Mater. Today* **2010**, *13*, 24.

[18] M. Templin, A. Franck, A. D. Chesne, H. Leist, Y. Zhang, R. Ulrich, V. Schädler, U. Wiesner, *Science* **1997**, *278*, 1795.

[19] D. Zhao, J. Feng, Q. Huo, N. Melosh, G. H. Fredrickson, B. F. Chmelka, G. D. Stucky, *Science* **1998**, *279*, 548.

[20] S. H. Joo, S. J. Choi, I. Oh, J. Kwak, Z. Liu, O. Terasaki, R. Ryoo, *Nature* **2001**, *412*, 169.

[21] C. Liang, K. Hong, G. A. Guiochon, J. W. Mays, S. Dai, *Angew. Chem. Int. Ed.* **2004**, *43*, 5785.

[22] Y. Meng, D. Gu, F. Zhang, Y. Shi, H. Yang, Z. Li, C. Yu, B. Tu, D. Zhao, *Angew. Chem. Int. Ed.* **2005**, *44*, 7053.

[23] H. Kosonen, S. Valkama, A. Nykänen, M. Toivanen, G. ten Brinke, J. Ruokolainen, O. Ikkala, *Adv. Mater.* **2006**, *18*, 201.

[24] H. Sai, K. W. Tan, K. Hur, E. Asenath-Smith, R. Hovden, Y. Jiang, M. Riccio, D. A. Muller, V. Elser, L. A. Estroff, S. M. Gruner, U. Wiesner, *Science* **2013**, *341*, 530.

[25] Z. Qiang, J. Xue, K. A. Cavicchi, B. D. Vogt, *Langmuir* **2013**, *29*, 3428.

[26] J. G. Werner, T. N. Hoheisel, U. Wiesner, *ACS Nano* **2014**, *8*, 731.

[27] P. Yang, D. Zhao, D. I. Margolese, B. F. Chmelka, G. D. Stucky, *Nature* **1998**, *396*, 152.

[28] T. Katou, B. Lee, D. Lu, J. N. Kondo, M. Hara, K. Domen, *Angew. Chem. Int. Ed.* **2003**, *42*, 2382.

[29] J. Lee, M. C. Orilall, S. C. Warren, M. Kamperman, F. J. DiSalvo, U. Wiesner, *Nat. Mater.* **2008**, *7*, 222.

[30] S. C. Warren, L. C. Messina, L. S. Slaughter, M. Kamperman, Q. Zhou, S. M. Gruner, F. J. DiSalvo, U. Wiesner, *Science* **2008**, *320*, 1748.

[31] R. Buonsanti, T. E. Pick, N. Krins, T. J. Richardson, B. A. Helms, D. J. Milliron, *Nano Lett.* **2012**, *12*, 3872.

[32] I. E. Rauda, R. Buonsanti, L. C. Saldarriaga-Lopez, K. Benjauthrit, L. T. Schelhas, M. Stefik, V. Augustyn, J. Ko, B. Dunn, U. Wiesner, D. J. Milliron, S. H. Tolbert, *ACS Nano* **2012**, *6*, 6386.

[33] M. Stefik, S. Wang, R. Hovden, H. Sai, M. W. Tate, D. A. Muller, U. Steiner, S. M. Gruner, U. Wiesner, *J. Mater. Chem.* **2012**, *22*, 1078.

[34] Z. Li, K. Hur, H. Sai, T. Higuchi, A. Takahara, H. Jinnai, S. M. Gruner, U. Wiesner, *Nat. Commun.* **2014**, *5*, 3247.

[35] H. Arora, P. Du, K. W. Tan, J. K. Hyun, J. Grazul, H. L. Xin, D. A. Muller, M. O. Thompson, U. Wiesner, *Science* **2010**, *330*, 214.

[36] M. D. McGehee, *Nature* **2013**, *501*, 323.

[37] X. H. Liu, L. Zhong, S. Huang, S. X. Mao, T. Zhu, J. Y. Huang, *ACS Nano* **2012**, *6*, 1522.

[38] Z. Bao, M. R. Weatherspoon, S. Shian, Y. Cai, P. D. Graham, S. M. Allan, G. Ahmad, M. B. Dickerson, B. C. Church, Z. Kang, H. W. Abernathy Iii, C. J. Summers, M. Liu, K. H. Sandhage, *Nature* **2007**, *446*, 172.

[39] B. Jung, J. Sha, F. Paredes, M. Chandhok, T. R. Younkin, U. Wiesner, C. K. Ober, M. O. Thompson, *ACS Nano* **2012**, *6*, 5830.

[40] K. Iyengar, B. Jung, M. Willemann, P. Clancy, M. O. Thompson, *Appl. Phys. Lett.* **2012**, *100*, 211915.

[41] M. Badertscher, P. Bühlmann, E. Pretsch, *Structure Determination of Organic Compounds Tables of Spectral Data*, Springer-Verlag Berlin Heidelberg, Berlin, Heidelberg, **2009**.

[42] L. Urech, T. Lippert, *Photochemistry and Photophysics of Polymer Materials*, John Wiley & Sons, Hoboken, N.J, **2010**.

[43] M. O. Thompson, G. J. Galvin, J. W. Mayer, P. S. Peercy, J. M. Poate, D. C. Jacobson, A. G. Cullis, N. G. Chew, *Phys. Rev. Lett.* **1984**, *52*, 2360.

[44] P. E. de Jongh, T. M. Eggenhuisen, *Adv. Mater.* **2013**, *25*, 6672.

[45] J. P. Singer, K. W. Gotrik, J.-H. Lee, S. E. Kooi, C. A. Ross, E. L. Thomas, *Polymer* **2014**, *55*, 1875.

[46] A. P. Hammersley, S. O. Svensson, M. Hanfland, A. N. Fitch, D. Hausermann, *High Pressure Res.* **1996**, *14*, 235.

APPENDIX E

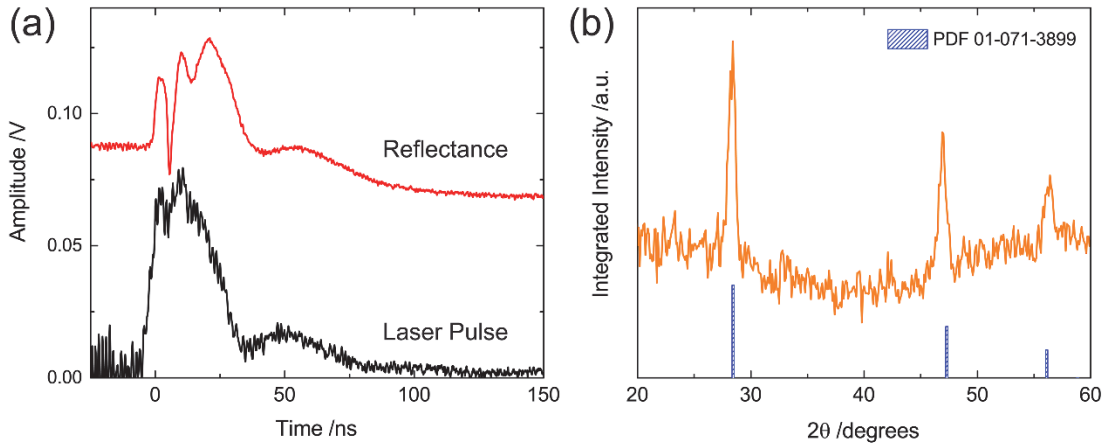

Figure S6.1. (a) Time-resolved reflectance measurement (red curve) of a single pulsed excimer laser irradiation at 700 mJ cm^{-2} on a ~400 nm thick a-Si/resin template sample using a 650 nm wavelength HeNe diode probe laser. The sharp increase in reflectance trace indicates Si melting at ~0 ns while the decline signifies recrystallization at 40-50 ns. The oscillations in the reflectance trace during Si melt state are attributed to thin film interference effects in the resin/Si composite material. The black curve indicates the incident excimer laser pulse profile. (b) 2D X-ray diffraction integrated intensity plot of a 350-400 nm thick excimer laser-induced polycrystalline Si inverse nanostructures after template removal.

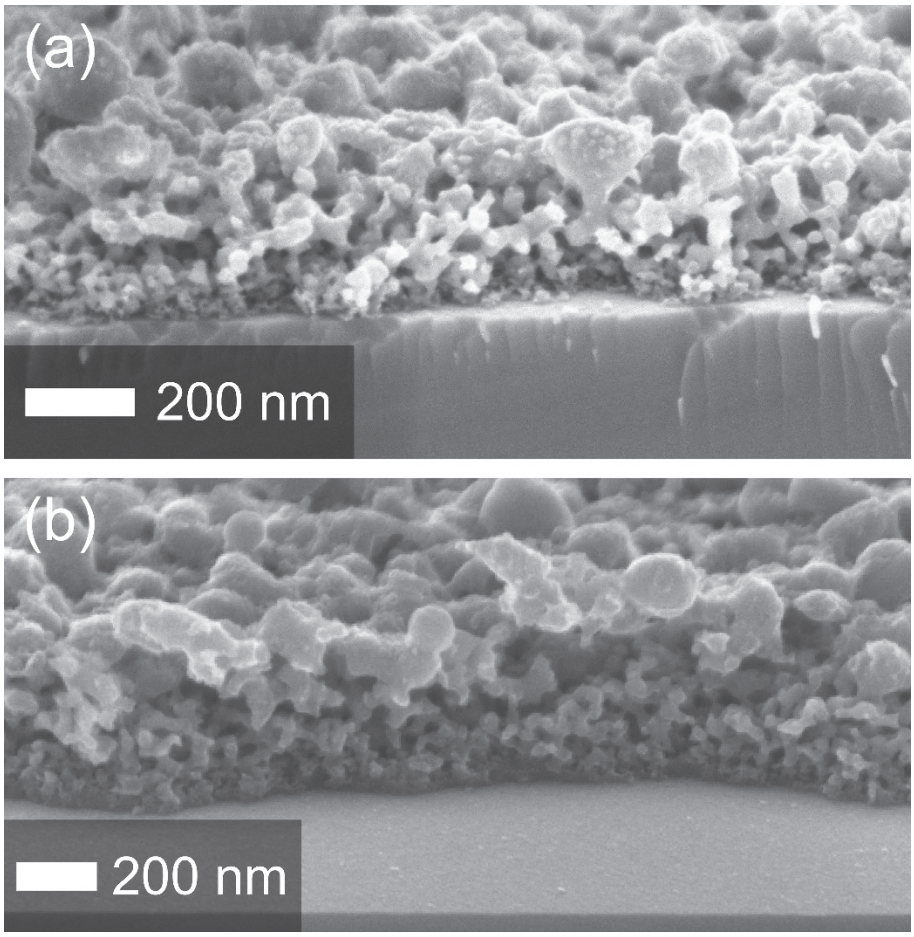

Figure S6.2. Cross-sectional SEM micrographs of (a) ~200 and (b) 350-400 nm thick excimer laser-induced asymmetrical porous c-Si nanostructures.

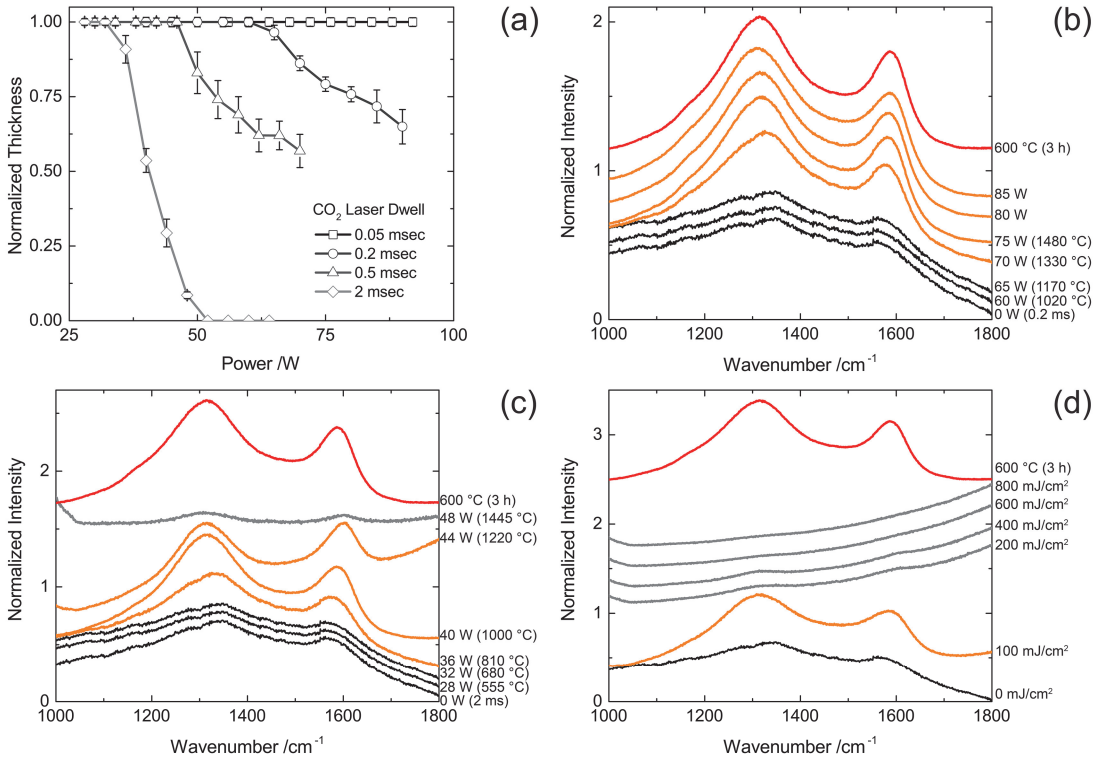

Figure S6.3. (a) Film thickness plots of resin templates annealed by a single pass of CO_2 laser irradiation at different dwells as indicated. (b-d) Raman spectra of resin samples annealed by CO_2 laser-induced transient heating at (b) 0.2 ms and (c) 2 ms dwells, and (d) after 40 ns pulsed excimer laser irradiation. The red curves in the Raman spectra are that of the mesoporous amorphous carbon samples pyrolysed in a tube furnace at 600 °C for 3 h under nitrogen.

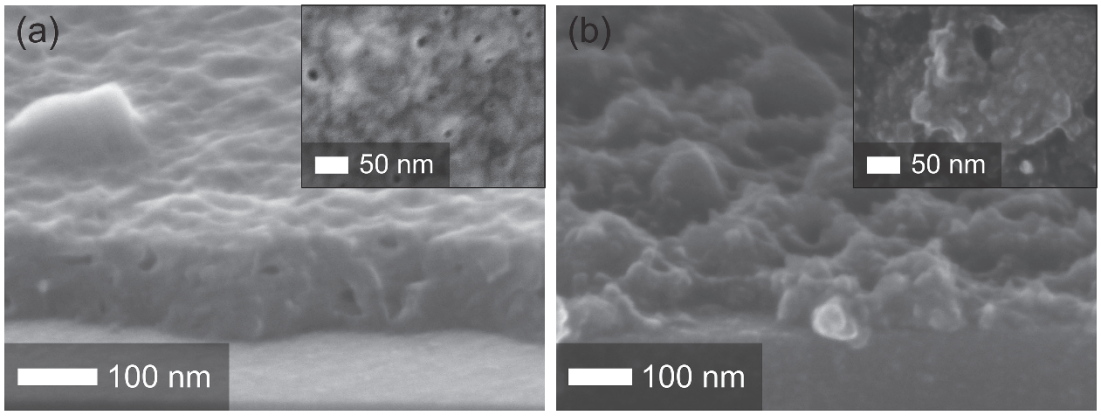

Figure S6.4. Cross-sectional and plan view (insets) SEM micrographs of (a) resin/a-Si composite nanostructures after removing the a-Si overlayer by CF_4 RIE, and (b) collapsed excimer laser-induced c-Si structure after template removal.

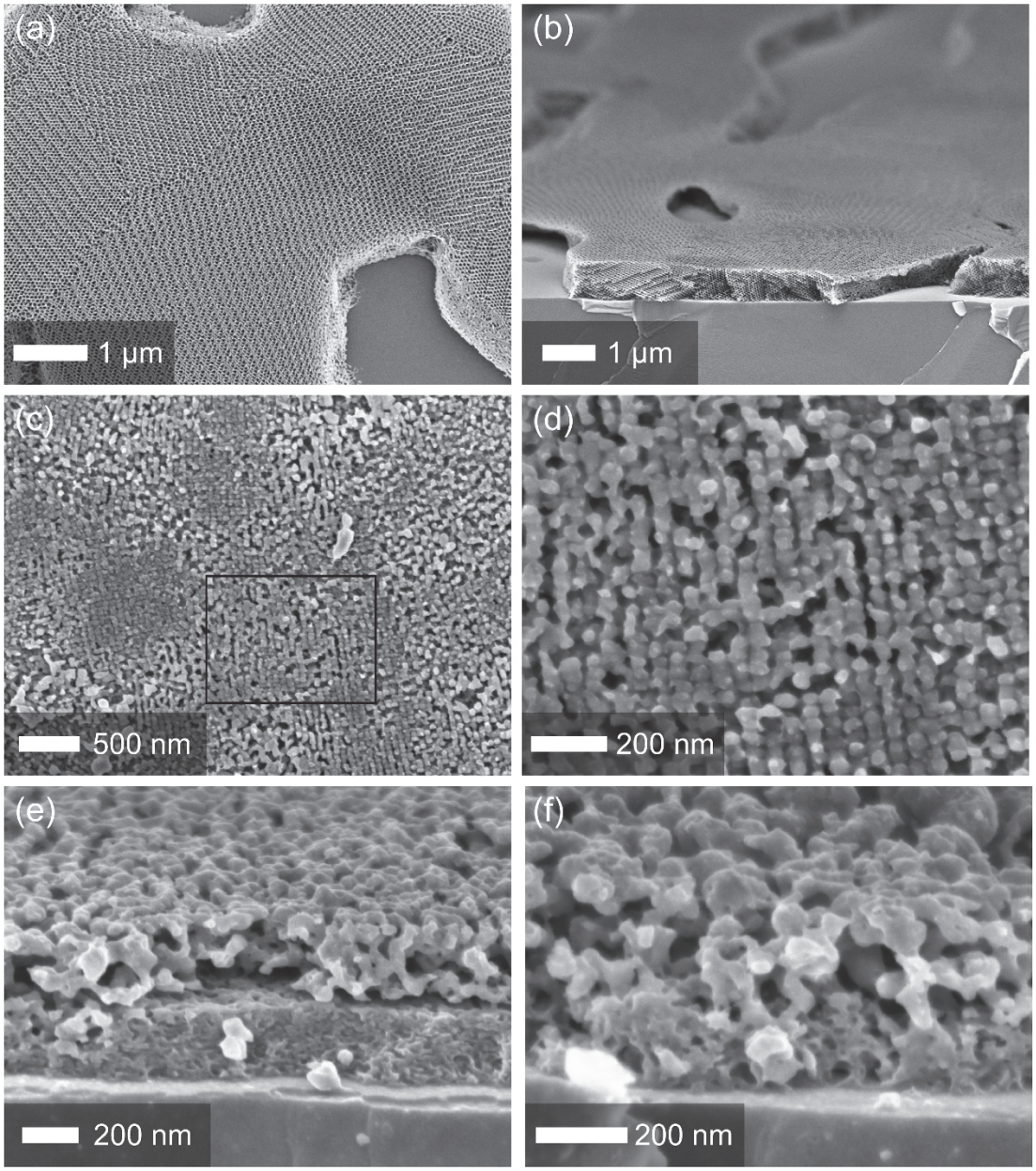

Figure S6.5. (a) Plan view and (b) cross-sectional SEM micrographs of (a,b) cryo-microtomed G^A mesoporous resin templates at lower magnifications. (c) Plan view SEM image of periodically ordered gyroidal Si inverse nanostructures after pulsed excimer laser annealing and template removal. The black boxed annotation in (c) is shown in (d) with higher magnification. (e,f) Cross-sectional SEM micrographs of periodically ordered gyroidal Si inverse nanostructures after pulsed excimer laser annealing and template removal.

CHAPTER 7

CONCLUSIONS

Self-assembly provides a simple, efficient and scalable route to realize biologically-inspired structures with multi-level length scales, materials complexity and functional properties. In this dissertation, I have demonstrated two approaches in the design, synthesis and characterization of mesoscopic and multi-modal hybrid structures from the bottom-up.

In the first part, grazing incidence wide-angle X-ray scattering was employed to probe the structural evolution of methylammonium lead trihalide perovskites on a mesoporous polyisoprene-*block*-polystyrene-*block*-polyethylene oxide terpolymer-directed alumina superstructure during thermally annealing on a hotplate. The BCP-directed alumina superstructure provided a homogenous interconnecting mesoscale pore for solution backfilling and subsequent crystallization of the hybrid perovskite. A slow temperature ramp (from ambient to 100 °C) in a dry environment was found to promote the formation of an unidentified solid-state precursor structure that remained stable up to 80 °C before transforming into crystalline tetragonal perovskite. From scanning electron microscopy (SEM), the presence of the precursor structure was correlated with enhanced final film coverage and BCP-directed alumina perovskite solar cell performance. Furthermore, by combining the slow ramp with a short rapid increase of annealing temperature (to 130 °C), hybrid perovskite crystal growth was accelerated with domain sizes attaining several micrometers. The micron sized perovskite domain film coverage on a planar substrate was estimated to be more than 95%, resulting in a planar heterojunction perovskite solar cell with 13.5% power conversion efficiency.

Hence, time/temperature control provides a simple means via (hotplate) thermal annealing to improve materials physical property and functionality.

In the second half of the dissertation, I reported the rapid direct conversion of polystyrene/silica colloidal crystal templates (CCTs) to non-close-packed inverse crystalline silicon (Si) nanostructures with almost 100% fidelity using pulsed excimer laser irradiation. Similar to BCP-directed inorganic templates, the thermal stability and structural integrity of the amorphous silica template was sufficient to support laser-induced Si melting and solidification. Exploiting the unique physical property enhancements provided by transient heating, I demonstrated a multi-level formation of porous structures in a single process by coupling BCP-directed resol self-assembly with sub-millisecond CO_2 laser-induced transient heating. In this block copolymer-based writing induced by transient heating experiments (B-WRITE) method, the all-organic hybrid system was irradiated sequentially at increasing laser powers in air to induce thermopolymerization of resol oligomers, followed by BCP decomposition, resulting nanoporous 3D resin polymer network structures. The pore size was tunable over two orders of magnitude (10-1000 nm) by varying the BCP, BCP/resol composition and hybrid film thickness. When heated at higher temperatures in nitrogen, the resin structure condensed into electrically conductive nanoporous carbons. Moreover, arbitrary-shaped patterns up to the millimeter scale could be directly defined by the laser beam without a mask. To this end, a microfluidic device was constructed using the B-WRITE method with the resin network structure in the channel providing additional surface areas that may be useful for catalysis and sensing applications. The B-WRITE method is also compatible with current semiconductor processing methods to form more complex hierarchical porous structures. Finally, I utilized the mesoporous resin structure as a template for laser-induced melt-conversion to porous crystalline Si

network nanostructures. From Raman spectroscopy measurements, I proposed that the phenolic resin condensed into amorphous carbon during sub-millisecond transient heating, enabling enhancement of thermal and mechanical stability to support the melt and subsequent solidification of Si.

The findings described in this dissertation provide ideas for a number of future experiments. The B-WRITE method could be extended to other platforms, for example, flexible substrates and direct fabrication of portable miniaturized sensing and energy storage devices. Ordered mesoporous BCP-directed resol hybrid samples prepared by annealing protocols could be coupled with laser irradiation to form single-crystal epitaxial Si and other functional inorganic nanostructures. 3D bicontinuous interconnecting single-crystal semiconducting Si or gallium arsenide exhibiting a lack of grain boundaries allowing optimal charge transport, as well as the ability to epitaxially grow along specific crystal axes, may be integrated with hybrid perovskite materials for significant energy conversion improvements.